
Dynamical and Critical Properties of Bosonic Quantum Impurity Models

A Density Matrix Renormalization Group study

Master's Thesis
Benedikt Bruognolo

Chair of Theoretical Solid State Physics
Faculty of Physics
Ludwig-Maximilians-University Munich



Supervisors:

Prof. Dr. Jan von Delft and PD Dr. Andreas Weichselbaum

Munich, June 5, 2013

Bosonische Quanten-Störstellen Modelle: Dynamik und kritische Phänomene

Dichte-Matrix Renormierungsgruppen Studie

Master Arbeit
Benedikt Bruognolo

Lehrstuhl für theoretische Festkörperphysik
Fakultät für Physik
Ludwig-Maximilians-Universität München



Betreuer:
Prof. Dr. Jan von Delft und PD Dr. Andreas Weichselbaum

München, den 5. Juni 2013

Contents

1	Introduction	1
2	Critical phenomena	3
2.1	Classical phase transitions	3
2.1.1	Critical phenomena and exponents	4
2.1.2	Landau Theory	5
2.1.3	Renormalization group and scaling	7
2.2	Quantum phase transitions	8
2.2.1	Quantum vs. classical phase transitions	9
2.2.2	Scaling and quantum to classical mapping	10
2.2.3	Quantum impurity phase transition	11
3	Numerical Methods	12
3.1	Matrix Product States	12
3.1.1	Global vs. local picture	13
3.1.2	Orthogonalization of effective basis sets	14
3.1.3	Basic MPS application	15
3.1.4	Reduced density matrix and block entropy	17
3.1.5	Symmetries	18
3.2	Bosonic numerical renormalization group	19
3.2.1	Spin-Boson model	19
3.2.2	Logarithmic discretization	20
3.2.3	Mapping onto the Wilson tight-binding chain	21
3.2.4	Iterative diagonalization	23
3.2.5	Renormalization group flow	24
3.2.6	Choice of bosonic basis	24
3.3	Variational matrix product states	26
3.3.1	Variational ground state calculation	26
3.3.2	Optimal bosonic basis and shift	29
3.3.3	One-site vs. two-site optimization	30
3.3.4	Energy-level flow diagrams	31
3.3.5	Time-dependent VMPS	32
4	Spin-boson model	34
4.1	Static properties	35
4.1.1	Ground state phases	36
4.1.2	Quantum phase transition	38
4.1.3	Subsequent results for critical exponents	40
4.2	Non-equilibrium dynamics	43

4.2.1	tVMPS and z-averaging	43
4.2.2	Ohmic dynamics	45
4.2.3	Sub-ohmic dynamics	48
5	Two-bath spin-boson model	50
5.1	Model Hamiltonian	50
5.1.1	Symmetries	51
5.1.2	VMPS setup	53
5.2	Ground state phases	55
5.2.1	Properties of critical coupling phase	57
5.2.2	Determining the phase boundaries	59
5.3	Critical Phenomena	61
5.3.1	Quantum critical point 1 (QC1)	61
5.3.2	Quantum critical point 2 (QC2)	66
5.4	Asymmetric coupling	70
5.5	Comparison of methods: symmetry improved VMPS	72
6	Conclusion	76
	Appendices	78
A.1	Two-site VMPS with optimal bosonic basis	79
B.1	SBM1: critical exponents	82
C.1	SBM2: Calculation of the magnetization in the $U(1)$ symmetry code	83
C.2	SBM2: Influence of diverging bosonic basis on QC1 and QC2	85
C.3	SBM2: Critical exponents	87
C.3.1	ν at QC1	87
C.3.2	β at QC1	88
C.3.3	δ at QC1	89
C.3.4	β at QC2	90
C.3.5	δ at QC2	91
C.3.6	ν at QC2	92

1. Introduction

In recent years, the steady miniaturization of electronics has become part of our everyday life. Without even realizing it, most of us work and interact with devices that consist of small structures on the order of a few nanometers. For instance, a transistor being part of the CPU in a commercially available smartphone or laptop is already smaller than $100nm$. At those scales, quantum effects come into play and might drastically change the physical properties of a system. With continuing progress in the field of semiconductors pushing the miniaturization process to new limits, it becomes increasingly important to obtain a profound understanding of solid state physics at nano scales.

Since a quantum system cannot be isolated perfectly in any realistic situation, it is particularly important to find an appropriate description of the system interacting with its environment, which often consists of a large number of degrees of freedom. For the theoretical analysis of such situations, one typically relies on quantum impurity models, that in general consist of a small impurity system with only few degrees of freedom coupled to a large non-interacting quantum systems, the bath or reservoir, containing a large number of fermionic or bosonic particles. Famous examples of quantum impurity models include the Kondo model [1, 2], the interacting resonant level mode [3] or the spin-boson model [4, 5]. The latter is particularly interesting due to its bosonic nature, which allows the simulation of a non-charged environment. Popularized in 1987 by Leggett et al. in the context of quantum dissipation [4, 6], the spin-boson model has been applied to a variety of physical systems such as electron transfer processes in biomolecules [7], noisy qubits [8, 9] and cold atom quantum dots [10, 11], to name but a few.

Due to the complexity arising from the large number of degrees of freedom contained in the bath, only very few quantum impurity models can be treated in an exact way. At the same time, perturbative approaches can fail to capture the physical properties completely, since multiple energy scales may become important. Instead, one relies on powerful numerical methods such as the Numerical Renormalization Group (NRG) [12, 13] and the Density Matrix Renormalization Group (DMRG) [14, 15] in order to fully characterize the physical properties of a quantum impurity model.

More recently, bosonic quantum impurity models have attracted new attention in the context of phase transitions at zero temperature, so-called quantum phase transition. The debate was initiated by first numerical studies of the critical properties of the spin-boson model, which exhibits a quantum phase transition between a localized and a delocalized state. The results obtained with bosonic NRG suggested a failure of quantum-to-classical correspondence [16, 17, 18], an analytic technique which characterizes a quantum phase transition by mapping it onto a thermal phase transition of a classical model. Since this statement implied far-reaching consequences not only for the physics of the spin-boson model, it triggered successive works employing different numerical schemes, which all confirmed the validity of quantum-to-classical correspondence [19, 20, 21]. The method introduced by Guo et al., based on a Variational Matrix Product State (VMPS) procedure [22], was not only

capable to study the spin-boson model with high accuracy across the entire phase diagram, but also illustrated the limitations of bosonic NRG in a very convincing way.

Motivated by Guo's work, we extend the powerful VMPS approach to enable a dynamical analysis of the standard spin-boson model. Moreover, we continue Guo's VMPS study of a generalized spin-boson model including a second bath, which exhibits a highly non-trivial ground state phase diagram including a novel phase at intermediate coupling. The main focus of this thesis is the study of the critical phenomena of the two-bath spin-boson model. We present the first extensive numerical study of the critical properties of the two-bath model and compare the numerical results to analytic renormalization group predictions.

The thesis is structured as follows:

- **Chapter 2 – Critical phenomena:** In this chapter we briefly introduce the physics of critical phenomena including a discussion of analytic approaches such as mean-field theory and renormalization group. In addition, we address the topic of quantum phase transitions and sketch the idea of quantum-to-classical correspondence
- **Chapter 3 – Numerical methods:** Starting with the matrix product state formalism, we present the procedure of NRG applied to a bosonic quantum impurity model. Moreover, we explain how the most important limitation of bosonic NRG can be cured by a variational matrix product state approach. Finally, we extend the VMPS algorithm to the treatment of real-time dynamics.
- **Chapter 4 – Spin-boson model:** This chapter briefly summarizes the ground state properties of the spin-boson model at zero temperature and its critical phenomena. We present VMPS results for various critical exponents, before discussing the non-equilibrium dynamics of the ohmic and sub-ohmic model.
- **Chapter 5 – Two-bath spin-boson model:** The discussion of the two-bath version starts with reviewing the symmetries incorporated in the XY -symmetric Hamiltonian and the VMPS setup for this model. In the next step, we elaborate on the rich ground state phase diagram at zero temperature, which includes two distinct quantum phase transitions and focus on the properties of the intermediate coupling phase. Based on VMPS results, we finally present an extensive study of the critical properties.
- **Chapter 6 – Conclusion:** The last chapter summarizes the main results of this work and gives an outlook on possible topics of future research.

2. Critical phenomena

Phase transitions have been a major subject of active studies in statistical and condensed matter physics for more than a century. Powerful methods, including renormalization group approaches have been developed to describe the striking physical properties observed in systems near a transition point, known as critical phenomena. Triggered by experiments on high-temperature superconductors and heavy fermion compounds, focus has been drawn to a subclass of phase transitions occurring in systems at zero temperature, called Quantum Phase Transitions (QPT). Not driven by thermal but by quantum fluctuations, QPTs strongly affect the low temperature phase diagram of electronic systems including examples of quantum impurity models, such as the Kondo [1, 2] or the spin-boson model [4, 5].

In this chapter, we give a short introduction into the rich physics of critical phenomena, that will be relevant for our numerical results in Chap. 4 and 5. Starting with a classical system, we briefly discuss theoretical concepts such as mean field theory, renormalization group and scaling, mainly following the books of H. Nishimori, G. Ortiz [23] and D. Uzunov [24]. Based on the reviews of M. Vojta [25], T. Vojta [26] and the book of S. Sachdev [27] we continue with quantum phase transitions in the second part, sketching the idea of quantum-to-classical mapping, a technique that allows to relate a QPT to a classical transition located in a higher dimension. We conclude the chapter with a discourse on QPTs in quantum impurity models, which are also subject of the numerical calculations presented in this thesis.

2.1 Classical phase transitions

The phenomenon of a phase transition describes the crossover between two phases of matter due to the variation of a system parameter such as temperature or pressure. This is accompanied by a dramatic change of macroscopic properties in the system which can be described theoretically by the appearance of singularities in functions characterizing physical quantities like entropy S , specific heat C or volume V . But what exactly causes the occurrence of a phase transition from a physical point of view? Consider the free energy $F = E - TS$ of the system, which consists of the internal energy E and the entropy S of the system. Both terms compete with each other: while the first term (E) favors an ordered state, the second one (S) prefers a disordered one. Which of the two terms dominates is determined by the values of external parameters (such as temperature T or volume V). Therefore a sudden change in the latter can lead to a phase transition.

To distinguish different phases of a material, we introduce a physical quantity called the *order parameter*, which 'measures' the order or rather the degree of asymmetry of the system. Being usually non-zero in the ordered (symmetry-broken) phase, the order parameter vanishes in the disordered (symmetric) phase. For example, the magnetization m is the best choice of the order parameter in ferromagnetic materials. Below the Curie temperature T_c the electronic spins can align in one specific direction (spontaneous symmetry breaking), leading to a finite magnetization and an ordered phase. Above T_c the spins do not favor any

particular direction, therefore the material is in a disordered phase with zero magnetization.

There exists a classification going back to Ehrenfest [28], that divides phase transitions into two different types. Those which are accompanied by a singularity in a first-order derivative of the free energy F are labeled *first order* phase transitions. At such transitions the correlation length ξ of the system is generally finite.¹ A transition is called *continuous* if a singularity shows up in a second- or higher-ordered derivative of the free energy. Furthermore, such a transition is characterized by a diverging correlation length. By convention a phase transition is classified by the order of the derivative that first shows a divergence or discontinuity. In Fig. 2.1 both types of transitions are shown for a ferromagnet.

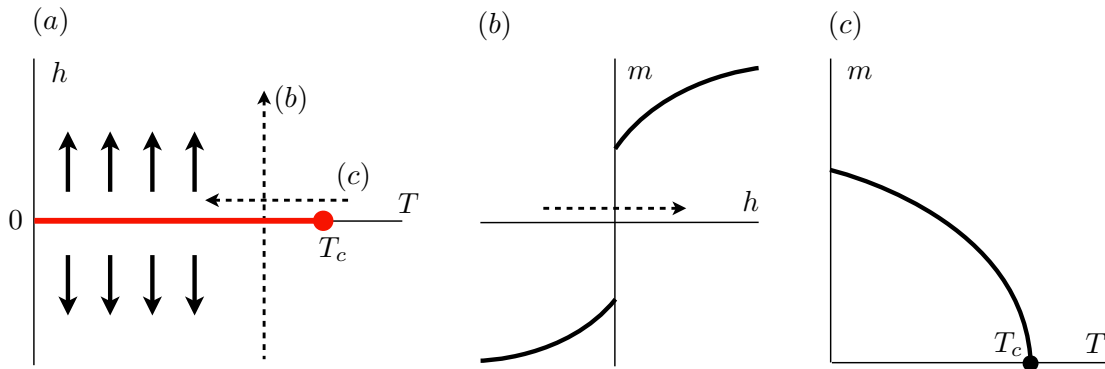


Figure 2.1: Possible phase transitions in a ferromagnetic material: changing the magnetic field h below T_c from positive to negative value as shown in (b) induces a first order phase transition, where the sign of the magnetization flips. As illustrated in (c), lowering the temperature T from $T > T_c$ to a value below the critical point leads to spontaneous magnetization - the system performs a second order phase transition. Figure adapted from [23].

2.1.1 Critical phenomena and exponents

Critical phenomena is the collective name associated with the fascinating physical behavior of a system that appears near the critical point in continuous phase transitions.

To explain the idea of critical phenomena let us get back to our ferromagnetic example. Starting in the delocalized phase with $m = 0$, $T > T_c$ and $h = 0^+$, we approach the critical point at T_c by lowering the temperature. The magnetization still stays at zero in the vicinity of the critical point. Nevertheless, it now rises rapidly if a finite magnetic field h is applied. While we observe a linear response of m to the magnetic field for $T \gg T_c$, the magnetization follows a super-linear power law near the critical point, $m \propto h^{1/\delta}$ (with $\delta > 1$). Defining the magnetic susceptibility χ as the first-order derivative of m with respect to the external field h , it follows that $\chi \approx m/h \propto h^{1/\delta-1}$ diverges for $h \rightarrow 0$ in the critical system. There exist an very intuitive explanation for this effect. Although the spins do not align spontaneously on a macroscopic scale yet, the material shows a tendency to form fairly large clusters of aligned spins for T close to T_c . Because the clusters react coherently to an external magnetic field, the magnetization rises rapidly with increasing h .

The behavior of m near the critical point illustrated above is one example of a critical phenomenon. It is characterized by the power-law exponent δ , a so called *critical exponent*.

¹The correlation length is a measure of the range over which fluctuations in one region of space are correlated with those in another region.

In general these basic variables describe the divergence or the degree of singularity of physical quantity near the critical point and specify the underlying critical phenomena. The most commonly used critical exponents and their definitions are summarized in table (2.1).

phys. Quantity	Definition	Exponent	Condition
Specific heat	$C \propto t ^{-\alpha}$	α	$t \rightarrow 0, h = 0$
Order parameter	$m \propto t ^{-\beta}$	β	$t \rightarrow 0^-, h = 0$
Susceptibility	$\chi \propto t ^{-\gamma}$	γ	$t \rightarrow 0, h = 0$
Order parameter	$m \propto h ^{-1/\delta}$	δ	$t = 0, h \rightarrow 0$
Correlation length	$\xi \propto t ^{-\nu}$	ν	$t \rightarrow 0, h = 0$
Correlation function	$G(r) \propto r^{-d+2-\eta}$	η	$t = 0, h = 0$
Correlation time	$\tau_c \propto \xi^z$	z	

Table 2.1: Definition of critical exponents. $|t|$ denotes the (dimensionless) difference between the control parameters and their critical value (e.g. $t = (T - T_c)/T_c$ in case of temperature), $G(r)$ the connected two-point correlation function $G(r) = \langle S_i S_{i+r} \rangle - \langle S_i \rangle \langle S_{i+r} \rangle$ of two spins S_i, S_{i+r} separated by a distance r , ξ the correlation length, τ_c the correlation time and d the space dimensionality of the system.

Particularly interesting is the exponent ν which describes the singular behavior of the correlation length ξ close to the critical point. The divergence of ξ implies that spacial correlations of order parameter fluctuations become long-ranged, since ξ specifies the characteristic length scales over which these fluctuations decay in the system. Analogous fluctuations show long range time-correlations near the critical point. This is indicated by the correlation time τ_c , which also diverges in a critical system, $\tau_c \propto \xi^z$, where z is called the dynamic critical exponent.

Since critical exponents play a key role in the characterization of critical phenomena, a lot of effort is put into developing systematic ways to calculate their values.

2.1.2 Landau Theory

To study critical phenomena from a theoretical point of view, one starts with a model that captures the essential features of the examined system, then tries to solve it according to the prescription of statistical mechanics. In general, such many-body systems are very difficult to handle, since they usually include a huge number of interacting particles. Therefore an exact solution can only be found for a few exceptions and we have to resort to approximate methods to understand the essential physics of the system. Commonly used and very efficient techniques are mean-field theories. The main idea of these methods is to replace all interactions between particles by an averaged or effective one, thereby reducing a many-particle problem to an effective one-body problem. While having limitations, mean-field theories provide a reasonable starting point in the study of critical phenomena.

Early examples of mean-field theories are the Weiss' molecular field theory of ferromagnets [29] or the van-der-Waals theory of the liquid-gas transition [30]. Modern approaches are often based on the Landau theory of phase transitions [31], which can be understood as a unification of earlier mean-field approaches.

Landau theory is a phenomenological theory, i.e. it does not include the elementary degrees of freedom of the microscopic model. It assumes that the free energy F is an analytic function of the order parameter and therefore can be expanded in a power-series. For a ferromagnetic phase transition the expansion of F in terms of the magnetization m

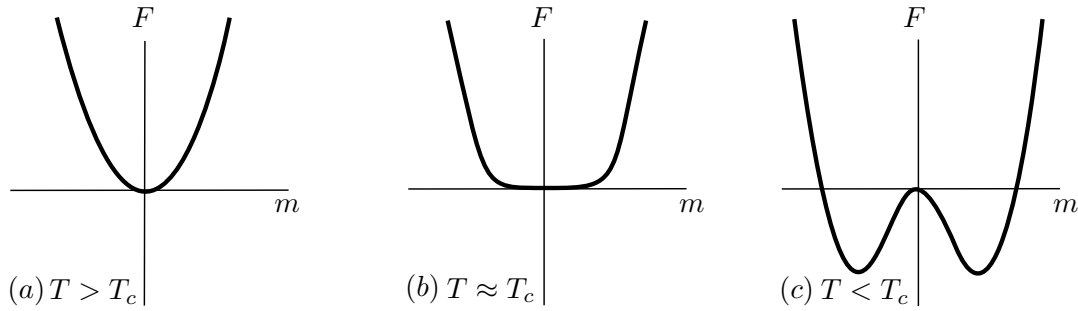


Figure 2.2: Free energy of a ferromagnetic material (a) in a disordered, (b) in a critical and (c) in an ordered state.

reads

$$F_L(m) = F_0 + am^2 + bm^4 + \mathcal{O}(m^5), \quad (2.1)$$

where F_0 , a and b are constants as functions of m but have dependencies on external parameters such as temperature or magnetic field. Usually, comparison to experimental data or first-principle calculations from the microscopic model are used to determine their value for a given system. The equilibrium value of m is calculated by minimizing $F_L(m)$ for a given set of external parameters.

Interestingly, critical phenomena within Landau theory are *super-universal*, indicating that the behavior of all continuous phase transitions is identical. Consequently, critical exponents in completely different physical systems always have the same value in Landau theory (or any other mean-field approaches), listed in table (2.2).

Exponent	Mean-field value
α	0
β	1/2
γ	1
δ	3

Table 2.2: Mean-field values of critical exponents

Experimental results generally lead to deviations in comparison to the predictions of Landau theory. Although critical phenomena show a certain degree of universality, it turns out to be weaker than the predicted super-universality. Why Landau theory not fully agrees with experimental data was a controversial problem for decades and could only be resolved by the introduction of Wilson's renormalization group [12, 32].

The fundamental limitation of Landau theory (and of any mean-field approach) is that it does not include fluctuations around the average of the order parameter. Especially in low-dimensional systems these fluctuations play an important role for the physical behavior at the critical point, while their effects generally decrease in higher dimensions. It turns out that in sufficiently high-dimensional systems Landau theory actually does lead to the correct critical exponents. A dimensional analysis shows that for a given model, there exist two critical dimensions, d_{uc} and d_{lc} , called the upper and lower critical dimension, respectively. In systems where the spatial dimensionality d exceeds its upper critical dimension, $d > d_{uc}$, critical exponents always correspond to the mean-field predictions. If d lies in between upper

and lower critical dimensions, $d_{uc} > d > d_{lc}$, there is still a phase transition present in the system, but the critical exponents no longer agree with the mean-field values. In systems with a dimensionality below the lower critical dimension, $d < d_{lc}$, the strength of the fluctuations destroys the ordered phase completely, so no phase transition takes place.

In a ferromagnetic system at nonzero temperature $d_{uc} = 4$, while $d_{lc} = 2$ or $d_{lc} = 1$, depending on whether the system obeys Ising or Heisenberg symmetry, respectively [26].

2.1.3 Renormalization group and scaling

Mean-field theories offer useful insights as a first step towards understanding critical phenomena, because they give an overview of the physical behavior at the critical point. However, in a system where fluctuations become dominant, it is necessary to proceed beyond mean-field approaches in order to draw clear qualitative and quantitative conclusions. A very powerful tool to analyze critical phenomena while systematically including fluctuations is the Renormalization Group (RG) [12, 32].

The key idea behind RG is the exploitation of an additional symmetry present at the critical point, which is absent in the underlying Hamiltonian. We have already encountered one major feature of critical phenomena: the divergence of the correlation length ξ close to the critical point. In a system with a characteristic length scale going to infinity, the physics is invariant under a scaling transformation, because the structure of correlations is the same at all length scales. This means that a coordinate transformation of the kind $\mathbf{r} \rightarrow \mathbf{r}' = \mathbf{r}/b$, where b is the *rescaling factor*, leaves the dominant physical features of the system invariant.

A renormalization group transformation transforms the Hamiltonian of one scale to the one on the next scale starting from the original Hamiltonian. Applied to an Hamiltonian H with a set of coordinates \mathbf{r} , the RG transformation only affects \mathbf{r} but not the form of the Hamiltonian,

$$R[H(\mathbf{r})] = H(\mathbf{r}'). \quad (2.2)$$

The sequence of effective Hamiltonians resulting from the RG transformation describe the *renormalization group flow*. Usually, the RG flow converges to one or more so-called *fixed points* \mathbf{r}^* , which are invariant under the RG transformation $R[H(\mathbf{r}^*)] = H(\mathbf{r}^*)$. The fixed points give the possible macroscopic states at a large scale. In addition, it is possible to calculate the critical exponents of the system based on the RG flow. A detailed treatment of the single steps would be beyond the scope of this thesis. However, we briefly elaborate on important *scaling relations* for the critical exponents and their derivation using very general arguments.

Before exploiting the rescaling invariance of the system at the critical point, we have to include what was missing in Landau theory - we have to take the fluctuations of the order parameter into account. To accomplish that, we formulate the partition function of the system as a functional integral

$$Z = e^{-H/k_bT} = \int \mathcal{D}[\Phi] e^{-S[\Phi]/k_bT}, \quad (2.3)$$

where a fluctuating field $\Phi(r)$ now represents the local order parameter and $S[\Phi]$ is the Landau-Ginzburg-Wilson free energy functional given by

$$S[\Phi] = \int d^d r [c(\nabla\Phi(r))^2 + F_L(\Phi(r)) - h\Phi(r)]. \quad (2.4)$$

The thermodynamic average m of the order parameter is calculated by taking the thermal average $\langle\Phi\rangle$ with the statistical weight e^{-S/k_bT} . Even though m is still zero in the delocalized phase, fluctuations of Φ are now included [26].

We have already mentioned that in the vicinity of the critical point all physical properties remain unchanged when we rescale all lengths in the system by a factor b . Within the RG framework this makes it possible to derive so called *homogeneity relation* for thermodynamic quantities, which can be used to evaluate critical exponents. For the free energy density $f = -(k_b T/V) \log(Z)$ the homogeneity relations is given by

$$f(t, h) = b^{-d} f(tb^{1/y_t}, hb^{y_h}), \quad (2.5)$$

where y_t and y_h are exponents of *scaling fields* entering the RG equations (for a detailed derivation see [23] chap. 4). The four critical exponents $\alpha, \beta, \gamma, \delta$, which are directly derived from the free energy density, relate to y_t and y_h very generally,

$$\alpha = 2 - \frac{d}{y_t}, \quad \beta = \frac{d - y_h}{y_t}, \quad \gamma = \frac{2y_h - d}{y_t}, \quad \delta = \frac{y_h}{d - y_h}. \quad (2.6)$$

Note that only two scaling parameters appear in Eq. (2.5), while there exist four critical exponents $\alpha, \beta, \gamma, \delta$ which can be derive from f . Thus knowledge of only two of the latter is sufficient to determine the remaining two critical exponents. Their dependence can be expressed in the form of *scaling relations*

$$2 - \alpha = 2\beta + \gamma, \quad 2 - \alpha = \beta(\delta - 1). \quad (2.7)$$

Using an additional homogeneity relation for the correlation function, it is also possible to express the critical exponents ν and η in terms of y_h and y_t ,

$$\nu = \frac{1}{y_t}, \quad \eta = d - 2y_h + 2. \quad (2.8)$$

A careful analysis reveals several additional scaling relations,

$$\alpha = 2 - d\nu, \quad \beta = \frac{\nu(d - 2 + \eta)}{2}, \quad \gamma = \nu(2 - \eta), \quad \delta = \frac{d + 2 - \eta}{d - 2 + \eta}. \quad (2.9)$$

Scaling relations for exponents that involve explicitly the dimensionality of the system are called *hyperscaling relations*. In contrast to (ordinary) scaling relations in Eq. (2.7), hyperscaling relations only hold below the upper critical dimension d_{uc} [33].

The above scaling relations are a generic feature of continuous phase transitions and do not depend on the underlying system. They are a signature of the *universality* of critical phenomena. There exist wide classes of different physical systems that show the same critical behavior (so called *universality classes*). For example, a liquid gas transition and a ferromagnetic phase transition in uniaxial magnets belong to the same universality class. This can be understood by the fact that microscopic details of the systems are rendered irrelevant at the critical point due to the diverging correlation length ξ . Critical phenomena thus only depend on more general features of the Hamiltonian such as symmetries.

2.2 Quantum phase transitions

Until now, we only focussed on thermal fluctuations driving the phase transition. As temperature is lowered, however, thermal fluctuations decrease and eventually cease as $T \rightarrow 0$. Quantum fluctuations on the other hand are still present even at very low temperature. Being a consequence of Heisenberg's uncertainty principle, these fluctuations can initiate a different class of phase transitions called quantum phase transitions (QPT) at absolute zero, which has attracted a lot of attention in the last two decades. At very first sight QPTs seem

to be solely an academic topic, since it is impossible to reach $T = 0$ in any experimental setup. However, since the properties of a critical point govern the behavior of the system also in the vicinity of the critical point, the presence of a QPT is discernable at non-zero temperatures, as well. Indeed, it turns out that QPTs contribute to the solution of many open problems in condensed matter physics such as high-temperature superconductors [34, 35], heavy fermion compounds [36, 37] and two-dimensional electron gases [38, 39].

There exist several excellent reviews on QPTs [39, 25] including the book of S. Sachdev [27], we will refrain from introducing the topic at length here. After a phenomenological discussion on QPTs we sketch the idea of quantum-to-classical mapping and focus on the quantum impurity phase transitions, a subclass which occurs in open quantum systems.

2.2.1 Quantum vs. classical phase transitions

It is worthwhile to ask how quantum mechanics affects a second order phase transition. Two possible answers exist. Firstly quantum mechanics can be relevant in the description of the ordered phase, e.g. in the case of superconductors. Then again quantum fluctuations may directly affect the critical behavior determining the universality class the system belongs to. This can only occur if the typical energy scale of quantum fluctuations in the system, $\hbar\omega_c$, is significantly larger than the thermal energy, $k_B T$. We stated in the previous section that the correlation time τ_c of the order parameter fluctuations diverges close to the critical point. Accordingly the typical frequency scale ω_c , and for the same reason also the typical energy scale, drop to zero according to (see table 2.1)

$$\hbar\omega_c \propto |t|^{\nu z} \quad t \rightarrow 0. \quad (2.10)$$

As a consequence, quantum mechanics will not influence the critical behavior for a system at a finite temperature T^* as long as for that temperature the condition $\hbar\omega_c < T^*$ is satisfied, i.e. as long as the distance to the critical point is smaller than the crossover scale, $|t| < [T^*]^{1/\nu z}$. Since this condition can always be satisfied by tuning the temperature sufficiently close to T_c , critical phenomena of finite temperature transitions are dominantly affected by thermal fluctuations and we can ignore quantum mechanics in these cases. Following this argument, it is justified to call them 'classical' phase transition.

In contrast, a transition at zero temperature controlled by a non-thermal parameter (magnetic field, pressure) is fully determined by quantum fluctuations, since the crossover scale T^* vanishes. Phase transitions of this kind are called quantum phase transitions.

Near the Quantum Critical Point (QCP) both thermal and quantum fluctuations can intertwine, giving rise to two interesting types of phase diagrams shown in Fig. (2.3). In the first case displayed in Fig. 2.3(a), the system can establish an ordered phase only at $T = 0$. Consequently, the phase transition is not accessible in any real experiment. Nevertheless, there still are interesting signatures of the QPT observable at finite temperatures. Depending on the strength of the control parameter g used to tune the system through the QPT, we can distinguish three regimes. While in the so-called thermally disordered region thermal fluctuations are responsible for the destruction of long ranged order, quantum fluctuations dominate in the so-called quantum disordered region at $g > g_c$. Here the system essentially resembles that in its quantum disordered ground. For values of g close to g_c the system enters the so-called quantum critical phase, where both thermal and quantum fluctuations play an important role. Here the system shows to some extent critical behavior with respect to g , but the thermal fluctuations drive it away from criticality. This leads to unusual properties such as non-Fermi liquid behavior and unorthodox power laws [25]. In Fig. 2.3(b) the ordered phase also exists at finite temperatures, making a classical phase transition observable between ordered and thermally disordered phases at finite temperatures.

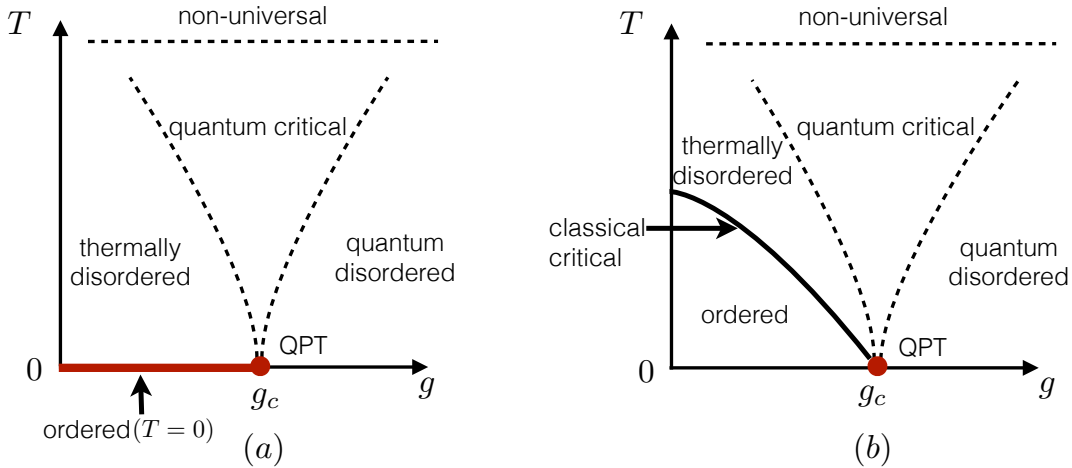


Figure 2.3: Schematic phase diagram of system in the vicinity of a quantum phase transition, where g is a non-thermal control parameter. In (a) the system can only form an ordered phase at $T = 0$ (red solid line), while in (b) the ordered phase exist also at finite temperatures (solid black line). Figure adapted from [39].

2.2.2 Scaling and quantum to classical mapping

Similar to the classical continuous phase transition, scaling arguments are useful to gain further insights of the critical behavior close to a quantum phase transition. However, the quantum mechanical case is more complicated. In classical statistical mechanics the kinetic and potential contribution to the partition function Z factorize, thus making it possible to study thermodynamic critical behavior using effective time-independent theories with dimensionality d , equal to the number of spatial dimension in the corresponding system.

The situation is different in quantum statistical mechanics, where the kinetic and potential part of the Hamiltonian usually do not commute. Consequently, the partition function $Z = \text{Tr} \exp(-\beta \hat{H})$ no longer factorizes and thermodynamic and dynamic critical behavior have to be solved together. This can be accomplished by interpreting the canonical density operator $\exp(-\beta \hat{H})$ as a time-evolution operator in imaginary time, $-it/\hbar = \tau \in [0, \beta]$ [26]. The resulting functional corresponding to the classical Landau-Ginzburg-Wilson function in Eq.(2.4) needs to be formulated in terms of time- and space dependent fields,

$$S[\Phi] = \int_0^\beta d\tau \int d^d r [a(\partial_\tau \Phi(r, \tau))^2 + c(\nabla \Phi(r, \tau))^2 + F_L(\Phi(r, \tau)) - h\Phi(r, \tau)]. \quad (2.11)$$

From Eq.(2.11) we can derive an amazing feature of quantum statistical mechanics. At zero temperature the imaginary time acts as another spatial dimension with infinite extension. Thus a quantum phase transition in d dimensions can be interpreted as a classical phase transition in $d + z$ dimensions². This property is called *quantum-to-classical correspondence*. Analogous to the classical case, scaling techniques can be applied to derive a modified homogeneity law for the free energy density [27]. Quite often the corresponding classical transition has already been subject to detailed study, simplifying calculations to extract the critical behavior of the QPT tremendously. For example, the QCP of the later discussed spin-boson model corresponds to the classical transition in an 1D Ising model with long ranged interaction [40, 41].

²Note from the previous section that time scales like the z th power of a length in the vicinity of the critical point, z being the dynamical critical exponent.

While a quantum-to-classical mapping does simplify the description of QPTs in many systems, it is not always applicable. For example, a Berry phase term showing up in topological phases can lead to a negative statistical weight, making it impossible to identify the quantum partition function with a classical one [27]. Even if the mapping is successful, only the thermodynamic criticality can be extracted. For a description of real time dynamics, novel theories are necessary [26].

2.2.3 Quantum impurity phase transition

An interesting subcategory of QPTs are so-called boundary quantum phase transitions, where only the degrees of freedom belonging to a subsystem of the full system show a critical behavior. Such types of QPTs occur for example in quantum impurity models, where the impurity acts as a boundary which can become critical independent from the rest of the system [41]. In general, a quantum impurity model consists of a small quantum system, the impurity, that is coupled to a large reservoir or bath of particles. Typically, the Hamiltonian has the general structure

$$\hat{H} = \hat{H}_{imp} + \hat{H}_{bath} + \hat{H}_{coupling}, \quad (2.12)$$

where the first two terms describe the independent contribution of impurity and bath to the Hamiltonian, while the interaction between the two systems is defined in the last term. The bulk degrees of freedom in \hat{H}_{bath} can be of fermionic or bosonic nature and are usually considered to be non-interacting, though this assumption is not valid in general. In most models the spectrum of the bath is gapless and shows a power law behavior at low frequencies. Since QPTs occur at $T = 0$ only, the low energy contributions to the bath spectrum are most important. Furthermore, the thermodynamic limit of the bath has to be considered in order to study the critical phenomena of the model. The impurity Hamiltonian \hat{H}_{imp} consists of only few degrees of freedom, e.g. one or more quantum spins. The most prominent examples of quantum impurity models that show interesting QPTs are the Kondo model [1, 2] and the spin-boson model [4, 5], that we discuss further below.

Three types of impurity QPTs can be distinguished. A first order transition indicates a simple level crossing in the system's ground state, which is not topic of this thesis. The more interesting type of QPT are continuous QPTs, which are accompanied by critical exponents. The critical phenomena then depend on a continuous parameter that specifies the low-energy power law in the density of bath states. Moreover, the effective dimension of the system is essentially determined by this parameter for some quantum impurity models as the spin-boson model. Thus it influences, for example, the validity of hyperscaling relations (see Sec. 2.1.3). If the model approaches its lower-critical dimension d_{lc} , the QPT can turn into a Kosterlitz-Thouless transition, which is characterized by an exponentially diverging correlation length [42].

3. Numerical Methods

The purpose of this chapter is to introduce two very popular numerical methods, that allow the study of quantum criticality and other low-energy properties in quantum impurity models: the Numerical Renormalization Group (NRG) [12, 13] and the Density Matrix Renormalization Group (DMRG) [14, 15]. Both methods can be formulated within the framework of Matrix Product States (MPS), a concept originally developed in quantum information. The MPS formulation of NRG [43] and DMRG [44, 45, 22] not only lead to a deeper understanding of the methodology and opened the door for various extensions hard to see in the conventional formulations [46]. Moreover, it allowed to establish a close connection between both methods [47, 43], crucial for the development of the numerical setup used in this work.

In the following sections we give an MPS based introduction to NRG and DMRG focusing on application to bosonic systems only. Based on extensive reviews on the topic of MPS [22, 48], we first summarize the most important properties and the diagrammatic notation of matrix product states relevant for our results. Afterwards, we discuss bosonic NRG [16, 49] and the issue of bosonic state truncation arising in this method. In the last part, we explain how this problem can be overcome using a DMRG based technique [21], which is used to obtain the results in the remainder of this work. This chapter is only intended to make the thesis self-contained, thus not covering every detail or providing derivations.

3.1 Matrix Product States

We start by considering a 1D physical chain consisting of N equal sites with local and next-neighbor interaction only, where d denotes the dimension of the local Hilbert space on each site. Thus the Hilbert space of the total system \mathcal{H} scales exponentially with the size of the local state spaces, $\dim(\mathcal{H}) = d^N$. A generic quantum many-particle state $|\psi\rangle$ located somewhere in \mathcal{H} is given by

$$|\psi\rangle = \sum_{n_1 \dots n_N} \psi_{n_1, \dots, n_N} |n_1\rangle \dots |n_N\rangle, \quad (3.1)$$

where $n_i = 1, \dots, d$ labels the local basis states of site i . In general, the entanglement of a generic quantum state and therefore the size of its coefficient space ψ scales with system size. A proxy of the amount of entanglement present in a many-body state is given by the von-Neumann entropy

$$S(\rho_r) = -\text{Tr}[\rho_r \ln \rho_r], \quad (3.2)$$

where ρ_r is the reduced density matrix of a subregion of the chain (cf. Sec. 3.1.4). The extensive character of S for a generic state is referred to as *volume scaling*. For some specific states such as the ground state, however, the entropy scales according to an *area law* [50, 51, 52], which in case of our 1D chain indicates that the entropy stays constant with increasing system size (with logarithmic correction at criticality). In other words, only a small partition

of the total Hilbert space is necessary to give an accurate description of the ground state of a quantum many-body system.

With this in mind, we introduce the concept of matrix product states (MPS) as a convenient and efficient way to describe an a priori unknown quantum state in a 1D system. To form an MPS we decompose the coefficients in Eq. (3.1) into a product of matrices $A^{[n_k]}$,

$$|\psi\rangle = \sum_{n_1 \dots n_N} A^{[n_1]} A^{[n_2]} \dots A^{[n_N]} |n_1\rangle \dots |n_N\rangle, \quad (3.3)$$

Overall the state consists of $N \times d$ so-called A -tensors, since a matrix $A^{[n_k]}$ is associated with each of the d local states n_k on every site. The indices at the end of the chain, i.e. the first index of $A^{[n_1]}$ and the second one of $A^{[n_N]}$, only range over one value to account for open boundary conditions. Thus $A^{[n_1]}$ and $A^{[n_N]}$ have row- and column-vector shape, respectively.¹

In principle, the transformation of $|\psi\rangle$ in Eq. (3.1) into an MPS in Eq. (3.3) is formally exact, if the dimension of the A -tensors is chosen sufficiently large. Nevertheless, an exact transformation is often neither feasible in terms of numerical resources nor it is necessary considering area laws. In 1D, we still get a very good approximation of the ground state properties of our system, if we can truncate the total Hilbert space by limiting the dimensions of the A -matrices to some upper cutoff dimension D . This is achieved through the systematic use of singular value decomposition (SVD) [22].

3.1.1 Global vs. local picture

There exist two equivalent pictures when dealing with matrix product states, a global and a local picture, both having their particular application. In the global picture an MPS is written in the form of Eq. (3.3), where the state is stored in the A -tensors and formally described in terms of the product of the local Hilbert spaces $|n_1\rangle \dots |n_N\rangle$ with the main purpose of reducing resources (but without locally exploiting orthonormality properties). In this case all sites are treated equally and no special *local* site is picked out.

The local picture denotes an alternative formulation of an MPS, where we choose any specific site k as the local site of the quantum chain and combine all others to effective basis sets, so that

$$|\psi\rangle = \sum_{l_k r_k n_k} A_{l_k, r_k}^{[n_k]} |l_k\rangle |n_k\rangle |r_k\rangle, \quad (3.4)$$

where $|l_k\rangle$ and $|r_k\rangle$ are sets of states describing the left and the right part of the chain with respect to the current site k . In this picture, the $A^{[n_k]}$ -matrices give the full representation of the wavefunction, where its coefficients define a linear combinations of the orthonormal many-body basis states $|l_k\rangle$, $|n_k\rangle$ and $|r_k\rangle$. Moreover, the effective basis set $|l_k\rangle$ to the left of site k can be built up iteratively in terms of A -tensors and the local state spaces such that

$$\begin{aligned} |l_k\rangle &= \sum_{n_1 \dots n_{k-1}} (A^{[n_1]} \dots A^{[n_{k-1}]})_{l_k} |n_1\rangle \dots |n_{k-1}\rangle \\ &= \sum_{n_{k-1}} \sum_{l_{k-1}} \underbrace{\sum_{n_1 \dots n_{k-2}} (A^{[n_1]} \dots A^{[n_{k-2}]})_{l_{k-1}} |n_1\rangle \dots |n_{k-2}\rangle}_{|l_{k-1}\rangle} A_{l_{k-1}, l_k}^{[n_{k-1}]} |n_{k-1}\rangle \\ &= \sum_{n_{k-1}} A_{l_{k-1}, l_k}^{[n_{k-1}]} |l_{k-1}\rangle |n_{k-1}\rangle. \end{aligned} \quad (3.5)$$

¹While not considered in our project, MPS can also obey periodic boundary conditions. In that case the 2D matrix shape of $A^{[n_1]}$ and $A^{[n_N]}$ is kept and one traces over the open indices at the end.

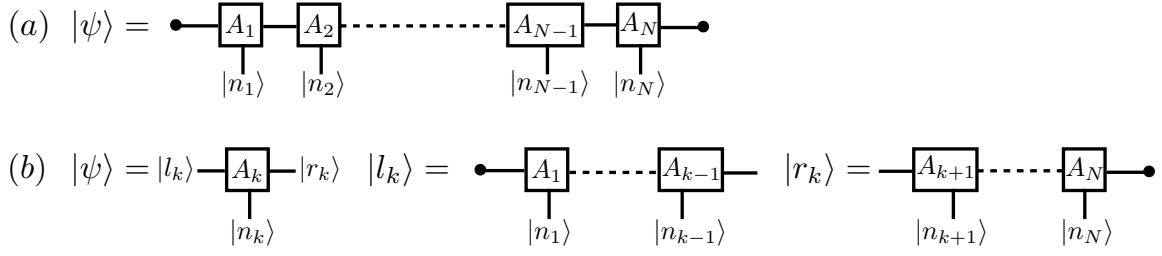


Figure 3.1: Schematic diagram of an MPS wavefunction in the (a) global and (b) local picture. In general, blocks indicate the coefficient spaces of the A -matrices and lines refer to indices, which correspond to state spaces. The open lines connect to the basis, e.g. the vertical lines correspond to the local state spaces. Indices connecting two A -matrices are summed (contracted). In case of open boundary conditions, the left and right end of an MPS is terminated by the vacuum states (small circle). Figure adapted from [48].

$A^{[n_{k-1}]}$ specifies the mapping of the effective left basis $|l_{k-1}\rangle$ combined with the local state basis n_{k-1} onto the effective left basis $|l_k\rangle$. The same applies to the effective right basis set $|r_k\rangle$, which expressed in terms of $|r_{k+1}\rangle$ and n_{k+1} by the $A^{[n_{k+1}]}$ -matrices,

$$|r_k\rangle = \sum_{n_{k+1}} A_{r_k, r_{k+1}}^{[n_{k+1}]} |r_{k+1}\rangle |n_{k+1}\rangle. \quad (3.6)$$

A graphical representation of an MPS in global and local picture is shown in Fig. 3.2. Numerical methods such as NRG or DMRG usually treat every site of the chain iteratively in the local picture and heavily employ orthonormality conditions present in this formulation. Given Eqs. (3.5) and (3.6), an iterative update towards a nearest neighbor site is the most efficient numerically.

3.1.2 Orthogonalization of effective basis sets

While a priori only the local basis states $|n_k\rangle$ in Eq. (3.4) form an orthonormal basis, we also impose orthonormality on the effective basis sets $|l_k\rangle$ and $|r_k\rangle$,

$$\langle l_k | l'_k \rangle = \delta_{ll'}, \quad (3.7)$$

$$\langle r_k | r'_k \rangle = \delta_{rr'}. \quad (3.8)$$

From the iterative structure of $|l_k\rangle$ and $|r_k\rangle$ in Eqs. (3.5) and (3.6) it follows immediately that orthonormality of the effective basis sets results in certain conditions of the A -tensors:

$$\sum_{n_i} A^{[n_i]^\dagger} A^{[n_i]} = \mathbb{I} \quad \text{if } i < k, \quad (3.9)$$

$$\sum_{n_i} A^{[n_i]} A^{[n_i]^\dagger} = \mathbb{I} \quad \text{if } i > k. \quad (3.10)$$

Note that an arbitrary MPS (even randomly initialized) can be transformed, so that the effective basis sets obey the orthonormality conditions in the local picture for any given local site k .

Assume that for a given state $|\psi\rangle$ in the local picture at site k the left effective basis set $|l_k\rangle$ is orthonormal. When we switch the current site to $k+1$ we want to ensure that $|l_{k+1}\rangle$ is an orthonormal basis set as well. This can be achieved by applying a singular value decomposition (SVD) [22] to $A^{[n_k]}$,

$$A_{l_k, r_k}^{[n_k]} = A_{(l_k \sigma_k), r_k} = (USV^\dagger)_{(l_k n_k), r_k} = \sum_{m, n} U_{(l_k n_k), m} \delta_{m, n} s_m (V^\dagger)_{n, r_k} = \sum_m U_{l_k, m}^{[n_k]} (SV^\dagger)_{m, r_k},$$

$$(a) \quad \sum_{n_i} A^{[n_i]\dagger} A^{[n_i]} = \mathbb{I}$$

$$(b) \quad \sum_{n_i} A^{[n_i]} A^{[n_i]\dagger} = \mathbb{I}$$

Figure 3.2: Graphical representation of orthonormality conditions in Eqs. (3.9) and (3.10). In (a) the contraction of a left-orthonormalized A -tensor is shown, which results in an identity tensor. The orthonormality condition in panel (a) allows to replace the explicit contraction by a direct connection of the indices r_i, r'_i allowing more efficient calculations. The same can be done for a right-orthonormalized A -tensor in (b). Figure adapted from [53].

with U and V both being column-orthonormal. S is a diagonal matrix consisting of real positive elements s_i (singular values). In the next step, we contract SV^\dagger onto $A^{[n_{k+1}]}$ and replace $A^{[n_k]}$ with U thereby ensuring that $k+1$ now has an orthonormal left basis as well:

$$A^{[n_k]} A^{[n_{k+1}]} = \sum_i A_{l_k, i}^{[n_k]} A_{i, r_{k+1}}^{[n_{k+1}]} = \sum_{i, m} U_{l_k, m}^{[n_k]} (SV^\dagger)_{m, i} A_{i, r_{k+1}}^{[n_{k+1}]} = \tilde{A}^{[n_k]} \tilde{A}^{[n_{k+1}]}, \quad (3.11)$$

as schematically depicted in Fig. 3.3. Note that this procedure does not change the overall state $|\psi\rangle$ when all singular values in S are kept. Employing this procedure systematically starting at site 1 (which by construction has the vacuum state as its an orthonormal left basis) moving to the right end, we generate an *left-canonical* MPS, where the left basis sets are orthonormal for any given site k .

Analogously, the approach works for the effective right basis: proceeding from site N (where the right basis set is orthonormal by construction) sweeping to the left end generates a *right-canonical* MPS with orthonormalized right basis sets at every site.

Figure 3.3: Diagrammatic representation of generating a orthonormalization procedure in Eq. (3.11). Applying the SVD to $A^{[n_k]}$ and contracting SV^\dagger on $A^{[n_{k+1}]}$ yields an updated $\tilde{A}^{[n_{k+1}]}$ with orthonormal left basis set $|l_{k+1}\rangle$. Figure adapted from [48].

3.1.3 Basic MPS application

Scalar product

Calculating the overlap of two states $|\psi'\rangle$ and $|\psi\rangle$ is one of the simplest operations within the MPS framework. It is calculated by contracting over the corresponding local indices of the two wave functions,

$$\begin{aligned} \langle \psi' | \psi \rangle &= \langle n'_1 | \dots \langle n'_N | \sum_{n'_1 \dots n'_N} \left(A^{[n'_1]} \dots A^{[n'_N]} \right)^* \sum_{n_1 \dots n_N} \left(A^{[n_1]} \dots A^{[n_N]} \right) |n_1\rangle \dots |n_N\rangle \\ &= \sum_{n_1 \dots n_N} \left(A'^{[n_1]} \dots A'^{[n_N]} \right)^* \left(A^{[n_1]} \dots A^{[n_N]} \right), \end{aligned} \quad (3.12)$$

where we used the orthonormality of the local basis sets, $\langle n'_k | n_l \rangle = \delta_{kl} \delta_{n'_k n_k}$. The operation is graphically depicted in Fig. 3.4.

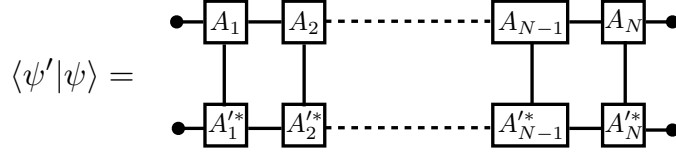


Figure 3.4: Schematic diagram of the overlap of two $|\psi'\rangle, |\psi\rangle$ in MPS notation. The calculation is carried out by contracting the corresponding local indices n_i resulting in overall scalar quantity.

Operator application

The application of a local operator to a state $|\psi\rangle$ is an essential ingredient within the DMRG procedure, which we elaborate on in Sec. 3.3. Consider an operator that acts only on two consecutive sites k and $k+1$,

$$\hat{O}^{[k,k+1]} = \sum_{n_k n'_k} \sum_{n_{k+1} n'_{k+1}} O_{(n_k, n_{k+1}), (n'_k, n'_{k+1})} |n_k, n_{k+1}\rangle \langle n'_k, n'_{k+1}|. \quad (3.13)$$

Since an MPS is naturally expressed in the local basis, the operator's affect on the wave function only at the two corresponding A -tensors,

$$\begin{aligned} \hat{O}^{[k,k+1]} |\psi\rangle &= \sum_{n_1 \dots n_N} A^{[n_1]} \dots \underbrace{\sum_{n'_k n'_{k+1}} (O_{(n_k, n_{k+1}), (n'_k, n'_{k+1})} A^{[n'_k]} A^{[n'_{k+1}]})}_{C^{[n_k, n_{k+1}]}} \dots A^{[n_N]} |n_1\rangle \dots |n_N\rangle \\ &= \sum_{n_1 \dots n_N} A^{[n_1]} \dots C^{[n_k, n_{k+1}]} \dots A^{[n_N]} |n_1\rangle \dots |n_N\rangle \\ &\stackrel{SVD}{=} \sum_{n_1 \dots n_N} A^{[n_1]} \dots \tilde{A}^{[n_k]} \tilde{A}^{[n_{k+1}]} \dots A^{[n_N]} |n_1\rangle \dots |n_N\rangle. \end{aligned} \quad (3.14)$$

In the first step, the enlarged tensor C is formed by contracting $A^{[n_k]}$ and $A^{[n_{k+1}]}$ with $\hat{O}^{[k,k+1]}$. Next, the original structure of $|\psi\rangle$ is restored by applying SVD on C truncating the from Dd^2 states down to D states by keeping the largest singular values only. This leads to properly orthonormalized new A -tensors, $\tilde{A}^{[n_k]}$ and $\tilde{A}^{[n_{k+1}]}$.

Expectation value

After having introduced how to calculate the scalar product and the operator application to an MPS, it is straightforward to evaluate an expectation value of a local operator $\hat{O}^{[k,k+1]}$. Choosing k and $k+1$ as local sites, the orthonormality conditions in Eqs. (3.9) and (3.10) with respect to the current local site k or $k+1$ allow us to compact the term in the left part of Fig. 3.5 without explicit contraction such that just four A -matrices remain,

$$\begin{aligned} \langle \psi | \hat{O}^{[k,k+1]} | \psi \rangle &= \langle n'_1 | \dots \langle n'_N | \sum_{n'_1 \dots n'_N} \sum_{n_1 \dots n_N} (A^{[n'_1]} \dots A^{[n'_N]})^* \hat{O}^{[k,k+1]} (A^{[n_1]} \dots A^{[n_N]}) |n_1\rangle \dots |n_N\rangle \\ &= \sum_{n'_k n'_{k+1} n_k n_{k+1}} (A^{[n_k]} A^{[n_{k+1}]})^* O_{(n_k, n_{k+1}), (n'_k, n'_{k+1})} A^{[n'_k]} A^{[n'_{k+1}]} \end{aligned} \quad (3.15)$$

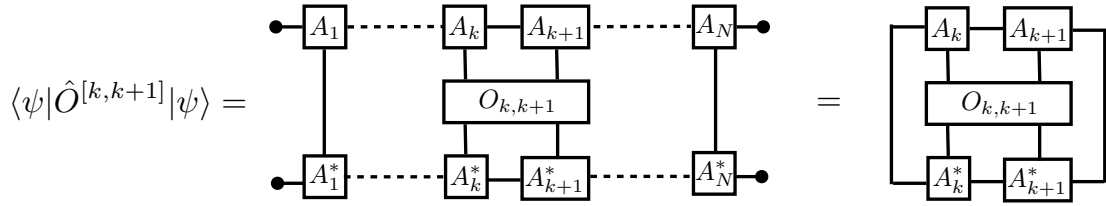


Figure 3.5: Graphical representation of the calculation of an expectation value involving a two-site local operator $\hat{O}^{[k,k+1]}$ carried out in Eq. (3.15). Using the orthonormality condition in the local picture with respect to site k or $k+1$, all A -tensors corresponding to sites unequal $k, k+1$ are eliminated from the explicit calculation. The remaining contractions that need to be performed only involve $A^{[n_k]}$, $A^{[n_{k+1}]}$ and $\hat{O}^{[k,k+1]}$.

3.1.4 Reduced density matrix and block entropy

In the beginning of the section, we have already elaborated on the important role of entanglement in MPS based numerical methods such as DMRG. Let us consider a state $|\psi\rangle$ in the local picture of site k ,

$$|\psi\rangle = \sum_{l_k r_k n_k} A_{l_k, r_k}^{[n_k]} |l_k\rangle |n_k\rangle |r_k\rangle. \quad (3.16)$$

The entanglement between left and right block of the chain can be quantified by the spectrum of the reduced density matrix, which we calculate by tracing out the right side of the system, $\rho_{n_1, \dots, n_k}^l = \text{tr}_{r_k}(|\psi\rangle\langle\psi|) = \text{tr}_{n_{k+1}, \dots, n_N}(|\psi\rangle\langle\psi|)$. Making again use of the orthonormality conditions in the local picture the expression for the reduced density matrix can be reduced to

$$\rho_{n_1, \dots, n_k}^l = \sum_{n_1 \dots n_k} \sum_{n'_1 \dots n'_k} \left(A^{[n_1]} \dots A^{[n_k]} \right)^* \left(A^{[n_1]} \dots A^{[n_k]} \right) |n_1\rangle \langle n'_1| \dots |n_k\rangle \langle n'_k| \quad (3.17)$$

$$= \sum_{l'l'} \rho_{ll'} |l_{k+1}\rangle \langle l'_{k+1}| \quad (3.18)$$

The entanglement of the two blocks is derived from the von-Neumann entropy S_k (in this context the so-called *block entropy*), which is defined by the eigenspectrum $\rho_\alpha^{(k)}$ of the reduced density matrix,

$$S_k = - \sum_{\alpha} \rho_\alpha^{(k)} \log_2(\rho_\alpha^{(k)}). \quad (3.19)$$

Strongly entangled blocks yield a high value of S_k corresponding to a more equally distributed eigenspectrum $\rho_\alpha^{(k)}$, while one dominant eigenvalue usually indicates a disentangled state. Importantly, DMRG uses the eigenspectrum of the reduced density matrix as an efficient truncation criterium: by discarding the smallest eigenvalues $\rho_\alpha^{(k)} < \epsilon \ll 1$ and the corresponding state spaces, we truncate only those parts of the Hilbert space that are most irrelevant for an accurate approximation of $|\psi\rangle$. The eigenspectrum of the reduced density matrix is equivalent to the squared singular value spectrum obtained by an SVD of $A^{[n_k]}$, i.e. $\rho_\alpha^{(k)} = [s_k]^2$ (see Sec. 3.1.2). Therefore the SVD spectrum serves as an equally efficient truncation criterium.

3.1.5 Symmetries

The matrix product state framework allows for a straightforward incorporation of preserved symmetries of the model Hamiltonian. Generally speaking, the symmetry induced selection rules cause a large number of matrix elements to be exactly zero, thus tensors become sparse. Keeping only the non-zero elements, we can achieve tremendous improvement in speed and accuracy in numerical simulations by the inclusion of symmetries. Especially for numerically demanding systems, such as multi-band models, it is crucial to exploit as many symmetries of the Hamiltonian as possible.

A. Weichselbaum [54] has recently presented a very general and transparent framework for the implementation of abelian and non-abelian symmetries for matrix product and tensor-network states. The so-called QSpace, a unified tensor representation for quantum symmetry spaces, is particularly useful to function in renormalization group algorithms such as DMRG or NRG. While in general being able to deal with complicated non-abelian symmetries, here we apply QSpace for the implementation of abelian $U(1)$ symmetries in a bosonic setting.

In this context consider a Hamiltonian \hat{H} , which is invariant under a set of n_s independent abelian symmetries, S^λ being the irreducible representation for each symmetry $\lambda = 1, \dots, n_s$. Hence, the Hamiltonian and the specific symmetry generator \hat{S}_α^λ satisfy the commutation relations $[\hat{H}, \hat{S}_\alpha^\lambda] = 0$. Furthermore $[\hat{S}_{\alpha'}^{\lambda'}, \hat{S}_\alpha^\lambda] = 0$ for $\lambda \neq \lambda'$ indicates that the symmetries act independent of each other.

For the symmetry implementation we introduce basis states $|q\rangle$ labeled in terms of the symmetry eigenbasis. The quantum labels $q \equiv (q^1, \dots, q^{n_s})$ reference the irreducible representations S^λ . Since q is conserved by the Hamiltonian, the matrix representation of \hat{H} acquires a block-diagonal structure and general tensors get subdivided into well-defined symmetry sectors. Retaining only the few remaining non-zero data blocks with an efficient bookkeeping, QSpace leads to an enormous gain in numerical efficiency.

3.2 Bosonic numerical renormalization group

The Numerical Renormalization Group (NRG) is a powerful numerical method to treat quantum impurity models. One of its major advantages and a distinct feature in comparison to other renormalization group techniques is its non-perturbative character, which allows the treatment of interacting quantum many-body systems with a continuum of excitations spread over a broad interval of energies. Since its development by Kenneth Wilson in the 1970s [12, 32], NRG has been applied to numerous quantum impurity models and thus helped to solve many questions in the field of Kondo physics, transport or dissipation [55, 56, 57, 58, 59, 60, 61].

There exists only one major restriction regarding the applicability of NRG on specific quantum impurity models. Many-body interactions affect only the impurity, the bath or reservoir of the model is considered to be non-interacting. Apart from that, the bath generally can be consisting of bosonic (e.g. phonons, magnons, particle-hole pairs etc.) or fermionic particle (e.g. electrons in the conduction band), while the setup of the impurity is not constrained at all.

For almost three decades NRG was exclusively applied to fermionic models such as the single impurity Anderson model or the single and multi-channel Kondo models. Only in 2003, Bulla et al. [16] employed NRG for the first time in a bosonic context, i.e. to calculate the critical properties of the Spin-Boson model. Why did it take almost 30 years to transfer the method to bosonic systems? It turns out that bosonic bath are far more complicated to manage numerically compared to their fermionic counterparts. Since Pauli's principle prevents that two fermions occupy the same state, the local fermionic Hilbert space dimension stays finite and small. However, each bosonic state can be occupied by an infinite number of bosons yielding infinitely large local Hilbert spaces, which make numerical approaches far more complicated. An efficient numerical treatment of this issue arising from the fundamental nature of the particles will be the major topic of the following sections.

Since we focus in this work on bosonic quantum impurity models, we introduce NRG in the context of bosonic baths only, following [49]. After reviewing the basic steps of the NRG procedure, we shortly discuss the connection between NRG and MPS pointed out by [43] and comment on the main problem of bosonic NRG [62]. For a general overview on NRG we refer to the review of Bulla et al. [13].

3.2.1 Spin-Boson model

While bosonic NRG can be applied to a variety of quantum impurity models involving a bosonic bath with a continuous spectrum, we base the discussion of the conceptual steps on the spin-boson model, the first application of bosonic NRG [16]. Since a detailed analysis of the physical properties of the model is presented later on in Chap. 4, for now we only introduce the basic features of the model which are essential for the understanding of bosonic NRG. We start with the Hamiltonian of the continuous version of the spin-boson model, which is given by

$$\hat{H} = \underbrace{\frac{\epsilon}{2}\hat{\sigma}_x - \frac{\Delta}{2}\hat{\sigma}_z}_{\hat{H}_{imp}} + \underbrace{\sum_i \omega_i \hat{a}_i^\dagger \hat{a}_i}_{\hat{H}_{bath}} + \underbrace{\frac{\hat{\sigma}_x}{2} \sum_i \lambda_i (\hat{a}_i + \hat{a}_i^\dagger)}_{\hat{H}_{coupling}}. \quad (3.20)$$

The impurity consists of a generic two-state system, represented by the Pauli matrices $\hat{\sigma}_{x,z}$, linearly coupled by λ_i to a bath of harmonic oscillators with creation operators a_i and frequencies ω_i , the coupling being with respect to the position $\hat{x} = 1/\sqrt{2}(\hat{a}_i + \hat{a}_i^\dagger)$ of each

oscillator. ϵ is an additional bias in coupling direction and Δ gives the bare tunneling amplitude between the two spin eigenstates $|+\rangle$ and $|-\rangle$ of $\hat{\sigma}_x$. The effect of the bath on the impurity is fully determined by the bath spectral function,

$$J(\omega) = \pi \sum_i \lambda_i^2 \delta(\omega - \omega_i), \quad (3.21)$$

generally defined by the density of states of the bath $\rho(\omega)$ and the coupling $\lambda(\omega)$. For the description of asymptotic low-temperature behavior of the model only the low-energy spectrum of the bath plays a role. Therefore in the standard parametrization of the spectral function only frequencies up to a critical frequency ω_c are taken into account and the high energy spectrum is neglected. Usually a power law form is chosen,

$$J(\omega) = 2\pi\alpha\omega_c^{1-s}\omega^s, \quad 0 < \omega < \omega_c, \quad s > 0, \quad (3.22)$$

where the dimensionless constant α indicates the dissipation strength. Depending on the value of s , we distinguish between 'ohmic' ($s = 1$), 'sub-ohmic' ($s < 1$) and 'super-ohmic' ($s > 1$) dissipation. In the following, we set ω_c to 1 as the unit of energy.

3.2.2 Logarithmic discretization

Similar to other numerical settings, we first need to apply some sort of coarse-graining to the continuous bath. While there are many ways to discretize such a system generally, NRG works with a logarithmic discretization scheme. This choice is motivated by the fact, that for many quantum impurity models the relevant energy scales can become exponentially small. To resolve these scales appropriately a logarithmic coarse-graining is required, since it yields an exponentially enhanced low-energy resolution compared to a linear discretization. Moreover, a logarithmic discretization separates consecutive energy intervals and therefore allows a controlled numerical treatment within the iterative diagonalization procedure.

To discretize the spectral function of a bosonic bath it is convenient to start at the continuous version of the SBM Hamiltonian by replacing the discrete sum over the bath modes by a continuous interval over the energy variable ϵ and substituting $\hat{a}_i \rightarrow \hat{a}_\epsilon/\sqrt{\rho(\epsilon)}$, with $[\hat{a}_\epsilon, \hat{a}_{\epsilon'}^\dagger] = \delta(\epsilon - \epsilon')$ and $\rho(\epsilon)$ being the bath density of states. Thus the spin-boson Hamiltonian in Eq. (3.20) takes the form

$$\hat{H} = \hat{H}_{imp} + \int d\omega (\omega \hat{a}_\omega^\dagger \hat{a}_\omega) + \frac{\hat{\sigma}_x}{2} \int d\omega \sqrt{\rho(\omega)} \lambda(\omega) (\hat{a}_\omega + \hat{a}_\omega^\dagger), \quad (3.23)$$

where $\rho(\omega)$ and the coupling function $\lambda(\omega)$ are related to the spectral function $J(\omega)$ via

$$\frac{1}{\pi} J(\omega) = \rho(\omega) [\lambda(\omega)]^2. \quad (3.24)$$

The spectral function of a bosonic bath is defined in the interval $[0, \omega_c = 1]$ and is therefore restricted to positive energies only. To logarithmically discretize the bath spectral function, we introduce the dimensionless parameter $\Lambda > 1$ which defines a set of intervals with discretization points,

$$\omega_n = \Lambda^{-n} \quad n = 0, 1, 2, \dots \quad (3.25)$$

The width of each energy interval is given by $d_n = \Lambda^{-n}(1 - \Lambda^{-1})$. Within each interval n a complete set of orthonormal functions can be defined,

$$\Psi_{np}(\omega) = \begin{cases} \frac{1}{\sqrt{d_n}} e^{i\omega_n p \omega} & \text{for } \Lambda^{-(n+1)} < \omega < \Lambda^{-n}, \\ 0 & \text{outside this interval,} \end{cases} \quad (3.26)$$

with $p = 0, \pm 1, \pm 2, \dots$, and $\omega_n = 2\pi/d_n$. The creation and annihilation operators \hat{a}_ω^\dagger and \hat{a}_ω can be represented in this basis,

$$\hat{a}_\omega = \sum_{np} \hat{a}_{np} \Psi_{np}(\omega) \quad (3.27)$$

$$\hat{a}_\omega^\dagger = \sum_{np} \hat{a}_{np}^\dagger \Psi_{np}^*(\omega). \quad (3.28)$$

Since the impurity only couples to the $p = 0$ component of the bosonic operators \hat{a}_{np}^\dagger and \hat{a}_{np} , we neglect other contributions $p \neq 0$ although those components are still linked to the $p = 0$ components of the free bath (very similar to the fermionic case). Thus a single annihilation and creation operator now represents the continuous spectrum of bosonic modes in each energy interval n . In the next step we redefine the creation and annihilation operators in each interval,

$$\hat{a}_n \equiv \frac{1}{\sqrt{N_n^2}} \int_{\Lambda^{-(n+1)}}^{\Lambda^{-n}} \sqrt{\frac{J(\omega)}{\pi}} \hat{a}_{n0} \Psi_{n0} d\omega, \quad (3.29)$$

$$\hat{a}_n^\dagger \equiv \frac{1}{\sqrt{N_n^2}} \int_{\Lambda^{-(n+1)}}^{\Lambda^{-n}} \sqrt{\frac{J(\omega)}{\pi}} \hat{a}_{n0}^\dagger \Psi_{n0} d\omega, \quad (3.30)$$

where the normalization N_n is chosen such that the bosonic commutator relation $[\hat{a}_n, \hat{a}_{n'}^\dagger] = \delta_{nn'}$ holds:

$$N_n^2 = \int_{\Lambda^{-(n+1)}}^{\Lambda^{-n}} \frac{J(\omega)}{\pi} d\omega. \quad (3.31)$$

Splitting the continuous spin-boson Hamiltonian of Eq. (3.23) into a sum of integrals over the discretized intervals and employing Eqs. (3.29) and (3.30), we arrive at the discretized "star" Hamiltonian

$$\hat{H}_{star} = \hat{H}_{imp} + \sum_n \xi_n \hat{a}_n^\dagger \hat{a}_n + \frac{\hat{\sigma}_x}{2\sqrt{\pi}} \sum_n \gamma_n (\hat{a}_n + \hat{a}_n^\dagger), \quad (3.32)$$

where

$$\gamma_n^2 = \int_{\Lambda^{-n}}^{\Lambda^{-(n+1)}} J(\omega) d\omega = \frac{2\pi\alpha}{s+1} (1 - \Lambda^{-(s+1)}) \Lambda^{-n(s+1)}, \quad (3.33)$$

$$\xi_n = \gamma_n^{-2} \int_{\Lambda^{-n}}^{\Lambda^{-(n+1)}} J(\omega) \omega d\omega = \frac{s+1}{s+2} \frac{1 - \Lambda^{-(s+2)}}{1 - \Lambda^{-(s+1)}} \Lambda^{-n}. \quad (3.34)$$

In the last step we used the standardized form of the bath spectral function in Eq. (3.22) to evaluate the integrals defining ξ_n and γ_n .

The "star" label of the discretized Hamiltonian in Eq. (3.32) indicates its structure: the impurity couples to bosonic modes of all energy scales very similar as in the original spin-boson Hamiltonian. However, now each bosonic degree of freedom represents the continuous spectrum of bosonic modes within its energy interval.

3.2.3 Mapping onto the Wilson tight-binding chain

Following the standard NRG methods, the discretized "star"-Hamiltonian is mapped exactly into a semi-infinite chain with only nearest-neighbor interaction. In the NRG framework such a setup is referred to as Wilson-chain. The mapping procedure involves a unitary

transformation for the bosonic annihilation and creation operators, $\hat{b}_n = \sum_{m=0}^{\infty} U_{nm} \hat{a}_m$, and can be carried out numerically by standard tridiagonalization procedures (e.g. Lanczos algorithm).

The resulting "chain" Hamiltonian generated by the mapping of Eq. (3.32) is given by

$$\hat{H}_{chain} = \hat{H}_{imp} + \sqrt{\frac{\eta_0}{\pi}} \frac{\hat{\sigma}_x}{2} (\hat{b}_0 + \hat{b}_0^\dagger) + \sum_{n=0}^{\infty} [\epsilon_n \hat{b}_n^\dagger \hat{b}_n + t_n (\hat{b}_n^\dagger \hat{b}_{n+1} + \hat{b}_{n+1}^\dagger \hat{b}_n)], \quad (3.35)$$

with $\eta_0 = \int J(\omega) d\omega$ describing the overall coupling between bath and impurity, which is located on the first site of the chain. Note that the impurity spin now couples to the second site (i.e. the first bosonic site) of tight-binding chain only. Each bosonic site is connected to its direct neighbors by the hopping amplitude t_n and obtains an on-site energy ϵ_n . The parameters ϵ_n and t_n decay exponentially as Λ^{-n} and are calculated numerically from the spectral function $J(\omega)$ (for details see App. 1 in [49]). Note that ϵ_n and t_n fall off as $\Lambda^{-n/2}$ in the fermionic case. This difference arises from the absence of holes for bosonic baths.

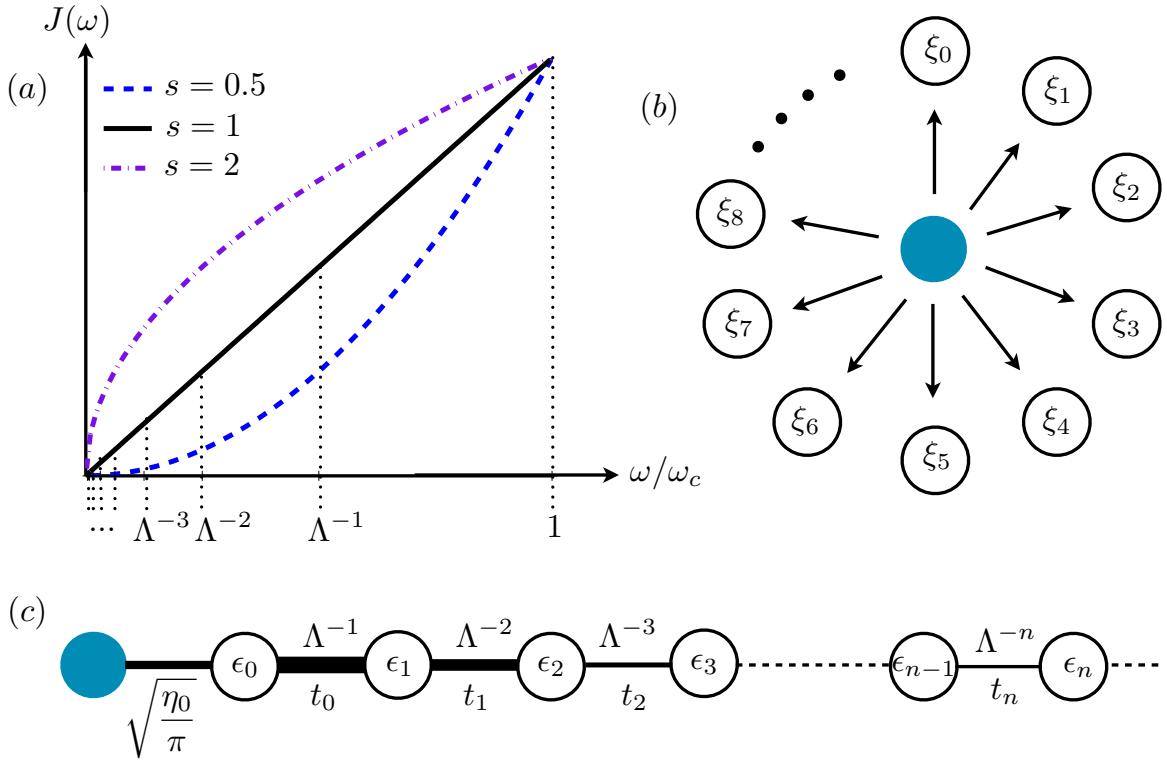


Figure 3.6: (a) Spectral function $J(\omega)$ of a bosonic bath in the spin-boson model for ohmic ($s = 1$), sub-ohmic ($s = 0.5$) and super-ohmic ($s = 2$) dissipation. The logarithmic discretization of $J(\omega)$ leads to a Hamiltonian of "star"-structure schematically illustrated in (b), where the impurity (blue) still couples to each bath oscillator individually. The discretized Hamiltonian is then exactly mapped onto the semi-infinite tight-binding chain in (c), where the exponentially decaying energy scale is illustrated by thinning bonds between different sites. In the Wilson chain Hamiltonian, the impurity couples only to the first bosonic site.

3.2.4 Iterative diagonalization

After mapping the discretized Hamiltonian on a Wilson chain, we solve the model with an iterative diagonalization procedure. This is achieved by writing \hat{H}_{chain} as a series of Hamiltonians $\hat{H}_N (N \geq 0)$ that equal \hat{H}_{chain} in the limit $N \rightarrow \infty$,

$$\hat{H} = \lim_{N \rightarrow \infty} \Lambda^{-N} \hat{H}_N, \quad (3.36)$$

with \hat{H}_N being a rescaled version of \hat{H} including only N sites of the Wilson chain,

$$\hat{H}_N = \Lambda^N \left[\hat{H}_{imp} + \sqrt{\frac{\eta_0}{\pi}} \frac{\hat{\sigma}_x}{2} (\hat{b}_0 + \hat{b}_0^\dagger) + \sum_{n=0}^N \epsilon_n \hat{b}_n^\dagger \hat{b}_n + \sum_{n=0}^{N-1} t_n (\hat{b}_n^\dagger \hat{b}_{n+1} + \hat{b}_{n+1}^\dagger \hat{b}_n) \right]. \quad (3.37)$$

Two successive Hamiltonians are related by the recurrence relation

$$\hat{H}_{N+1} = \Lambda \hat{H}_N + \Lambda^{N+1} [\epsilon_{N+1} \hat{b}_{N+1}^\dagger \hat{b}_{N+1} + t_N (\hat{b}_N^\dagger \hat{b}_{N+1} + \hat{b}_{N+1}^\dagger \hat{b}_N)]. \quad (3.38)$$

The rescaling factor Λ^N allows us to directly compare the low energy spectrum of subsequent Hamiltonians and with each additional site we get a better resolution of the low-energy spectrum of \hat{H} .

The starting point of the iterative NRG procedure is \hat{H}_0 consisting only of the impurity and the first bosonic site,

$$\hat{H}_0 = \hat{H}_{imp} + \sqrt{\frac{\eta_0}{\pi}} \frac{\hat{\sigma}_x}{2} (\hat{b}_0 + \hat{b}_0^\dagger) + \epsilon_0 \hat{b}_0^\dagger \hat{b}_0. \quad (3.39)$$

Diagonalizing \hat{H}_0 in a basis formed by the product states of the σ_x -eigenstates $|\sigma\rangle$ and an appropriate basis $|n_0\rangle$ for the first bath site (see Sec. 3.2.6 for details), we obtain a set of eigenenergies and eigenstates. In each subsequent step we construct the rescaled \hat{H}_{N+1} according to Eq. (3.38) in terms of the eigenstates $|s_N\rangle$ of \hat{H}_N and the bosonic state basis $|n_{N+1}\rangle$ of the additional site. By diagonalization of \hat{H}_{N+1} we obtain a new set of eigenstates $|s_{N+1}\rangle$ which connects to the old states $|s_N\rangle$ via a unitary transformation $A^{[N]}$,

$$|s_{N+1}\rangle = \sum_{n_{N+1}, s_N} A_{s_N, s_{N+1}}^{[n_{N+1}]} |s_N\rangle |n_{N+1}\rangle, \quad (3.40)$$

where $A^{[N+1]}$ represents the d A -matrices that link to the underlying product space $|s_N\rangle \otimes |n_{N+1}\rangle$ ($d < \infty$ referring to the dimension of the added local state space). We notice that the transformation in Eq. (3.40) shows a structure similar to an MPS in the local picture (cf. Eq. (3.3)). Based on this observation, NRG can be fully reformulated in the MPS language leading to advantages in many applications [63, 53].

Retaining all eigenstates obtained by diagonalization of \hat{H}_{N+1} is numerically not feasible for the complete iterative procedure as the Hilbert space grows exponentially with each added site. It is necessary to truncate the state space after the first iteration by keeping only a fixed number of D lowest lying eigenstates as indicated in Fig. 3.7(a). In the context of truncation we again stress the importance of the logarithmic discretization. If the discarded states should have no influence on later iterations, then their energy scales should sufficiently be separated from those in successive iterations. The energy scale separation is achieved only by a logarithmic coarse graining. Following this idea an alternative truncation criterium is to keep eigenstates up to some rescaled energy E_{keep} instead of a fixed number. However, it is a priori not clear which specific choice of the truncation parameters D or E_{keep} is optimal for the individual model. Therefore NRG calculations must always include a validation criterium to check whether the results are converged (e.g. discarded weight [64]).

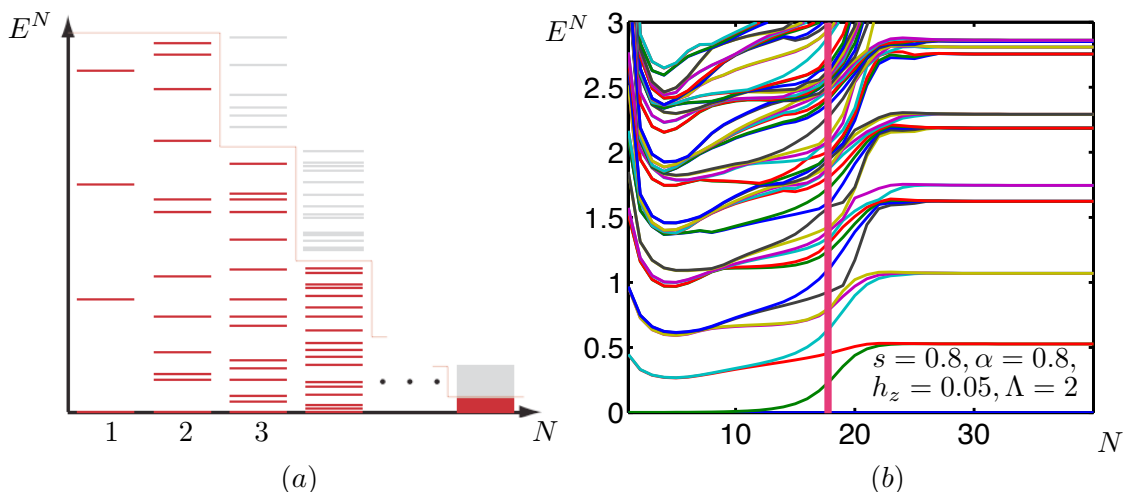


Figure 3.7: (a) Sketch of unscaled energy levels at different NRG iterations with ground state energy set to zero. After the second step we start discarding the high energy states in the spectrum (grey) thus obtaining a highly resolved low energy spectrum at iteration N . (b) Typical energy-level flow diagram of $U(1)$ symmetric two-channel spin-boson model. For the first 10 iterations, the system resides in the localized regime where the impurity strongly couples to the bosonic baths and thus localizes in coupling direction. Between iterations 10-20, the system flows to a delocalized fixed point lifting the two-folded ground state degeneracy. The red bar indicates the cross-over at iteration $N^* = 18$ characterized by the low-energy scale $T^* \propto \Lambda^{-N^*} \approx 3 \cdot 10^{-06}$.

3.2.5 Renormalization group flow

The recursion formula in Eq. (3.38) points out the renormalization group character of NRG, because its structure is similar (but not equivalent) to a standard RG transformation. We have already discussed in Sec. 2.1.3, that a renormalized Hamiltonian can be described by an effective Hamiltonian with a given set of parameters that changes during the RG transformation. Usually, after a sufficient number of iterations, the parameters approach a fixed point, where additional RG transformations leave the set of parameters invariant. Thus by studying the parameter flow we can extract information about the physics of the underlying model.

Since the Hamiltonian changes its form after each iteration in NRG, the RG flow concept has to be adapted. Instead of studying the parameter flow, we can examine the flow of the rescaled eigenenergies E_N along the Wilson chain sites N to identify different fixed points connecting to different physical behavior of the specific system. The energy-flow diagram of the two-channel spin-boson model is shown in Fig. 3.7(b) as an example, where we can distinguish two regimes: for the first 15 sites the system is localized while it flows to a delocalized fixed point for later iterations.

Note that for a bosonic model we observe no even-odd effects in the energy flow. This is another difference to the fermionic case, where the spectrum usually oscillates between two sets of energy levels for even and odd iterations.

3.2.6 Choice of bosonic basis

In the previous discussion of the bosonic NRG procedure we only touched the most important difference in comparison to the fermionic setup on the surface. We face two major problems

when setting up the local bosonic basis $|n_N\rangle$ on each site of the Wilson chain that are not present for a fermionic model:

1. Since bosonic occupation numbers are not limited by Pauli's principle, a single local bosonic state space in principle includes infinitely many states. In the numerical approach we have to truncate each local basis set $|n_k\rangle$ to a finite number of d_k states (typically $d_k \approx 25$). Therefore bosonic NRG carries a non-trivial truncation error from the very first iteration, which has to be monitored carefully.
2. We have to select d_k states from the infinitely large bosonic basis, that give the best description of the lowest-lying eigenstates of H_{N+1} .

These problems combined pose a serious challenge to any bosonic NRG procedure, especially since the different regimes of the spin-boson model require different choices of an optimal bosonic basis. This is illustrated best by considering a mean-field version of the original spin-boson Hamiltonian in Eq. (3.20),

$$\hat{H}_{MF} = \hat{H}_{spin} + \hat{H}_{boson} \quad (3.41)$$

$$\hat{H}_{spin} = \frac{\epsilon}{2}\hat{\sigma}_x - \frac{\Delta}{2}\hat{\sigma}_z + \frac{\hat{\sigma}_x}{2} \sum_i \lambda_i \langle \hat{a}_i + \hat{a}_i^\dagger \rangle \quad (3.42)$$

$$\hat{H}_{boson} = \frac{\langle \hat{\sigma}_x \rangle}{2} \sum_i \lambda_i (\hat{a}_i + \hat{a}_i^\dagger) + \sum_i \omega_i \hat{a}_i^\dagger \hat{a}_i. \quad (3.43)$$

At the delocalized fixed point the magnetization of the impurity spin is equal to zero, $\langle \hat{\sigma}_x \rangle = 0$. Hence, the coupling term in \hat{H}_{boson} vanishes and it is clear, that the lowest-lying eigenstates of H_{N+1} can be constructed from the undisplaced lowest bosonic excitations. Thus the optimal basis choice is formed by the d_k lowest eigenstates $|n_i\rangle$ of $\hat{a}_i^\dagger \hat{a}_i$, with $\hat{a}_i^\dagger \hat{a}_i |n_i\rangle = n_i |n_i\rangle$.

The situation is different at the localized fixed point where we obtain a finite magnetization, $\langle \hat{\sigma}_x \rangle \neq 0$. Now we can't drop the coupling term in Eq. (3.43) with the consequence, that each bosonic mode \hat{a}_i acquires a displacement $\delta_i \propto \lambda_i \langle \hat{\sigma}_x \rangle / (2\omega_i)$, i.e.

$$\hat{a}'_i = \hat{a}_i + \delta_i. \quad (3.44)$$

Therefore displaced oscillators are the optimal choice of the basis set in the localized regime to construct the lowest-lying set of eigenstates of H_{N+1} . However, the displacements δ_i are generally not known a priori and grow exponentially in the Wilson chain setup with each iteration, which poses a severe challenge for any NRG implementation. Thus no complete algorithm exists to setup an optimal bosonic basis for the complete parameter spectrum of the spin-boson model. While there have been attempts to incorporate a displaced basis in the NRG [49], most bosonic NRG applications are calculated with an undisplaced local basis set. This leads to huge systematic errors, especially when calculating critical properties [62, 65].

The bosonic basis problem motivated Guo et al. [21] to develop a DMRG based method, that overcomes this issue by finding the displacement δ_i variationally, thus allowing a controlled and efficient treatment of any bosonic impurity model. A detailed introduction of this variational approach is given in Sec. 3.3.

3.3 Variational matrix product states

Although NRG has been widely successful in the non-perturbative calculation of the static and dynamic properties of numerous quantum impurity models, it fails in the application to real-space lattice models such as the Hubbard model, which feature constant hopping amplitudes. This inspired Steven White to develop the Density Matrix Renormalization Group (DMRG) to solve one-dimensional lattice models [14, 66]. Opposed to NRG, which still contains the essential features of a renormalization group approach, DMRG should be understood as a variational method (despite of its name).

People quickly became excited about DMRG, since it allows very efficient and accurate description of ground-state properties of interacting 1D real-space lattice models. Extensions of static DMRG to the calculation of dynamical [67, 68] and thermodynamical properties [69, 70] were developed, different approaches of generalizing the method to higher dimensional systems have been introduced [71, 72, 73, 74, 75]. Moreover, it was shown that DMRG can fully be reformulated in terms of matrix product states [44, 76, 77, 22]. In the MPS setting, the DMRG algorithm works as a variational optimization scheme, in which the ground-state energy is minimized in the space of all matrix product states. In this context, the term variational matrix product state (VMPS) often replaces the acronym DMRG. The MPS framework not only simplified the implementation of the method, but it also helped to put DMRG on a solid theoretical basis using insights already known from quantum information theory (e.g. discussion on area laws in Sec. 3.1).

In 2005, Weichselbaum et al. [63] showed that the iterative NRG procedure can be understood in the language of MPS, as well. Applied to a Wilson chain, both methods produce similar MPS representations of the ground state of the model. However, the results are not equivalent since VMPS and NRG use two different truncation criteria to keep the size of effective Hilbert space numerically feasible. While NRG discards the highest-energy eigenstates of a series of effective Hamiltonians, VMPS truncation relies on the singular value decomposition of the matrices composing the MPS. Correspondingly, the energy-scale separation imbedded in the NRG procedure is in general not required in the VMPS setup.

The application of VMPS compared to NRG can be - but does not have to be - advantageous with respect to numerical efficiency and accuracy. Which of the methods is the better choice depends essentially on the quantum impurity model. A detailed comparison of the two approaches applied to fermionic models is given in [47]. For systems with bosonic baths VMPS should always be the preferred method, since it allows - in contrast to NRG - the implementation of an optimal displaced oscillator basis.

3.3.1 Variational ground state calculation

The VMPS procedure can be understood as a variational optimization scheme working within the MPS space. In general, we start with a given 1D Hamiltonian \hat{H} (e.g. the chain Hamiltonian of the spin-boson model in Eq. (3.32) including N sites) and generate a random and properly orthonormalized state $|\psi\rangle$. Next, we try to find an optimal approximation for the ground state of the system, by gradually reducing the energy $E = \langle\psi|\hat{H}|\psi\rangle/\langle\psi|\psi\rangle$ treating one site at a time. Given $|\psi\rangle$ in the local picture at site k ,

$$|\psi\rangle = \sum_{l_k r_k n_k} A_{l_k r_k}^{[n_k]} |l_k\rangle |n_k\rangle |r_k\rangle, \quad (3.45)$$

this is achieved by iterative varying E with respect to the local $A^{[n_k]}$ -matrices while keeping all other A -tensors constant,

$$\min[E] = \frac{\langle \psi | \hat{H} | \psi \rangle}{\langle \psi | \psi \rangle} \rightarrow \frac{\partial}{\partial A_k^*} \frac{\langle \psi | \hat{H} | \psi \rangle}{\langle \psi | \psi \rangle} = 0. \quad (3.46)$$

The optimization problem in Eq. (3.46) can be transformed into an eigenvalue problem within the local Hilbert space spanned by $|l_k\rangle \otimes |n_k\rangle \otimes |r_k\rangle$. Since we are mainly interested in the ground state of the system, it is not necessary to diagonalize \hat{H} exactly (which usually turns out to be impossible even in the local picture due to the size of \hat{H}). It suffices to calculate $\hat{H}|\psi\rangle$ in the local picture of site k and to determine the optimized ground state with the help of a sparse eigensolver (employing Lanczos or Davidson algorithm [78, 79]).

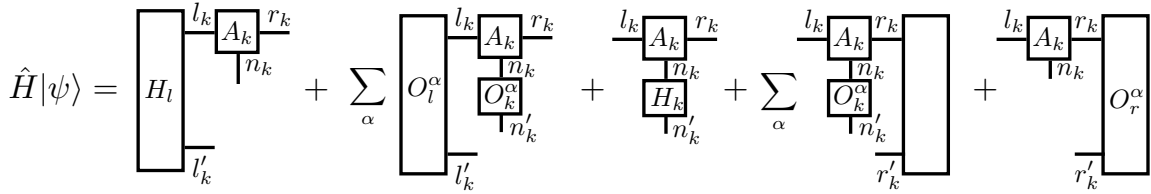


Figure 3.8: Graphical representation of application of the Hamiltonian \hat{H} to $|\psi\rangle$ during the VMPS optimization step. The five different parts of the Hamiltonian are transformed into the effective local basis of site k .

To this end we transform the Hamiltonian in the effective state basis of site k and split it into five parts,

$$\hat{H}_k = \hat{H}^{[l]} + \hat{H}^{[l,k]} + \hat{H}^{[k]} + \hat{H}^{[k,r]} + \hat{H}^{[r]}, \quad (3.47)$$

with each part represented in the basis $|l_k\rangle \otimes |n_k\rangle \otimes |r_k\rangle$, as illustrated in Fig. 3.8:

- $\hat{H}^{[l]} = \hat{H}^{[l]} \otimes \mathbb{I}^{[k]} \otimes \mathbb{I}^{[r]}$ acts only at the left part of the chain
- $\hat{H}^{[l,k]} = \sum_{\alpha} \hat{O}_{\alpha}^{[l]} \otimes \hat{O}_{\alpha}^{[k]} \otimes \mathbb{I}^{[r]}$ is the coupling between left part of the chain and local site k
- $\hat{H}^{[k]} = \mathbb{I}^{[l]} \otimes \hat{H}^{[k]} \otimes \mathbb{I}^{[r]}$ acts only at the local site
- $\hat{H}^{[k,r]} = \mathbb{I}^{[l]} \otimes \sum_{\alpha} \hat{O}_{\alpha}^{[k]} \otimes \hat{O}_{\alpha}^{[r]}$ is the coupling between local site k and right part of the chain
- $\hat{H}^{[r]} = \mathbb{I}^{[l]} \otimes \mathbb{I}^{[k]} \otimes \hat{H}^{[r]}$ acts only at the right part of the chain.

Here, $\mathbb{I}^{[l]}, \mathbb{I}^{[k]}, \mathbb{I}^{[r]}$ describe identity matrices in respective spaces. While the representation of $\hat{H}^{[k]}$ and $\hat{O}_{\alpha}^{[k]}$ is trivially given in the local state space of site k , the other terms require an iterative transformation into the effective basis of site k first.

$\hat{O}_{\alpha}^{[l]}$ and $\hat{O}_{\alpha}^{[r]}$ are constructed by transforming the basis of the operators $\hat{O}_{\alpha}^{[k-1]}, \hat{O}_{\alpha}^{[k+1]}$ from their local bases sets $|n_{k-1}\rangle$ and $|n_{k+1}\rangle$ to the effective basis sets $|l_k\rangle$ and $|r_k\rangle$, respectively. After applying the basis transformation, we can combine them with their respective

counterparts $\hat{O}_\alpha^{[k]}$ to a part of the Hamiltonian. The construction of $\hat{H}^{[l,k]}$ is given by

$$\hat{H}_{l_k, l'_k, n_k, n'_k}^{[l,k]} = \sum_\alpha \sum_{n_{k-1}, n'_{k-1}, l_{k-1}} \left((A_{l_{k-1}, l'_k}^{[n_{k-1}]})^* \hat{O}_{n_{k-1}, n'_{k-1}}^{[k-1], \alpha} A_{l_{k-1}, l_k}^{[n_{k-1}]} \right) \hat{O}_{n_k, n'_k}^{[k], \alpha} \quad (3.48)$$

$$= \sum_\alpha \hat{O}_{l_k, l'_k}^{[l], \alpha} \hat{O}_{n_k, n'_k}^{[k], \alpha}. \quad (3.49)$$

Analogously we form $\hat{H}^{[r,k]}$ by a similar calculation:

$$\hat{H}_{n_k, n'_k, r_k, r'_k}^{[r,k]} = \sum_\alpha \hat{O}_{n_k, n'_k}^{[k], \alpha} \sum_{n_{k+1}, n'_{k+1}, r_{k+1}} \left((A_{r_{k+1}, r'_k}^{[n_{k+1}]})^* \hat{O}_{n_{k+1}, n'_{k+1}}^{[k+1], \alpha} A_{r_{k+1}, r_k}^{[n_{k+1}]} \right) \quad (3.50)$$

$$= \sum_\alpha \hat{O}_{n_k, n'_k}^{[k], \alpha} \hat{O}_{r_k, r'_k}^{[r], \alpha}. \quad (3.51)$$

The Hamiltonians affecting the right and the left block of the chain, $\hat{H}^{[l]}$ and $\hat{H}^{[r]}$, are constructed iteratively from $\hat{H}^{[r,k]}$ and $\hat{H}^{[l,k]}$ [48].

In this work, VMPS is solely applied to bosonic Wilson-chain Hamiltonians (e.g. Eq. (3.32)), where energy scale decays exponentially across the chain as $\propto \Lambda^{-k}$. For such models it is highly recommended to replicate the rescaling procedure known from NRG. Otherwise, we lose numerical accuracy at higher iteration due to the limits of numerical double precision. Before the calculation of the sparse eigensolver is carried out, we therefore multiply \hat{H}_k in Eq. (3.47) by an appropriate rescaling factor Λ^k to ensure that optimization can take place on the effective energy scale $\propto \omega_c$.

Sweeping and convergence

By running the sparse eigensolver we create an optimized A -tensor $A'^{[n_k]}$ which minimizes the energy of $|\psi\rangle$ in the matrix space of all local A -tensors at site k . Therefore replacing $A^{[n_k]}$ with its optimized version $A'^{[n_k]}$ generates an improved approximation of the ground state.

Since VMPS suffers from the same problem of an exponentially growing Hilbert space as NRG, a truncation of the state space is required after each optimization step. This is usually done when switching the current site to $k \pm 1$ using SVD, as discussed in Sec. 3.1.2. Instead of performing an exact SVD, we keep only the D largest singular values and discard those states having the smallest relevance for a proper approximation of the ground state. After switching to a neighboring site, the optimization routine is repeated for $A'^{[n_{k \pm 1}]}$.

Usually, the VMPS procedure is started at the first site of the chain and then moves to the right end optimizing the A -tensors site by site. After reaching the end of the chain, the process is carried out in the other direction. By moving twice through the chain (from left to right and back again) we complete one "sweep".² After each sweep, we check the convergence of $|\psi\rangle$ by calculating the variance of the (unscaled) ground state energy E_k calculated at each site $k \in [1, N]$ units,

$$\text{var}(E_k) = \frac{\text{std}(E_k)}{|\bar{E}|}, \quad (3.52)$$

where N is the chain length, \bar{E} the average value of E_k and $\text{std}(E_k)$ defines the standard deviation

$$\text{std}(E_k) = \sqrt{\frac{1}{N-1} \sum_k (E_k - \bar{E})^2}. \quad (3.53)$$

²For a Wilson chain Hamiltonian it suffices to only sweep from left to right, since the right part of the chain has negligible influence on the first iterations due to the exponentially decaying energy scale.

If we find $\text{var}(E_k)$ to be smaller than some lower bound $\epsilon \approx 10^{-13} - 10^{-15}$, the optimization procedure is stopped and the resulting state $|\psi\rangle$ is considered to be a reliable approximation of the system's ground state. Otherwise, successive sweeps are carried out until $\text{var}(E_k)$ drops below ϵ .

3.3.2 Optimal bosonic basis and shift

As discussed in Sec. 3.2.6, the Hilbert-space truncation limits the applicability of NRG to quantum impurity models with bosonic baths. However, recent work by Guo et al. [21] showed how to overcome problem by using a VMPS based method. A general algorithm is presented which allows to study bosonic quantum impurity models across the entire phase diagram by setting up an optimal bosonic basis of displaced oscillators variationally. As most of our results are obtained using this procedure, we introduce the basic steps of the method in the following (more details can be found in [80]).

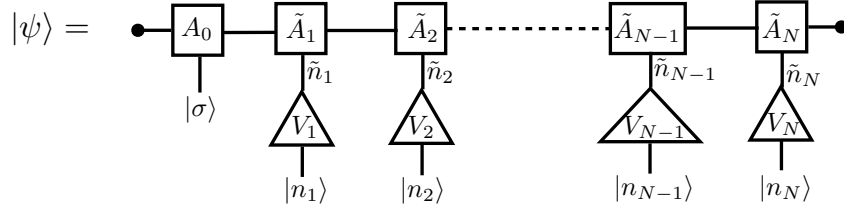


Figure 3.9: Schematic diagram of $|\psi\rangle$ in the OBB representation. A_0 links to the impurity at the first site of the Wilson chain, while all other sites have a local bosonic basis n_k . The V -matrices transform the original (large) local basis set to an optimal (smaller) basis set used for the optimization of the \tilde{A} -tensors.

The main advantage of VMPS in comparison to NRG is that it allows to change the local basis during the sweeping, while in NRG the local basis is fixed after adding the site to the chain. To exploit this, [21] makes use of two main ideas, (a) the effective optimal bosonic basis representation (OBB) and (b) the implementation of an oscillator shift:

- (a) Originally introduced by [81], the OBB representation describes a basis transformation V of the original local harmonic oscillator basis $|n_k\rangle$ onto a smaller, effective basis $|\tilde{n}_k\rangle$ on each site k ,

$$|\tilde{n}_k\rangle = \sum_{n_k=0}^{d_k-1} V_{\tilde{n}_k, n_k} |n_k\rangle \quad (\tilde{n}_k = 0, \dots, d_{opt} - 1), \quad (3.54)$$

with d_k and d_{opt} denoting the size of the original and effective basis, respectively. Including V into the A -tensors on each bosonic site, the structure of $A^{[n_k]}$ is now given by

$$A_{l_k, r_k}^{[n_k]} = \sum_{\tilde{n}_k=0}^{d_{opt}-1} \tilde{A}_{l_k, r_k}^{[\tilde{n}_k]} V_{\tilde{n}_k, n_k}, \quad (3.55)$$

where $\tilde{A}^{[\tilde{n}_k]}$ links the effective bosonic basis to the left and right part of the chain, while V maps the original to the effective local basis. The previously presented local

optimization procedure thus splits into two steps: at first, V is updated and in this process the optimal effective local basis set $|\tilde{n}_k\rangle$ is determined. Then we optimize $\tilde{A}^{[\tilde{n}_k]}$ using the new local basis states and move to the next site. The main advantage of the OBB representation is that it allows us to significantly increase the size of the local basis sets from $d_k \approx 25$ to $d_k \leq 10^4$.

- (b) The local bosonic state space can further be expanded by incorporating a displacement of the oscillator modes when constructing the OBB. Following [20], the oscillator coordinates $\hat{x}_k = (\hat{b}_k + \hat{b}_k^\dagger)$ are shifted by their equilibrium value $\langle \hat{x}_k \rangle$, such that the OBB captures the quantum fluctuations near the shifted coordinate $\hat{x}'_k = \hat{x}_k - \langle \hat{x}_k \rangle$. This is achieved by formulating the shift δ_k as an unitary transformation

$$\hat{U}(\delta_k) = e^{\frac{\delta_k}{2}(\hat{b}_k^\dagger - \hat{b}_k)}, \quad (3.56)$$

acting on the local bosonic operators \hat{b}_k^\dagger and \hat{b}_k as

$$\hat{b}'_k = \hat{U}^\dagger(\delta_k)\hat{b}_k\hat{U}(\delta_k) = \hat{b}_k + \frac{\delta_k}{\sqrt{2}}, \quad (3.57)$$

$$\hat{b}'_k{}^\dagger = \hat{U}^\dagger(\delta_k)\hat{b}_k^\dagger\hat{U}(\delta_k) = \hat{b}_k^\dagger + \frac{\delta_k}{\sqrt{2}}. \quad (3.58)$$

By the application of $\hat{U}(\delta_k)$ on $\hat{b}_k^\dagger, \hat{b}_k$ we automatically shift \hat{x}_k by δ_k ,

$$\hat{x}'_k = \frac{1}{\sqrt{2}}(\hat{b}'_k + \hat{b}'_k{}^\dagger) = \hat{x}_k + \delta_k. \quad (3.59)$$

Therefore Guo et al. proposed to calculate $\langle \hat{x}_k \rangle$ after processing the local optimization procedure from (a). Then by setting $\delta_k = \langle \hat{x}_k \rangle$ and replacing $\hat{b}_k^\dagger, \hat{b}_k$ by their displaced version $\hat{b}'_k{}^\dagger, \hat{b}'_k$, the shift can be included exactly on the Hamiltonian level, $\hat{H}'_c(\hat{b}'_k{}^\dagger, \hat{b}'_k) = \hat{H}_c(\hat{b}_k^\dagger, \hat{b}_k)$. Afterwards, the optimization of the current site is repeated in the shifted local bosonic basis until $\langle \hat{x}_k \rangle$ converges, before moving to the next site.

The implementation of an OBB with shifted oscillator modes allows to simulate an effective local basis that would require a local dimension of $d_k^{eff} \approx 10^{10}$ in the unshifted basis, while the actual shifted basis can be kept small, $d_k = 10^2$. In addition, since the variational procedure determines the optimal shift δ_k for each site of the Wilson chain individually, the exponential growth of $\langle \hat{x}_k \rangle \propto \Lambda^k$ with increasing iteration k poses no further problem for the method.

Note that with the introduction of the OBB a second adjustable dimension d_{opt} besides the bond dimension D exists. In this work both are chosen in the spirit of [21], i.e. they are chosen large enough to keep all singular values larger than 10^{-5} .

3.3.3 One-site vs. two-site optimization

Above, we referred to VMPS as a one-site method indicating that during each step only one site is optimized while all others are kept constant. Alternatively, we can implement VMPS as a two-site algorithm, where to two A -tensors of neighboring sites are updated simultaneously. This version is mathematically equivalent to the original formulation of (finite) DMRG, where local updates are always performed on a two-site block [22].

For a bosonic model, the one-site optimization is often the preferred choice though converging generally slower. Since the Hilbert space dimension of the eigenvalue problem scales

only as $D^2 d_k$ for the one-site update compared to $D^2 d_k d_{k+1}$ in case of a two-site optimization, there is a significant difference in numerical cost for large d_k .

On the other hand, using one-site optimization has also a downside. Opposed to two-site VMPS, an implementation of a dynamic truncation procedure gets more complicated (nevertheless possible [22]). Usually, the initial choice fixes the bond dimension D throughout the calculation. This is problematic especially when symmetries are incorporated. Applying one-site VMPS causes the symmetry sectors in the A -tensors at each site to remain fixed, not allowing the state to expand into new sectors during the calculations, if required. Obviously, this leads to systematic errors in the determination of the ground state. Therefore we used a two-site optimization of an MPS in OBB representation (cf. Eq. (3.55)), which is employed in all calculations of the $U(1)$ -symmetric two-channel spin-boson model in Chap. 5. For details see A.1.

3.3.4 Energy-level flow diagrams

When VMPS is applied to a Wilson chain Hamiltonian, it is possible to generate the counterpart to the NRG energy-level flow diagram, discussed in Sec. 3.2.5. To this end, we calculate the eigenvalues E_k of the left block Hamiltonian \hat{H}_l in each iteration k when sweeping from the left to the right end of the Wilson chain. Multiplied with the correct rescaling factor Λ^{k-1} , the spectrum E_k corresponds to the rescaled eigenspectrum E_N determined in an NRG step. Analogously to its counterparts, the VMPS flow diagram contains information

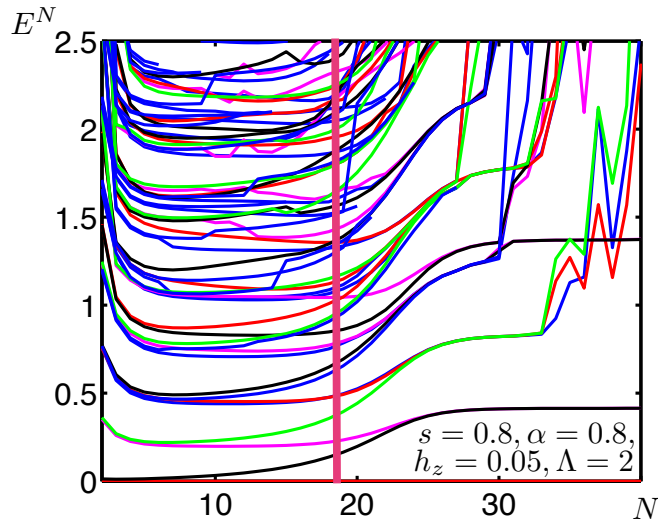


Figure 3.10: VMPS energy-level flow diagram of $U(1)$ symmetric two-channel spin-boson model. The behavior shows a similar transition from a localized to a delocalized fixed point as the NRG flow-diagram in Fig. 3.7. Due to the variational ground state optimization the lines corresponding to higher energy states display a less smooth flow than their counterparts in the NRG flow. In addition, the transition to the delocalized fixed point occurs at earlier iterations for the VMPS case. This behavior should be expected, since information of the complete chain is included in each VMPS optimization step, while the NRG spectrum only “knows” about prior iterations at higher energies.

about the fixed points of the impurity model. Comparing the flow diagrams of the spin-boson model in Fig. 3.10, the characteristics of the delocalized and the localized phase are clearly visible in the ground-state degeneracy. However, due to the variational procedure focusing on the ground state of the system only, the energy flow is less smooth than in NRG

(especially when using a shifted bosonic basis). Note that the quality of the VMPS energy flow diagrams can drastically be improved by the incorporating symmetries of the model.

3.3.5 Time-dependent VMPS

The analysis of the dynamic and thermodynamic properties of quantum systems is a central topic of modern solid state physics, which also influenced the development of the DMRG formalism. At first, DMRG was only able to treat static systems only, but the method has quickly been extended to calculate real-time dynamics and thermodynamics of quantum lattice systems. While a number of different approaches to implement time-dependence into DMRG exist [82, 83, 84, 85], we focus only on adaptive time-dependent DMRG (tDMRG) implemented in the MPS framework.

Considering a time-independent Hamiltonian \hat{H} of a 1D chain containing N sites with local and nearest-neighbor interaction only, the time-evolution of the state $|\psi(t=0)\rangle$ up to some time t is governed by the time-evolution operator,

$$\hat{U}(t) = e^{-i\hat{H}t}, \quad (3.60)$$

requiring the numerically challenging exponentiation of the many-body Hamiltonian \hat{H} . Instead of carrying out the direct exponentiation of \hat{H} as a whole, we first separate the Hamiltonian into a sum of bond terms \hat{h}_k acting only on sites k and $k+1$,

$$\hat{H} = \hat{H}_{even} + \hat{H}_{odd}, \quad \text{with } \hat{H}_{even} = \sum_{k=even} \hat{h}_k, \quad \hat{H}_{odd} = \sum_{k=odd} \hat{h}_k. \quad (3.61)$$

Now we apply the Suzuki-Trotter decomposition to separate \hat{H} for a small time step τ into a product of even and odd terms,

$$\hat{U}(\tau) = e^{-i\hat{H}_{even}\tau} e^{-i\hat{H}_{odd}\tau} + O(\tau^2) \quad (3.62)$$

$$= e^{-i\hat{h}_2\tau} e^{-i\hat{h}_4\tau} \dots e^{-i\hat{h}_1\tau} e^{-i\hat{h}_3\tau} \dots + O(\tau^2) \quad (3.63)$$

$$= \hat{U}_2(\tau)\hat{U}_4(\tau) \dots \hat{U}_1(\tau)\hat{U}_3(\tau) \dots + O(\tau^2), \quad (3.64)$$

where we used in the second step that all odd and even bond terms respectively commute with each other. Due to the non-commutivity of neighboring bond term, $[\hat{h}_i, \hat{h}_{i+1}] \neq 0$ a so-called *Trotter error* of order $O(\tau^2)$ is introduced, which can be reduced by using higher orders of the decomposition.

The determination of \hat{U} is drastically simplified by the Suzuki-Trotter decomposition, since the exponentiation is now carried out for each bond term \hat{h}_k individually.

Evolving $|\psi(t=0)\rangle$ one time step τ is now easily calculated. In a first sweep to the right we evolve all odd bonds, i.e. step by step we multiply the two-site operators $e^{-i\hat{h}_k\tau}$, k being odd, onto their corresponding A -tensors, $A^{[n_k]}$ and $A^{[n_{k+1}]}$, and truncate afterwards to prevent the bond dimensions to grow from D to $d_k^2 D$. Note that the application of a two-site operator has already been introduced in Sec. 3.1.3. Sweeping back to the right all even bonds are evolved in the same way concluding one time step τ as shown in Fig 3.11.

After each time step, physical observables can be calculated by evaluating the expectation values $\langle \hat{O}(t) \rangle = \langle \psi(t) | \hat{O} | \psi(t) \rangle$. The same applies to time-dependent correlation function such as $\langle \hat{O}(t) \hat{O}' \rangle = \langle \psi(t) | \hat{O} | \phi(t) \rangle$, where $|\psi(t)\rangle = e^{-i\hat{H}t} |\psi\rangle$ and $|\phi(t)\rangle = e^{-i\hat{H}t} \hat{O}' |\psi\rangle$.

The tDMRG procedure introduces two sources of error, one due to truncation of the bond dimensions in each time step and the other due to the Trotter decomposition. Usually, the first one is more problematic: since the entanglement of $|\psi(t)\rangle$ can grow linearly with increasing time t , the required bond dimension D rises exponentially thus limiting the

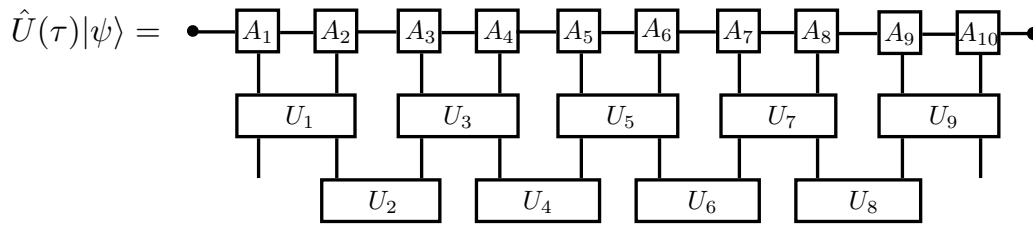


Figure 3.11: MPS diagram illustrating the application of $\hat{U}(\tau)$ to $|\psi\rangle$. In a first sweep to from left to right only the odd bonds are evolved. While sweeping back to the right all even bonds are evolved concluding one time step τ .

reachable time scale of tDMRG. Compared to truncation, the Trotter error plays a minor role for reasonably small values of τ and can be further reduced by using higher orders of the Suzzuki-Trotter decomposition. In our calculations, an algorithm based on second-order Trotter decomposition is employed,

$$e^{-i\hat{H}\tau} = e^{-i\hat{H}_{\text{odd}}\tau/2} e^{-i\hat{H}_{\text{even}}\tau} e^{-i\hat{H}_{\text{odd}}\tau/2} + O(\tau^3), \quad (3.65)$$

where the error per time step τ can be reduced by one order. This comes without additional costs if we pair steps of $\tau/2$ and evaluate observables not at every time-step.

4. Spin-boson model

A particular interesting bosonic quantum impurity model is the spin-boson model (SBM), which consists of a two-state system (e.g. a spin 1/2 impurity) coupled to a bath of non-interacting bosonic modes. In recent years, the SBM has gained a lot of attention because it is one of the simplest non-trivial models for studying the physics of competing interactions relevant in a wide range of applications. Popularized in 1987 by Leggett et al. in the context of quantum dissipation [4, 6], the SBM has been applied to a wide range of physical systems including the description of electron transfer processes in biomolecules [7], entanglement of qubits with the environment [8, 9], trapped ions [86] and cold atom quantum dots [10, 11], to name but a few.

The SBM hosts an impurity quantum phase transition at zero temperature, that has been subject of controversial discussion in the community for many years. Quantum-to-classical correspondence predicts that the quantum phase transition of the SBM corresponds to the classical transition of a 1D-Ising chain with long-ranged interactions. The first numerical studies of the QPT based on NRG obtained results that suggested a failure of quantum-to-classical correspondence for the SBM [16, 17, 18]. However, subsequent studies reasoned that the two limitations of bosonic NRG - namely the bosonic truncation and the mass-flow error - perturb calculations of critical properties, and thus doubted the former conclusions on the breakdown of quantum-to-classical correspondence [87, 88, 89]. Indeed more recent works quantum Monte Carlo, exact diagonalization and VMPS confirm its validity for the SBM [19, 20, 21].

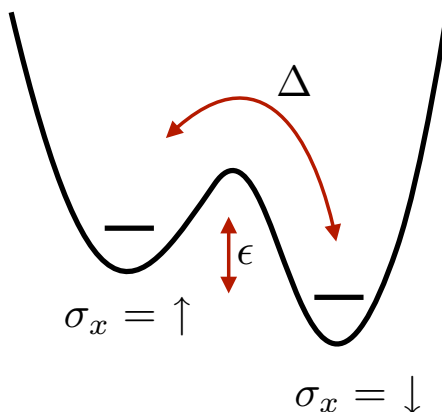


Figure 4.1: Schematic display of the spin-boson system with the quantum tunneling coefficient Δ and the bias ϵ .

In this chapter we explore the static and dynamic physical properties of the spin-boson model at zero temperature using the VMPS method introduced previously. Starting with the ground-state phases and the QPT, we present results for additional critical exponents. Then

we present results of the non-equilibrium dynamic of the SBM in the ohmic and sub-ohmic regime obtained by tDMRG.

4.1 Static properties

We have already encountered the spin-boson Hamiltonian briefly in the discussion of bosonic NRG in Sec. 3.2.1. The impurity consists of a single spin 1/2 represented by the Pauli matrices $\hat{\sigma}_{x,z}$, which is coupled linearly by λ_i to a bath of harmonic oscillators with creation operators a_i and frequencies ω_i :

$$\hat{H} = \underbrace{\frac{\epsilon}{2}\hat{\sigma}_x - \frac{\Delta}{2}\hat{\sigma}_z}_{\hat{H}_{imp}} + \underbrace{\sum_i \omega_i \hat{a}_i^\dagger \hat{a}_i}_{\hat{H}_{bath}} + \underbrace{\frac{\hat{\sigma}_x}{2} \sum_i \lambda_i (\hat{a}_i + \hat{a}_i^\dagger)}_{\hat{H}_{coupling}}, \quad (4.1)$$

where ϵ is an additional bias in coupling direction and Δ gives the bare tunneling amplitude between the two spin eigenstates $|+\rangle$ and $|-\rangle$ of $\hat{\sigma}_x$. The properties of coupling and bath are completely characterized by the bath spectral function, which is generally defined by the density of states of the bath $\rho(\omega)$ and the coupling $\lambda(\omega)$,

$$J(\omega) = \pi \sum_i \lambda_i^2 \delta(\omega - \omega_i). \quad (4.2)$$

For the description of the asymptotic low-temperature behavior of the model only the low-energy spectrum of the bath plays a role. Since we are particularly interested in the zero-temperature physics of the model only the low-energy spectrum of the bath needs to be taken into account. Hence, we employ the standard parametrization of the spectral function of power law form and only retain frequencies up to a critical frequency ω_c .

$$J(\omega) = 2\pi\alpha\omega_c^{1-s}\omega^s, \quad 0 < \omega < \omega_c, \quad s > 0. \quad (4.3)$$

where the dissipation strength of the bath is characterized by the dimensionless constant α . s determines the density of low-energy states and takes up the role of an effective dimension, which we comment on in detail in the discussion of the critical phenomena. One distinguishes between ohmic ($s = 1$), sub-ohmic ($s < 1$) and super-ohmic ($s > 1$) dissipation.

To apply the aforementioned VMPS procedure to the SBM, we discretize Eq. (4.1) and map it onto a semi-infinite Wilson chain (see Sec. 3.2.2 and 3.2.3 for details),

$$\hat{H}_{chain} = \hat{H}_{imp} + \sqrt{\frac{\eta_0}{\pi}} \frac{\hat{\sigma}_x}{2} (\hat{b}_0 + \hat{b}_0^\dagger) + \sum_{n=0}^{\infty} [\epsilon_n \hat{b}_n^\dagger \hat{b}_n + t_n (\hat{b}_n^\dagger \hat{b}_{n+1} + \hat{b}_{n+1}^\dagger \hat{b}_n)]. \quad (4.4)$$

All calculations in this section are carried out employing the VMPS procedure including an displaced optimal bosonic basis. If not stated otherwise, we use the discretization parameter $\Lambda = 2$, bond dimensions $D = 40$, $d_{opt} = 16$ and chain-length $N = 50$ in all calculations. Note that for $\epsilon = 0$ the Wilson chain Hamiltonian in Eq. (4.4) commutes with the parity operator,

$$\hat{P} = \sigma_x e^{i\pi\hat{N}}, \quad (4.5)$$

where $\hat{N} = \sum_i \hat{b}_i^\dagger \hat{b}_i$ counts the total number of bosons on the Wilson chain. The incorporation of parity symmetry into the VMPS procedure is especially crucial for the VMPS energy-flow diagrams. These are very sensitive to numerical perturbations on early sites of the Wilson chain, which can lead to artificial symmetry breaking. Since a VMPS code with explicit parity symmetry guarantees the correct degeneracy corresponding to the different ground states of the SBM, all VMPS flow diagrams in this chapter are generated in that manner (see next section).

4.1.1 Ground state phases

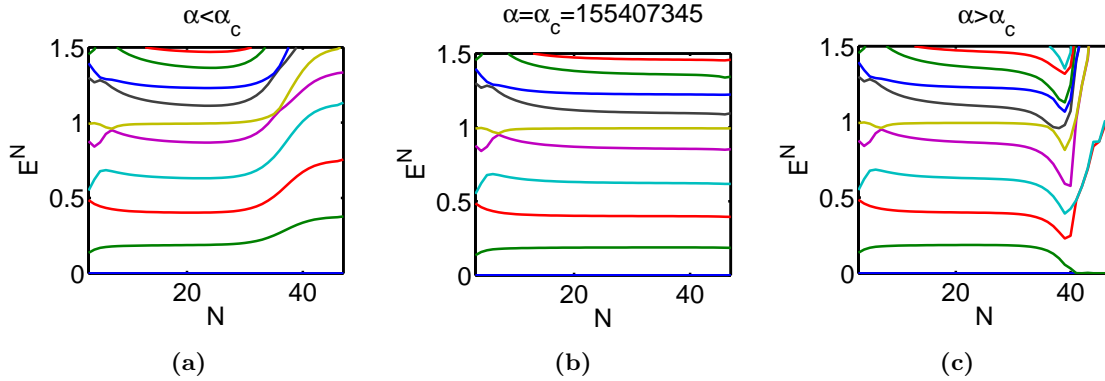


Figure 4.2: VMPS energy-flow diagrams for the sub-ohmic SBM with $s = 0.6$. (a) and (c) show the flow from the critical towards the delocalized and localized fixed point, respectively. In (b) the system is located directly at the phase boundary displaying a completely smooth energy-flow, signal of a critical fixed point.

At zero temperature and zero bias ϵ , the interplay between dissipation and spin precession, driven by the coupling α and the tunneling coefficient Δ respectively, determines the physical properties of the SBM. The model exhibits two distinct types of ground states:

1. A strongly coupled, localized ground state, where the dissipation is strong enough to localize the spin in the direction of the bath coupling resulting in a finite magnetization, $\langle \sigma_x \rangle \neq 0$, corresponding to a spontaneous symmetry breaking. Moreover, the ground state in the localized phase is two-fold degenerate.
2. A weakly coupled, delocalized ground state, where the bath coupling does not suffice to localize the impurity spin. Thus the magnetization of the ground state in the coupling direction remains zero, $\langle \sigma_x \rangle = 0$, and no degeneracy is present.

Both types of ground states correspond to two stable fixed points in the RG language, which can be identified in the VMPS flow diagrams, as illustrated for $s = 0.6$ in Fig. 4.2. Panel (a) displays the characteristic energy-flow of a delocalized fixed point with non-degenerate ground state at late iterations, while in (c) the system flows to a localized fixed point with a two-fold degeneracy of the ground state energy level. The quantum phase transition separating the two stable fixed points corresponds to an additional fixed point in the sub-ohmic regime, illustrated in Fig. 4.2(b) and is discussed in the next section. Which fixed point is reached depends on the interplay of dissipation strength α , tunneling coefficient Δ and the power law exponent of the bosonic bath s . This is illustrated in the phase diagram in Fig. 4.3(a), where the critical coupling $\alpha_c(\Delta)$ is plotted for different values of Δ denoting the location of the phase transition between localized and delocalized regime. Since the bath exponent s determines the bosonic density of states at low energies (it decreases if s increases), s directly influences the dissipation strength $\alpha > \alpha_c$ necessary to localize the spin. Hence, the critical coupling α_c rises with increasing s , reaching its maximum value at $s = 1$ in the ohmic regime. Similarly, a larger tunneling coefficient drives the delocalization of the spin and thus increases α_c as well. In Fig. 4.3(b) the Δ -dependence of the critical coupling is displayed. For small Δ , α_c shows a power law behavior, $\alpha_c \propto \Delta^k$, where $k = 1 - s$. Note that the phase transition is no longer present in the super-ohmic regime, since the system always delocalizes.

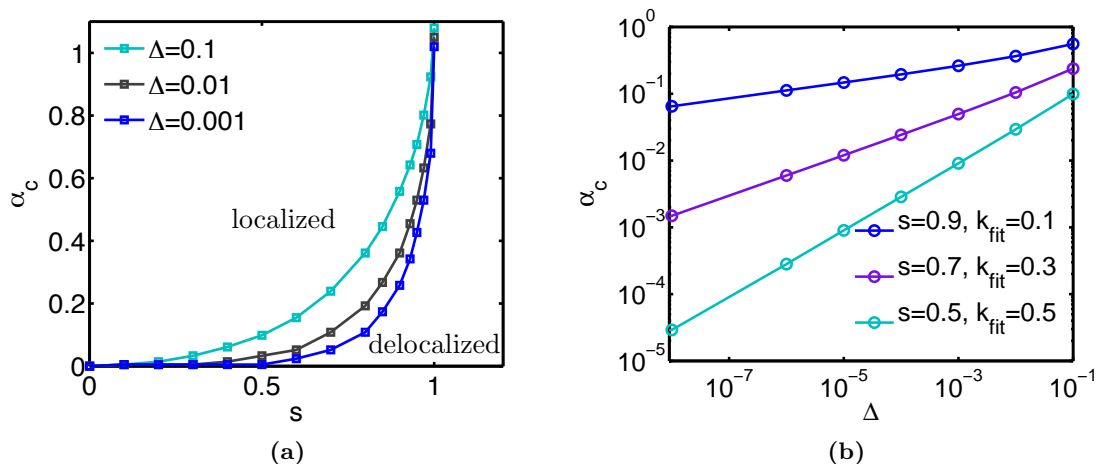


Figure 4.3: The phase diagram of the SBM in (a) shows a transition between a localized ($\alpha > \alpha_c$) and a delocalized ($\alpha < \alpha_c$) regime for various values of the tunneling coefficient Δ . In (b) the Δ dependence of the critical coupling α_c is displayed for different values of s .

Determining the critical coupling

Different ways exist to determine the critical coupling α_c numerically. One approach typically used in the Wilson chain setup of the SBM relies on energy-flow diagrams. For sub-ohmic dissipation, the flow diagrams show a crossover from the quantum critical fixed point to the localized ($\alpha > \alpha_c$) or delocalized fixed point ($\alpha < \alpha_c$) as illustrated in Fig. 4.2. The crossover can be characterized by a low-energy scale $T^* = c\Lambda^{-N^*}$, where N^* defines the iteration where the crossover becomes apparent and c is a constant prefactor. The critical coupling can be determined by non-linearly fitting the numerical data for $T^*(\alpha)$, as described in [49].

For our calculations we employed a different scheme, that is based on the characteristic behavior of the bosonic occupation numbers $\langle n_x \rangle$ in the ground state on the Wilson chain. As depicted in Fig. 4.4, we observe an increase of the numbers of bosons on each site towards the end of the chain in the localized phase, while the occupation numbers steadily decay going to higher iterations in the delocalized regime. The critical point is characterized by an almost constant occupation throughout the chain followed by a sharp decay at the end. We have verified that this characteristic feature can be used to numerically determine the critical coupling α_c with equivalent accuracy compared to the first approach. We have thus adopted this approach throughout for determining the α -values involved in the results described below.

As noted in [80], accessing critical properties requires a resolution down to the low-energy scale $T^* \propto |\alpha - \alpha_c|^\nu$, where ν is the critical exponent of the correlation length. The energy scale accessible by the bosonic Wilson chain of length N scales exponentially as Λ^{-N} .

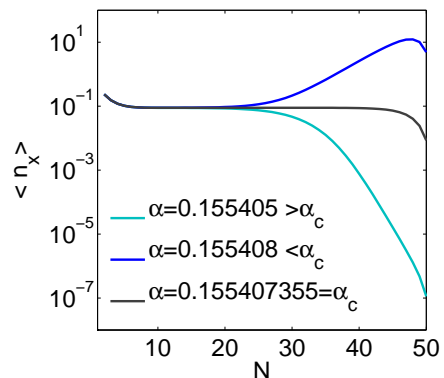


Figure 4.4: Characteristic behavior of bosonic occupation numbers $\langle n_x \rangle$ on the Wilson chain for the sub-ohmic SBM with $s = 0.6$ in the localized (blue), delocalized (light blue) phase and at the QPT (black).

Therefore ν and N essentially determine how accurately α_c can be determined numerically. In other words, if we want to calculate α_c with an accuracy of 10^{-a} , the Wilson chain requires a minimum length of

$$N \propto a\nu \frac{\ln(10)}{\ln \Lambda}. \quad (4.6)$$

4.1.2 Quantum phase transition

In the regime of $0 < s \leq 1$, the spin-boson model displays a quantum phase transition at zero temperature between a localized and a delocalized phase, which has gained much attention in recent years [16, 17, 19, 20, 21]. Quantum-to-classical correspondence predicts that the QPT of the SBM belongs to the same universality class as the classical transition of a 1D Ising chain with long-ranged interaction,

$$\hat{H}_{Ising} = - \sum_{\langle ij \rangle} J_{ij} \hat{S}_i^x \hat{S}_j^x + \hat{H}_{SR}, \quad (4.7)$$

with the interaction term $J_{ij} = J/|i - j|^{1+s}$, where \hat{H}_{SR} contains additional generic short-ranged interactions arising from the transverse field, which is considered irrelevant for the critical behavior of the model [90, 91]. The 1D Ising chain exhibits a phase transition for $0 < s \leq 1$. In this context, s acts as an effective dimension, since it determines the power law of the spectra and correlations [17]. It has been shown that the upper and lower critical dimensions of the model are located at $s = 1/2$ and $s = 1$, respectively [91].

As a consequence of the quantum-to-classical mapping, the critical phenomena of the SBM and of the 1D Ising chain should be equivalent. This results in the following predictions for the critical exponents of the SBM, which are defined in table 4.1:

- For $s = 1$, the QPT is of Kosterlitz-Thouless type, classified by an exponentially diverging correlation length and the absence of an additional critical fixed point. A Kosterlitz-Thouless phase transition is typical for a system reaching its lower critical dimension.
- In the regime $1/2 < s < 1$ the effective dimension of the system lies between the upper and lower critical dimension, indicating non-trivial critical behavior. Critical exponents can be related to the effective dimension s via perturbative RG calculations, which lead to $x = \gamma = s$. Moreover the exponents obey so-called hyperscaling relations,

$$\delta = \frac{1+x}{1-x} = \frac{1+s}{1-s}, \quad 2\beta = \nu(1-x) = \nu(1-s). \quad (4.8)$$

- For $0 < s < 1/2$, the effective dimension of the model exceeds the upper critical dimension indicating mean-field behavior,

$$\beta = \frac{1}{2}, \quad \delta = 3, \quad \nu = \frac{1}{s}, \quad \gamma = 1, \quad x = \frac{1}{2}. \quad (4.9)$$

The first numerical results for the critical properties of the SBM were obtained in 2003 by Bulla et al. [16] using bosonic NRG. The study confirmed the Kosterlitz-Thouless transition for $s = 1$ and the hyperscaling relations in the regime $1/2 < s < 1$ but, interestingly, it did not agree with the predictions of quantum-to-classical correspondence for $0 < s < 1/2$. Instead of finding the predicted mean-field behavior, the critical exponents extracted with

physical Quantity	Definition	Exponent	Condition
Local magnetization	$\langle \sigma_x \rangle \propto \alpha - \alpha_c ^{-\beta}$	β	$ \alpha - \alpha_c \rightarrow 0, \epsilon = 0, T = 0$
Local susceptibility	$\chi \propto \alpha - \alpha_c ^{-\gamma}$	γ	$ \alpha - \alpha_c \rightarrow 0, \epsilon = 0, T = 0$
Local magnetization	$\langle \sigma_x \rangle \propto \epsilon ^{-1/\delta}$	δ	$\alpha = \alpha_c, \epsilon \rightarrow 0, T = 0$
Correlation length	$\xi \propto \alpha - \alpha_c ^{-\nu}$	ν	$ \alpha - \alpha_c \rightarrow 0, \epsilon = 0, T = 0$
Local susceptibility	$\chi \propto T^{-x}$	x	$\alpha = \alpha_c, \epsilon = 0, T \rightarrow 0$

Table 4.1: Critical exponents of the spin-boson model where $\langle \sigma_x \rangle$ is the impurity magnetization, α_c the critical coupling, ϵ a bias of the impurity spin in coupling direction, T the temperature, ξ the correlation length and χ the susceptibility of the impurity.

bosonic NRG follow the hyperscaling relations in Eq. (4.8) across the entire sub-ohmic regime, $0 < s < 1$. These results were confirmed in subsequent NRG based works on the SBM and the related Bose-Fermi Kondo model [17, 18], hence it was concluded that quantum-to-classical correspondence would break down for sub-ohmic dissipation $0 < s < 1/2$. This was a strong statement, since the failure of quantum-to-classical correspondence would be accompanied by implications not only for dissipative bosonic systems but also for the Kondo lattice [92, 93]. Thus, the topic attracted more attention, leading to further studies based on different numerical approaches (quantum Monte Carlo [19], exact diagonalization [20] and VMPS [21]). All of these contradicted the NRG results by finding mean-field exponents for $0 < s < 1/2$. Thus the validity of quantum-to-classical correspondence for the spin-boson model can at present be regarded as well-established (although some still advocate its failure [94]). The discrepancies of the NRG results compared to other methods connect to the two limitations of bosonic NRG, the truncation error and the massflow error [87, 89].

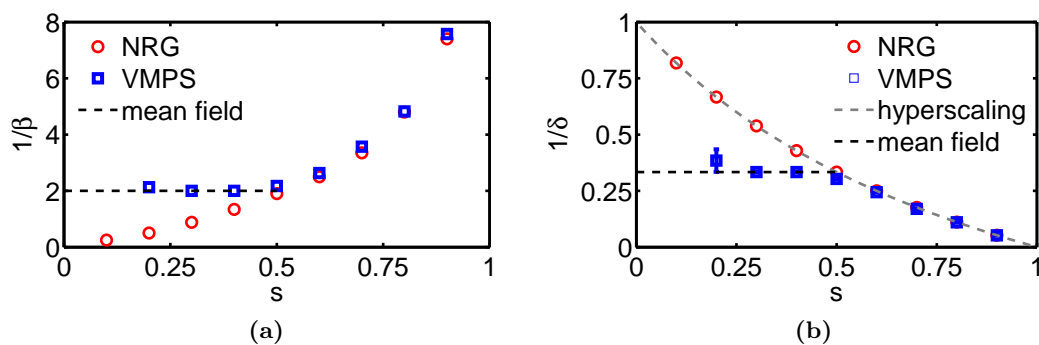


Figure 4.5: Critical exponents (a) β and (b) δ for different values of s calculated with VMPS (blue squares) and NRG (red dots). Only the VMPS calculations in (a) and (b) agree with the mean-field predictions (dashed black lines) for $0 < s < 1/2$, while NRG leads to different results following hyperscaling in (b). For $1/2 < s < 1$ both methods agree reasonably well with δ satisfying the hyperscaling relation in Eq. (4.8). Figure is adapted from [21].

In [21], the truncation effects of the local bosonic state spaces on the results of the critical exponents δ and β were illustrated very convincingly using the same VMPS procedure as in this work. While calculations using with a unshifted local bosonic basis yielded results for δ that obey the hyperscaling relation $\delta = (1 + s)/(1 - s)$ for $0 < s < 1/2$, the mean-field value $\delta = 1/2$ was reached when employing a displaced OBB procedure according to Sec. 3.3.2. Similarly, $\beta = 1/2$ was found with the optimized bosonic basis. Fig. 4.5 displays the dependency of δ and β with respect to s as displayed in [21]. We reproduced these results in reasonable calculation time using VMPS.

4.1.3 Subsequent results for critical exponents

While the results for the critical exponents β and δ already have been presented in [21], the VMPS procedure further allows us to determine the correlation length exponent ν as well as the temperature exponent x .

As noted previously, the correlation length exponent ν determines how the low-energy scale T^* , which describes the energy resolution on which quantum critical phenomena are observable, vanishes near the quantum critical point,

$$T^* \propto |\alpha - \alpha_c|^\nu. \quad (4.10)$$

Within the VMPS framework, the low-energy scale T^* can be read off energy-flow diagrams, as indicated in Fig. 4.2. T^* relates to the Wilson chain site N^* , where the transition of the flow from a critical to a localized/delocalized fixed point is observed, as $T^* \sim \Lambda^{-N^*}$. In general, T^* vanishes with the same exponent ν when approaching the QPT from the delocalized or localized phase. In our calculations, we started at the localized fixed point and defined N^* as the specific Wilson chain site where the energy of the first excited states decreases below $\Delta E_{01} \equiv (E_1 - E_0) \lesssim 0.05$ (in rescaled units).

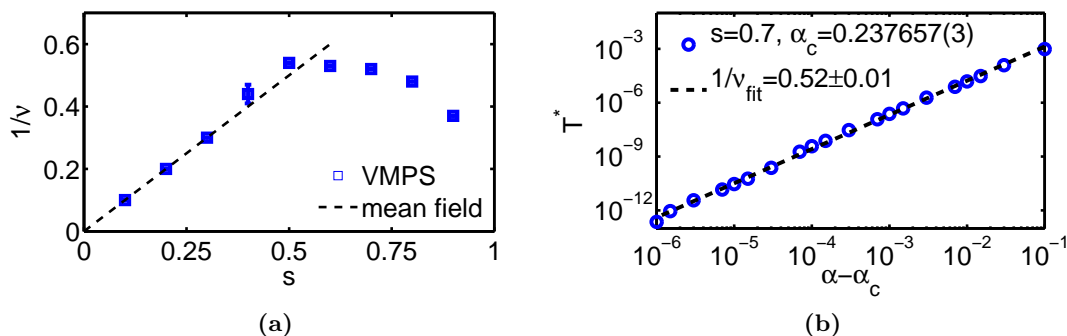


Figure 4.6: (a) Critical exponent ν of the spin-boson model for different values of s together with mean-field prediction of Eq. (4.9). (b) Vanishing of T^* close to the critical point for $s = 0.7$. The dashed black line indicates the numerical fit for the extracted exponent ν .

In Fig. 4.6(b) the vanishing of T^* close to the QPT is shown for $s = 0.7$. We clearly see that T^* decreases in a power law fashion, which allows us to extract the exponent ν via a non-linear fit. The resulting values of ν for different s are illustrated in Fig. 4.6(a), while the corresponding fitting can be found in Fig. B.1 of the appendix. ν diverges as expected for both $s \rightarrow 1$ (Kosterlitz-Thouless transition) and $s \rightarrow 0$ (completely localized system). Moreover, it follows the expected mean-field relation $1/\nu \propto s$ in the regime of $0 < s < 1/2$, with small deviations close to $s = 1/2$. At this point we expect logarithmic corrections to the leading power law, because the system is at its upper critical dimension. Since ν is neither corrupted by the bosonic truncation error nor the massflow error, we can compare our results with NRG studies [17] and find agreement with these over the complete interval of s .

Although we restrict our calculations to zero temperature only, VMPS allows to determine the critical exponent x which defines the temperature scaling of the susceptibility χ at the critical point. This can be achieved by studying the finite-size scaling of the impurity magnetization $m = |\langle \sigma_x \rangle|$ in coupling direction. In general, the system size L relates to the

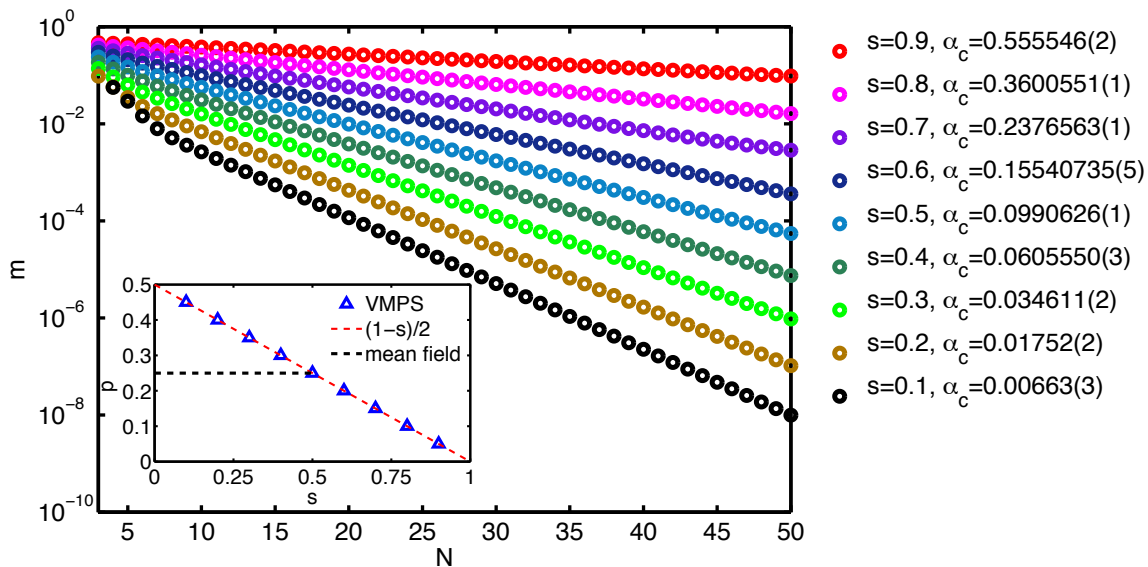


Figure 4.7: Finite-size scaling of the magnetization m at the QPT for various values of s . The inset displays dependence of the exponent p defining the exponential decay of m on the value of s (blue triangles). The dashed lines indicate the values of p expected for mean-field (black) behavior, $x = 1/2$, and the RG predictions valid in the presence of hyperscaling, $x = s$.

discretization parameter of the Wilson chain Λ and its length N as

$$\frac{1}{L} \propto \frac{1}{\Lambda^N}. \quad (4.11)$$

Assuming that the magnetization m approaches a well defined value m_0 in the limit $L \rightarrow \infty$, we expect corrections to m_0 for finite systems exponentially scaling with L ,

$$\begin{aligned} m &= m_0 + a \frac{1}{L^p} \\ &= m_0 + a(\Lambda^{-N})^p \\ &= m_0 + ae^{-\ln(\Lambda)pN}. \end{aligned} \quad (4.12)$$

According to [95], the magnetization of a gapped system scales as $m \propto \tilde{\Delta}^{(1-x)/2}$ close to a critical fixed point ($m_0 = 0$), with $\tilde{\Delta}$ being the finite energy gap. Since the lower energy cut-off Λ^{-N} acts as an effective energy gap [96], the exponent p of the finite-size corrections relates to the temperature exponent x at the critical point such as,

$$m \propto (\Lambda^{-N})^p = (\Lambda^{-N})^{(1-x)/2}, \quad (4.13)$$

which results in $2p = 1 - x$. Thus by studying the finite-size scaling of m at the phase boundary of the QPT and extracting the exponent p , we are able to determine the critical exponent x . Note that this relation is only valid in the presence of hyperscaling relations, i.e. below the upper critical dimension of the system (here $s = 1/2$).

In Fig. 4.7 the finite-size scaling of m is displayed for various values of s , while the extracted exponents p are illustrated in the inset. The inset suggests that $x = s$ for the complete dissipation spectrum of the sub-ohmic SBM, $0 < s < 1$. This result agrees with the perturbative RG predictions for $1/2 < s < 1$; however, it disagrees with expected mean-field result $x = 1/2$ in the regime $0 < s < 1/2$. The reason for this disagreement is as follows: For these values of s the system remains above the upper critical dimension and x is distorted by

the so-called massflow error that is inherent in the iterative finite-size scaling [88]. Similar to the iterative NRG procedure, the renormalization of the system is only taken partially into account at each iteration (lower energy scales to the left are disregarded). Thus at any step there is a missing parameter shift set by the current energy scale of the iteration. This indicates that the location of the critical coupling depends strongly on the minimal energy scale reached, i.e. on $T^* \propto \Lambda^{-N}$ where N is the length of the Wilson chain. By only including $M < N$ iterations, the finite-size scaling analysis in effect moves the system away from criticality, causing the deviation of x from the mean-field predictions.

As already discussed, the critical exponents follow the hyperscaling relations in Eq. (4.8) in the regime $1/2 < s < 1$. While the validity of the first hyperscaling relation for δ has already been proven in [21], the access to ν and x enables us to also check the validity of the second hyperscaling relation,

$$x = (1 - 2\beta/\nu). \quad (4.14)$$

Fig. 4.8 compares different results of x in the hyperscaling regime $1/2 < s < 1$. The blue squares indicate the extracted values of x from the finite size scaling, the red crosses display the results of Eq. (4.14) using β and ν collected from VMPS data and the dashed line relates to the RG prediction $x = s$. We find excellent agreement between the predicted values of x with VMPS calculations (deviations smaller than 2%). Although this result is to be expected, it proves the accuracy of the employed VMPS method. Moreover, it serves as a benchmark calculation illustrating that ν and x are accessible within VMPS. This is crucial when discussing the validity of our VMPS results for the critical phenomena of the two-channel spin-boson model in Chap. 5.

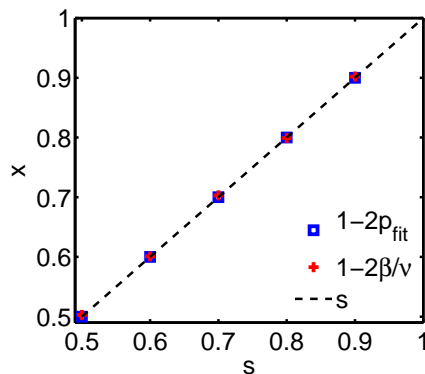


Figure 4.8: Critical exponent x calculated from finite-size scaling (blue squares) and hyperscaling (red crosses) compared with the RG prediction $x = s$.

4.2 Non-equilibrium dynamics

In the previous section the discussion focused on static properties of the spin-boson model, which have gained much attention in recent years mainly due to the controversy of the sub-ohmic quantum phase transition. Nevertheless, the model was originally introduced to study the dynamics of dissipative quantum systems [4], since the SBM is the simplest non-linear model displaying quantum coherence, friction and fluctuations of thermal and quantum nature, all essential features for the realistic description of a quantum system interacting with its environment. Particularly its applicability in quantum information, where the SBM models the interaction of a qubit with its environment, has turned the SBM to one of the most studied dissipative systems in the last decades. Despite its simplicity compared to other models, full analytical solutions of its dynamical behavior exist only in a few exceptional cases. However, various approximation methods have been developed for the different parameter regimes of the SBM, that help to gain deeper understanding of the impurity spin dynamics especially in the ohmic regime. For a detailed discussion on this extensive topic we refer to the book of U. Weiss [5].

In this section we briefly study the non-equilibrium dynamics of the SBM in the ohmic and sub-ohmic regime. For this purpose we extended the static version of our VMPS code using adaptive time-dependent DMRG as described in Sec. 3.3.5. We simulate a quantum quench by preparing the impurity spin in coupling direction by applying a strong bias field ϵ and then start the time-evolution while simultaneously setting $\epsilon = 0$. Depending on the parameter regime of the SBM, we can observe coherent oscillations or an incoherent relaxation of the impurity spin. We compare our tVMPS data for the ohmic SBM in the weak coupling regime with the non-interacting blip approximation [4, 97, 5] finding good quantitative agreement. Furthermore, we study the non-equilibrium dynamics of the sub-ohmic SBM and are able to reproduce the finding of [98], stating that a transition from coherent damped oscillations to a monotonic decay can be observed even in the localized limit of $s \rightarrow 0$.

4.2.1 tVMPS and z-averaging

When employing the bosonic tVMPS code discussed in Sec. 3.3.5, we have to consider the numerical problems arising in this procedure. First of all, since we study the relaxation of a non-equilibrium system we expect the entanglement of the time-evolved state $|\psi(t)\rangle$ to grow linearly thus blowing up the required bond dimensions of the MPS. The induced truncation error increases exponentially with time and therefore limits the accessible time to $t \sim 10^4/\omega_c$.

The bosonic nature of the SBM introduces a second issue, the truncated bosonic basis. Whenever we apply bosonic tVMPS, we have to include a sufficiently large bosonic basis on each site of the Wilson chain to ensure the time-evolution is not corrupted by truncating parts of the Hilbert space required for an accurate description of $|\psi(t)\rangle$. This problem does not arise in the delocalized regime, where a small local basis suffices to describe the low-energy excitations. We know on the other hand, that the localized phase requires a shifted basis to appropriately represent the low-energy states of the system. Since the displaced oscillator basis is not applicable in tVMPS, we can access the localized regime only close to the QPT on short time scales.

Moreover, when considering a Wilson chain with finite length N we represent a system with a continuous bath spectrum by a discretized finite size version. This yields another source of error for the time-evolution of the model known from time-dependent NRG approaches [59]. The finite system size affects the time evolution in two ways. On the one hand, the finite energy resolution limits the accuracy of the system dynamics to times $t < \Lambda^N$. This is only a minor problem, since we can usually adapt the chain to a sufficiently large length.

We found that the major restriction on the accessible time scale is rather caused by the bond truncation error. On the other hand, an accurate time-evolution relies on a continuous high energy spectrum of the bath modes, posing a serious challenge to any finite size representation using a logarithmic discretization scheme. To simulate the continuous bath spectrum we borrow a method successfully applied in NRG, Oliveira's so-called z -trick [99]. The idea is to add a shift to the discretization of the bath spectral function using an additional parameter z ,

$$\omega_n = \Lambda^{-n+z}, \quad n = 1, 2, 3, \dots, \quad z \in [0, 1), \quad (4.15)$$

where each choice of z includes different high energy states of the bosonic bath. By calculating the time-evolution separately for n_z different z -values equally spaced over the interval $[0, 1)$ and averaging the time-dependent observables, we simulate a continuous bath spectrum. In this way we reduce numerical artifacts that manifest themselves for example in unphysical oscillation as shown in Fig. 4.9(a).

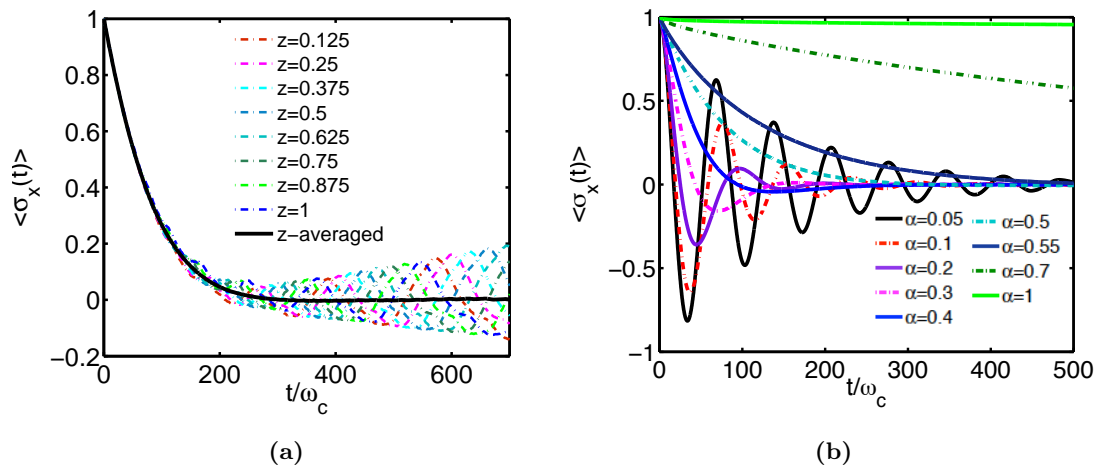


Figure 4.9: Time-evolution of the ohmic SBM starting from a fully polarized impurity spin. In (a) the z -averaging procedure is illustrated for the relaxation at the Toulouse point, $\alpha = 0.5$ with $\Delta = 0.1$. While the dotted lines, each representing the spin dynamics for one particular value of z , show unphysical oscillations caused by discretization artifacts, their average (black line) displays a smooth relaxation of the impurity spin. (b) shows the spin dynamics for various values of α in the delocalized regime with $\Delta = 0.1$. In the weak coupling regime, $0 < \alpha < 1/2$ we observe damped oscillations, while the spin decays monotonically to zero for strong coupling, $1/2 < \alpha < \alpha_c$.

To study the non-equilibrium dynamic of the SBM, we first apply a strong bias $\epsilon(t < 0) = 100$ and set the tunneling coefficient $\Delta(t < 0) = 0$ to obtain a fully polarized impurity spin as an initial state by standard VMPS calculation. Before we start the time-evolution employing tVMPS, we set $\epsilon(t = 0) = 0$ and change Δ to a finite value. For all calculations presented in this section, we chose the maximum bond dimension $D = 150$, the local dimension of $d_1 = 20$ for the first and $d_k = 5$ for the other bosonic sites, the chain length $N = 35$, $n_z = 8$ different z -values, a discretization parameter $\Lambda = 1.2$ and the time-step $\tau = 0.2$. For all calculations we carefully checked a priori that no divergence of the bosonic occupation numbers occurs on the Wilson chain.

4.2.2 Ohmic dynamics

Contrary to the SBM with sub-ohmic dissipation, the dynamical behavior of the ohmic SBM is well understood [4, 5]. The time evolution of the impurity spin in coupling direction $\langle \sigma_x(t) \rangle$ for a system with initially fully polarized spin, finite Δ and $\epsilon = 0$ strongly depends on the value of the coupling constant α . For $0 < \alpha < 1/2$ the system shows coherent oscillations that decay to zero. At the so-called Toulouse point, $\alpha = 1/2$, the characteristics of the dissipation changes drastically so that for $1/2 \leq \alpha < \alpha_c$ the spin decays monotonically to zero and oscillations are no longer present. In the localized phase, $\alpha > \alpha_c$, the magnetization $\langle \sigma_x(t) \rangle$ does not approach zero anymore for $t \rightarrow \infty$. Instead the spin localizes at a finite value.

In Fig. 4.9(b) the time-evolution of $\langle \sigma_x(t) \rangle$ is calculated with tVMPS for various values of the coupling constant α . We are able to reproduce the underdamped oscillations for $0 < \alpha < 1/2$ and the monotonic decay for $1/2 < \alpha < \alpha_c$, where $\alpha_c \approx 1.15$. However, since tVMPS is restraint to comparatively short long time scales due to the exponentially growing Hilbert space dimension, our method is not able to prove that the spin approaches a finite value in the localized phase. Nevertheless, the spin dynamics close to α_c already indicates a very slow decay that eventually saturates at a finite magnetization.

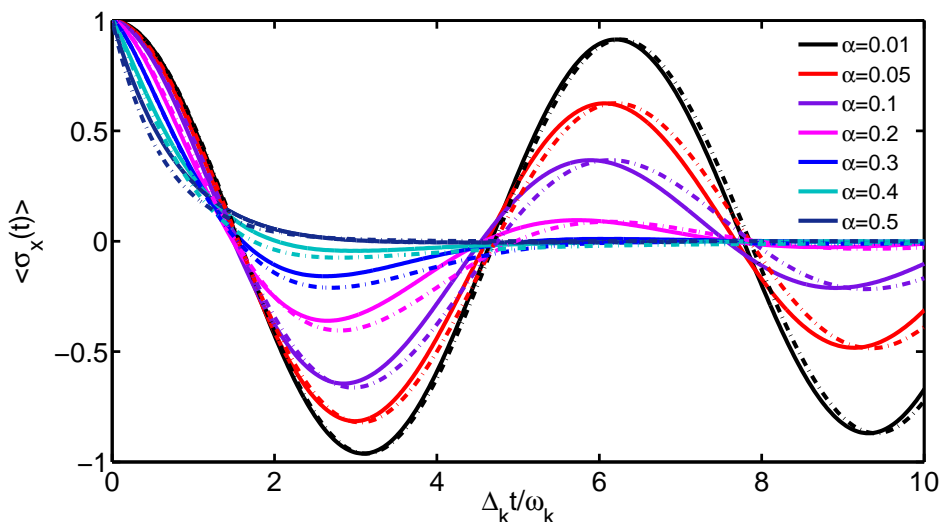


Figure 4.10: Non-equilibrium dynamics of a polarized impurity spin in the SBM for various values of α in the weak coupling regime $0 < \alpha < 0.5$ and tunneling coefficient $\Delta = 0.1$. The tVMPS results (solid lines) show good quantitative agreement with the predictions of the non-interacting blip approximation (dashed lines), calculated with Eq. (4.16).

Among various analytical methods that have been employed to study the spin dynamics in the weak coupling regime $0 < \alpha < 1/2$, the non-interacting blip approximation (NIBA) is one of the most prominent. It relies on the key assumption that the system spends much more of its time in a diagonal state of the density matrix than in an off-diagonal or 'blip' state. While this approximation leads to discrepancies in the asymptotic limit of $t \rightarrow \infty$, it is considered to work well for the unbiased SBM ($\epsilon = 0$) on short and intermediate time scales [5]. While NIBA was originally derived in a diagrammatic approach using a path-integral formalism [4], more compact derivations can be found in the literature [97]. According the NIBA formulation in [5], the time evolution of an initially polarized impurity spin is given

by

$$\langle \sigma_x(t) \rangle = \sum_{m=0}^{\infty} \frac{(-1)^m}{\Gamma[1 + (2 - 2\alpha)m]} (\Delta_{\text{eff}} t)^{(2-2\alpha)m}, \quad (4.16)$$

where Δ_{eff} is the effective tunneling coefficient defined as,

$$\Delta_{\text{eff}} = [\Gamma(1 - 2\alpha) \cos(\pi\alpha)]^{1/[2(1-\alpha)]} \Delta (\Delta/\omega_c)^{\alpha/(1-\alpha)}. \quad (4.17)$$

It can be shown, that the effective tunneling coefficient Δ_{eff} is equal to Δ for $\alpha = 0$ and equal to $\pi\Delta^2/2\omega_c$ for $\alpha = 1/2$. Thus, NIBA recovers for $\alpha \rightarrow 0$ the dynamic solution of an undamped spin-1/2 system, $\langle \sigma_x(t) \rangle = \cos(\Delta t)$. At the Toulouse point, $\alpha = 1/2$, the SBM can be mapped on a resonant level mode, which can be solved exactly [5]. In this case NIBA reproduces the exact solution,

$$\langle \sigma_x(t) \rangle = e^{-\pi\Delta^2/(\omega_c^2)} \quad (4.18)$$

describing the monotonic relaxation of the spin to zero. For short times $t\Delta_{\text{eff}} \gg 1$, the leading term of non-interacting blip approximation in Eq. (4.16) is given by

$$\langle \sigma_x(t) \rangle = 1 - \frac{(\Delta_{\text{eff}} t)^{2-2\alpha}}{\Gamma(3-2\alpha)} + O[(\Delta_{\text{eff}} t)^{4-4\alpha}]. \quad (4.19)$$

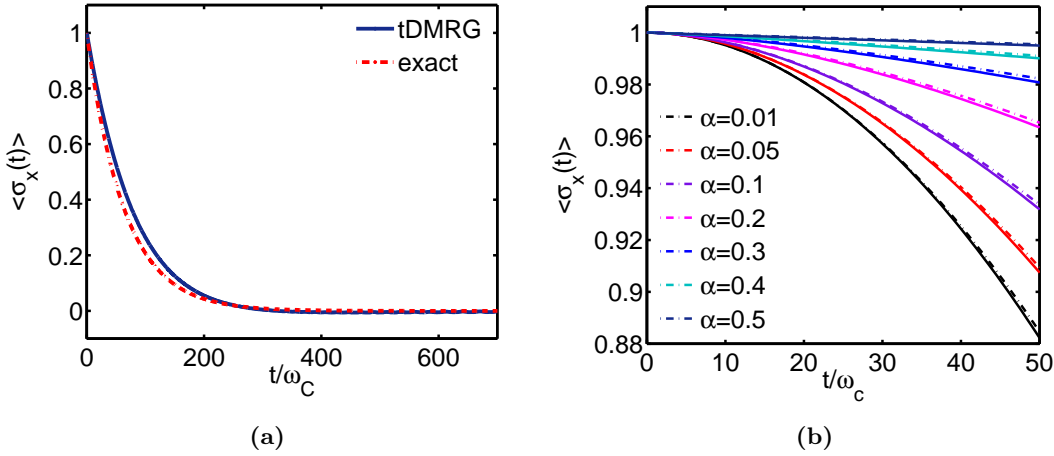


Figure 4.11: Non-equilibrium dynamics of a polarized impurity spin in the ohmic SBM (a) at the Toulouse point $\alpha = 1/2$ and (b) for short time scales in the weak damping regime $0 < \alpha < 1/2$. The solid line in (a) indicates the exact analytic result of Eq. (4.18) for $\alpha = 1/2$ and $\Delta = 0.1$, which is in agreement with the dotted line corresponding to the tVMPS calculation. The short-time analysis in (b) shows that tVMPS data (dotted lines) follow the analytic NIBA results of Eq. (4.19) almost exactly in the weak damping regime with $\Delta = 0.01$.

The NIBA predictions in the weak coupling regime $0 < \alpha < 1/2$ allow us to benchmark our tVMPS results. Fig. 4.10 displays the respective tVMPS (solid lines) and NIBA results (dashed lines) on a rescaled time-axis, where the latter are calculated with Eq. (4.16). Our method show good quantitative agreement with the NIBA predictions. On short time scales $t\Delta_{\text{eff}} \gg 1$, where NIBA is assumed to give a correct description of the time evolution via Eq. 4.19, tVMPS almost perfectly agrees with NIBA, as indicated in Fig. 4.11(b). The solid

lines illustrate the analytic solution while the dotted lines are calculated with tVMPS. A detailed analysis of the Toulouse point, $\alpha = 1/2$, is presented in Fig. 4.11(a). The tVMPS data is in accordance with the exact solution of Eq. (4.18), though we observe minor deviations that are most likely caused by finite size effects.

In conclusion, we are able to reproduce the dynamical behavior of a fully polarized impurity spin coupled to an ohmic bath with high accuracy using tVMPS. A further application to the sub-ohmic regime of the spin-boson model is presented in the next section.

4.2.3 Sub-ohmic dynamics

In contrast to the ohmic case, the dynamical properties of the SBM with sub-ohmic dissipation are only partially understood. One of the few analytic approaches studying the time-evolution of an initial non-equilibrium state suggests that there exists a transition from damped coherent oscillations at weak coupling to an incoherent decay at strong coupling, similar to the ohmic case [100]. Interestingly, the dynamics should always change from coherent to incoherent, even in the limit $s \rightarrow 0$ where the system localizes for all couplings α . Since we expect the SBM to show almost classical behavior for $s = 0$, this picture seems counter-intuitive.

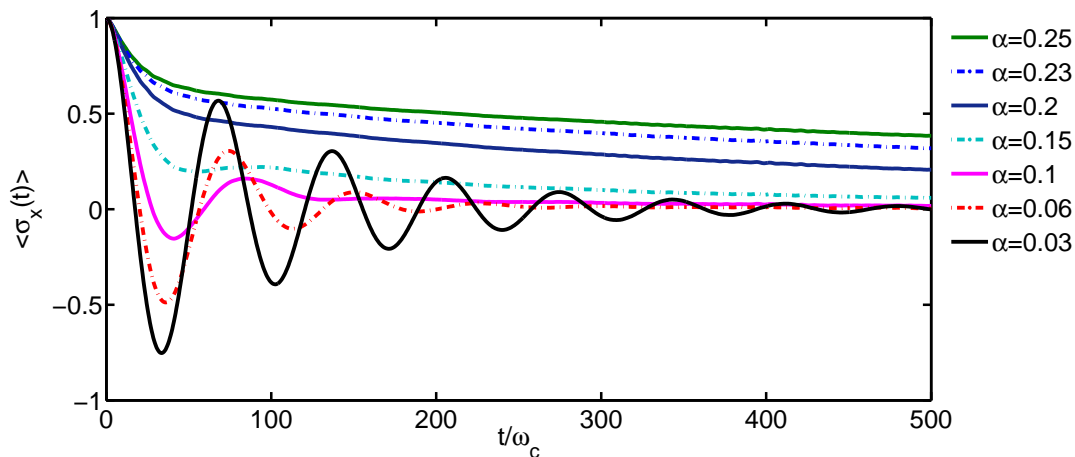


Figure 4.12: Non-equilibrium dynamics of a fully polarized spin in the sub-ohmic SBM with $s = 0.7$ and $\Delta = 0.1$ for different values of α in the delocalized regime. We observe a transition from damped coherent oscillations to an incoherent decay for $0.15 < \alpha < 0.2$.

Nevertheless, a numerical TD-NRG study confirmed the predictions by observing a transition from coherent to incoherent dynamics even in the localized phase for $s \rightarrow 0$ [98]. We are able to reproduce these findings using tVMPS applied to the non-equilibrium spin dynamics of the sub-ohmic SBM. In Fig. 4.12 the time-evolution of the impurity spin is shown for $s = 0.7$. We can clearly observe a transition from damped oscillations to an incoherent decay for intermediate couplings $0.15 < \alpha < 0.2$ in the delocalized phase. The phase boundary is approximately located at $\alpha_c \approx 0.262$. Fig. 5.6a(a) displays a similar behavior for $s = 0.5$, where a shallow oscillation can be observed even for $\alpha > \alpha_c = 0.105$ in the localized phase. The most striking feature is shown by the spin dynamics in the limit $s \rightarrow 0$ illustrated in Fig. 5.6a(b). Even though the impurity spin localizes for infinitesimally small couplings α , we can clearly see damped coherent oscillations around some finite value $\langle \sigma_x(\infty) \rangle$.

Although we are able to access the localized regime at intermediate coupling on short time scales where we do not observe a divergence of the bosonic occupation numbers on the Wilson chain, we are restricted to regions close to the QPT. For strong couplings, $\alpha \gg \alpha_c$, tVMPS breaks down due to the truncation of the local state space. Very recent works employing path-integral Monte Carlo techniques succeed to describe the sub-ohmic SBM in the strong coupling regime [101, 102]. They come to a fascinating conclusion: for $0 < s < 1/2$ the coherence in the non-equilibrium dynamics persists even for arbitrarily strong couplings α - even when the thermal equilibrium is of almost classical nature. There is no intuitive argument to explain these findings yet, indicating that further work has to be done in order to understand dissipation on the nanoscale.

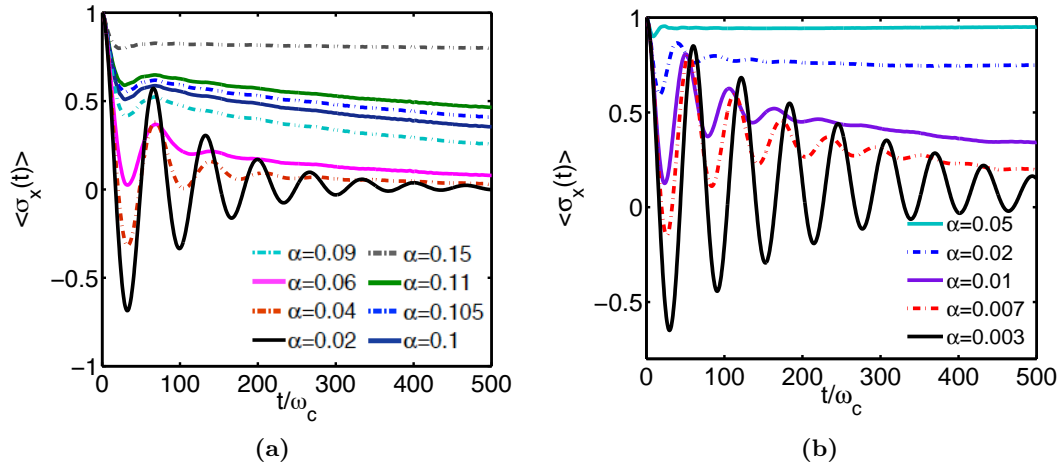


Figure 4.13: Non-equilibrium dynamics of a fully polarized spin for the sub-ohmic SBM with dissipation (a) $s = 0.5$ and (b) $s = 0$ for various values of α ($\Delta = 0.1$). In (a) the impurity spin displays strong coherent oscillations in the delocalized regime for $\alpha < \alpha_c \approx 0.105$, while the oscillations are suppressed (but still slightly visible) in the localized phase. In (b) the system localizes for any infinitesimally small coupling α . Nevertheless, we observe damped coherent oscillations around finite values of the magnetization.

5. Two-bath spin-boson model

The second bosonic quantum impurity model considered in this work is a generalized version of the spin boson model, where two independent bosonic baths couple to different components of the impurity spin. This model is particularly interesting because it hosts the phenomenon of frustration of decoherence [103, 104]: both baths compete rather than cooperate by trying to localize a different component of the impurity spin. This induces a new critical phase at intermediate coupling with highly non-trivial physical properties. The XY -symmetric version of the two-bath spin-boson model (SBM2) studied in this chapter may represent distinct noise sources arising in the context of impurities in quantum magnets [105, 106] or noisy qubits [103, 104, 107].

Recently, the first numerical study of the SBM2 based on VMPS has been carried out by [21], who extensively studied the ground state phase diagram and confirmed the existence of the critical phase in the sub-ohmic regime. However, the characterization of the two quantum phase transitions occurring in the system remained an open question. Continuing the work of [21], we present for the first time numerical results for the critical properties of the two-bath spin-boson model in the following. We start by discussing the model and its underlying abelian $U(1)$ symmetry, which turns out to be of great importance in order to obtain clean numerical results. Next, we present a short review of the ground state phase diagram and the most important properties of the critical phase, before turning to the critical phenomena. The corresponding RG results cited in this chapter are provided by Matthias Vojta [21, 96].

5.1 Model Hamiltonian

In general, the two-bath version of the spin-boson Hamiltonian has a similar structure as its one-bath counterpart,

$$\hat{H}^{SBM2} = \underbrace{-\frac{\vec{h}}{2} \cdot \vec{\sigma}}_{\hat{H}_{imp}} + \sum_{k=x,y} \left[\underbrace{\sum_i \omega_i \hat{a}_{k,i}^\dagger \hat{a}_{k,i}}_{\hat{H}_{bath}} + \underbrace{\frac{\hat{\sigma}_k}{2} \sum_i \lambda_{k,i} (\hat{a}_{k,i} + \hat{a}_{k,i}^\dagger)}_{\hat{H}_{coupling}} \right]. \quad (5.1)$$

In contrast to the standard SBM, the two-level impurity here couples both to an external field \vec{h} and to two independent bosonic baths via two different spin components, $\hat{\sigma}_x$ and $\hat{\sigma}_y$, where $\hat{\sigma}_i$ again denotes the Pauli matrix i . In this formulation the x - and y -component of the external field \vec{h} takes on the role of the bias ϵ in the standard SBM notation (c.f. Eq. (3.20), while h_z , acting perpendicular to the baths coupling acts, as an effective tunneling coefficient. For an appropriate description of the low-energy spectrum, the two spectral functions $J(\omega)_k = \pi \sum_i \lambda_{ki}^2 \delta(\omega - \omega_i)$ characterizing the bosonic baths and their interaction with the impurity are defined to be of power law form,

$$J_k(\omega) = 2\pi \alpha_k \omega_c^{1-s} \omega^s, \quad 0 < \omega < \omega_c = 1, s > 0. \quad (5.2)$$

where both coupling constants are set to be equal, $\alpha = \alpha_x = \alpha_y$, in order to study the XY -symmetric model. The reason for this choice is that we are particularly interested in the competition between the two baths, which amongst other things gives rise to an unconventional critical phase at intermediate coupling. As we will see in Sec. 5.4, small differences in the coupling coefficients lead to situations where the slightly stronger coupled bath dominates the physical behavior of the system.

In order to apply the VMPS framework to the SBM2, the model Hamiltonian in Eq. (5.1) is logarithmically discretized and then mapped on a Wilson chain following the standard protocol introduced in Secs. 3.2.2 and 3.2.3. This results in

$$\hat{H}_{chain}^{SBM2} = \hat{H}_{imp} + \sum_{k=x,y} \left[\sqrt{\frac{\eta_k}{\pi}} \hat{\sigma}_k (\hat{b}_{k,0} + \hat{b}_{k,0}^\dagger) + \sum_n (\epsilon_{k,n} \hat{b}_{k,n}^\dagger \hat{b}_{k,n} + [t_{k,n} \hat{b}_{k,n}^\dagger \hat{b}_{k,n+1} + \text{h.c.}]] \right], \quad (5.3)$$

with the on-site energies $\epsilon_{k,n}$, the hopping elements $t_{k,n}$ and the impurity-bath coupling η_k are calculated numerically.

5.1.1 Symmetries

$U(1)$ symmetry

For most of this chapter we consider the XY -symmetric model where the couplings between the impurity spin and both baths are identical, $\alpha_x = \alpha_y$. Consequently, we can drop the k -label in the hopping elements $t_{x,n} = t_{y,n} = t_n$ and on-site energies $\epsilon_{x,n} = \epsilon_{y,n} = \epsilon_n$ of the Wilson chain Hamiltonian in Eq. (5.3). By introducing a convenient spinor notation (whose characteristic property is the *absence* of the x - or y -index on \hat{b} or $\hat{\sigma}$),

$$\hat{b} \equiv \begin{pmatrix} \hat{b}_x \\ \hat{b}_y \end{pmatrix}, \quad \hat{\sigma} \equiv \begin{pmatrix} \hat{\sigma}_x \\ \hat{\sigma}_y \end{pmatrix}, \quad (5.4)$$

we can write the Hamiltonian in a more compact way

$$\hat{H} = \hat{H}_{imp} + \sqrt{\frac{\eta}{\pi}} (\hat{\sigma}^\dagger \hat{b}_0 + \text{h.c.}) + \sum_n (\epsilon_n \hat{b}_n^\dagger \hat{b}_n + [t_n \hat{b}_n^\dagger \hat{b}_{n+1} + \text{h.c.}]). \quad (5.5)$$

In case of zero bias, i.e. $\hat{H}_{imp} = h_z \hat{\sigma}_z / 2$ with $h_x = h_y = 0$, the system possesses an abelian $U(1)$ symmetry in the xy -plane. In other words, the Hamiltonian is invariant under simultaneous rotation of the impurity spin in the $\sigma_x \sigma_y$ -plane and the bosonic baths in the $b_x b_y$ -planes by a generic angle ϕ . A rotation of this type can be induced by a unitary operator $\hat{U}(\phi)$,

$$|\psi\rangle \rightarrow \underbrace{e^{i\phi \hat{S}}}_{\hat{U}(\phi)} |\psi\rangle, \quad (5.6)$$

where \hat{S} is the generator of the $U(1)$ symmetry, given by

$$\hat{S} = \frac{1}{2} \hat{\sigma}_z + i \sum_n (\hat{b}_{y,n}^\dagger \hat{b}_{x,n} - \hat{b}_{x,n}^\dagger \hat{b}_{y,n}) = \frac{1}{2} \hat{\sigma}_z + \sum_n (\hat{b}_n^\dagger \sigma_y \hat{b}_n), \quad (5.7)$$

with \hat{S} commuting with the Hamiltonian in Eq. (5.5), $[\hat{H}, \hat{S}] = 0$.¹ In this form, the symmetry sectors of \hat{S} involve a hopping between the two bath in the local bosonic state spaces, which

¹Note that the spin operators acting in the local space of the impurity are always denoted by $\hat{\sigma}_i$, while σ_i without hat explicitly denotes a Pauli matrix.

poses a serious challenge for the numerical implementation of the symmetry. Hence, it is useful to bring \hat{S} in a diagonal form in the spinor space of \hat{b} by applying a canonical transformation to the bosonic spinor, $\tilde{b} \equiv U\hat{b}$. The particular choice

$$U = \frac{1}{\sqrt{2}} \begin{pmatrix} 1 & +i \\ 1 & -i \end{pmatrix} \quad (5.8)$$

transforms the generator into a diagonal form in the spinor space:

$$\hat{S} = \frac{1}{2}\hat{\sigma}_z + \sum_n (\hat{b}_n^\dagger \sigma_y \hat{b}_n) = \frac{1}{2}\hat{\sigma}_z + \sum_n (\underbrace{\hat{b}_n^\dagger U^\dagger}_{\equiv \tilde{b}^\dagger} U \sigma_y U^\dagger \underbrace{U \hat{b}_n}_{\equiv \tilde{b}}) \quad (5.9)$$

$$= \frac{1}{2}\hat{\sigma}_z - \sum_n (\tilde{b}_n^\dagger \sigma_z \tilde{b}_n) = \frac{1}{2}\hat{\sigma}_z + \sum_n (\tilde{b}_{y,n}^\dagger \tilde{b}_{y,n} - \tilde{b}_{x,n}^\dagger \tilde{b}_{x,n}), \quad (5.10)$$

where the relation $U\sigma_y U^\dagger = -\sigma_z$ was used in the second line. In this form, the symmetry sectors are characterized by the z -component of the impurity spin and the difference in the bosonic occupation number in both baths rather than a hopping term, allowing a simpler symmetry implementation [108].

The canonical transformation employed on the bosonic operators also affects the coupling term of the Hamiltonian, which is now given by

$$\hat{H} = \hat{H}_{imp} + \sqrt{\frac{2\eta}{\pi}} \sqrt{2} (\hat{\sigma}_- [\tilde{b}_{x,0} + \tilde{b}_{y,0}^\dagger] + \hat{\sigma}_+ [\tilde{b}_{x,0}^\dagger + \tilde{b}_{y,0}]) + \sum_n (\epsilon_n \tilde{b}_n^\dagger \tilde{b}_n + [t_n \tilde{b}_n^\dagger \tilde{b}_{n+1} + \text{h.c.}]). \quad (5.11)$$

Since the SBM2 Hamiltonian and \hat{S} commute, it follows that any eigenstate $|q\rangle$ of \hat{S} is also an eigenstate of \hat{H} , with $|q\rangle$ being defined as

$$\hat{S}|q\rangle = q|q\rangle \quad \text{with } q = \frac{1}{2}\sigma_z + \tilde{N}_y - \tilde{N}_x, \quad (5.12)$$

where $\tilde{N}_{x,y} = \sum_n \tilde{b}_{(x,y),n}^\dagger \tilde{b}_{(x,y),n}$ is the total number of bosons occupying the Wilson chain of the individual baths and σ_z is the spin component in z -direction. It follows that given any ground state $|G\rangle$, one may obtain another ground state via $e^{i\phi\hat{S}}|G\rangle$. In case of a two-fold degeneracy of the ground state, the corresponding subspace can be described by the states $|G_{q=\pm 1/2}\rangle$ with the following properties:

$$\hat{S}|G_{q=\pm 1/2}\rangle = \pm \frac{1}{2}|G_{q=\pm 1/2}\rangle \quad (5.13)$$

$$\hat{H}|G_{q=\pm 1/2}\rangle = E_g|G_{q=\pm 1/2}\rangle, \quad (5.14)$$

where E_g is the ground state energy. These two states are the only ones with a symmetric distribution of boson numbers ($\tilde{N}_x = \tilde{N}_y$). By construction, the expectation value $\langle \sigma_{x,y} \rangle$ evaluated using ground states that are also symmetry eigenstates is zero. How to reconstruct the magnetization of the 'original' ground state is explained in App. C.1.

Parity symmetry

In addition to the $U(1)$ symmetry present in the XY -symmetric model, the Hamiltonian is also invariant under parity transformations. There exist three different parity operators for

the SBM2 Hamiltonian, which can be defined as

$$\hat{P}_x = \hat{\sigma}_x e^{i\pi \hat{N}_y} \quad (5.15)$$

$$\hat{P}_y = \hat{\sigma}_y e^{i\pi \hat{N}_x} \quad (5.16)$$

$$\hat{P}_z = \hat{\sigma}_z e^{i\pi(\hat{N}_x + \hat{N}_y)} = -i\hat{P}_x\hat{P}_y. \quad (5.17)$$

where $\hat{N}_x = \sum_k \hat{b}_{kx}^\dagger \hat{b}_{kx}$ and $\hat{N}_y = \sum_k \hat{b}_{ky}^\dagger \hat{b}_{ky}$ count the total bosonic occupation numbers of the x - and y -bath. Note that the application of \hat{P}_z to a state can be carried out by combining \hat{P}_x and \hat{P}_y ($\hat{P}_z = -i\hat{P}_x\hat{P}_y$), hence \hat{P}_z does not describe an additional independent symmetry. The parity obeys C_{sv} , which is an abelian point group. It follows that

$$[\hat{P}_x, \hat{S}] \neq 0 \quad (5.18)$$

$$[\hat{P}_y, \hat{S}] \neq 0 \quad (5.19)$$

$$[\hat{P}_x, \hat{P}_y] \neq 0. \quad (5.20)$$

A joint symmetry implementation of \hat{P}_x or \hat{P}_y with \hat{S} is therefore not possible. On the other hand, the $U(1)$ symmetry already contains \hat{P}_z as a special case ($\hat{P}_z = \exp(i\pi\hat{S})$). Therefore the $U(1)$ eigenstates have a well defined parity eigenvalue p_z .

$$\hat{P}_z|q\rangle = p_z|q\rangle \quad (5.21)$$

where $p_z = +1$ in case of an state with a positive q -value, while $q < 0$ corresponds to a negative parity eigenvalue $p_z = -1$.

5.1.2 VMPS setup

In principle, two different setups exist for the VMPS implementation of the SBM2. In contrast to NRG, where the impurity is always located at the first site of the Wilson chain due to energy scale separation, VMPS enables one to place the impurity in the middle of two separate Wilson chains coupling to one bath at the left and one at the right side. The sweeping procedure then moves from the left end (first bath) across the impurity in the middle to right end (second bath) and back again optimizing the ground state.

However, when studying the XY -symmetric version of the SBM2 such a setup leads to numerical problems, since the ground state is very sensitive to small asymmetries in the spin-bath coupling $\eta_x = \eta_y = \eta$. A separate treatment of the baths during the sweeping may induce a coupling asymmetry, causing convergence problems of the ground state. Therefore we employ a different VMPS setup, which is based on multi-channel NRG implementations. By combining the local Hilbert spaces of the two bosonic baths on each site of the Wilson chain, we form 'super-sites' in a folded setup. This is achieved by replacing the matrix representation of the bosonic operators in Eq. (5.3) with

$$B_{x,n} = b_{x,n} \otimes \mathbb{I}_{y,n} \quad (5.22)$$

$$B_{y,n} = \mathbb{I}_{x,n} \otimes b_{y,n}, \quad (5.23)$$

where $\mathbb{I}_{xy,n}$ is the identity matrix in the respective local bosonic space on site n . A schematic picture of the folded setup is displayed in Fig. 5.1.

Though the folded setup reduces coupling asymmetries arising in the sweeping procedure, VMPS does not guarantee a priori that symmetries of the underlying model are conserved in the numerical procedure. Due to the exponentially decreasing energy scale along the Wilson chain, small numerical noise at early iterations may lead to symmetry breaking at

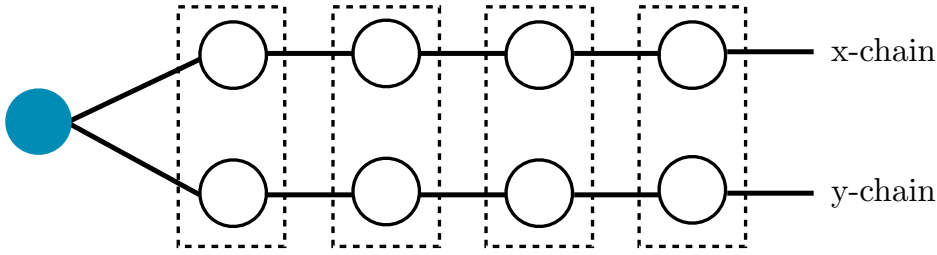


Figure 5.1: Schematic picture of the folded VMPS setup of the SBM2.

late iterations during the VMPS procedure. In our experience, these perturbations play a crucial role within the critical regime and near the phase boundaries for $0.75 < s < 1$ while the other phases of the SBM2 are more stable against these numerical effects. Being particularly interested in critical properties of the model, it is necessary to explicitly incorporate the aforementioned abelian $U(1)$ symmetry in the numerical setup by labeling the symmetry sectors according to the symmetry quantum number q in Eq. (5.12) with QSpace (see Sec. 3.1.5). This not only improves numerical stability, it also drastically speeds up calculation time. For a detailed comparison of the results obtained with and without the explicit conservation of the $U(1)$ symmetry see Sec. 5.5.

Note that we are not yet able to include a shift δ_n of the local bosonic basis into our symmetry implementation. The shift leads to additional terms in \hat{S} ,

$$\hat{S} = \frac{1}{2}\sigma_z + \sum_n (\tilde{b}_{y,n}^\dagger \tilde{b}_{y,n} + \frac{\delta_{y,n}}{\sqrt{2}}(\tilde{b}_{y,n} + \tilde{b}_{y,n}^\dagger) + \frac{\delta_{y,n}^2}{2} - \tilde{b}_{x,n}^\dagger \tilde{b}_{x,n} - \frac{\delta_{x,n}}{\sqrt{2}}(\tilde{b}_{x,n} + \tilde{b}_{x,n}^\dagger)) - \frac{\delta_{x,n}^2}{2}). \quad (5.24)$$

Because of the additional terms linear in δ_n , \hat{S} is no longer diagonal in the \tilde{b}_x - \tilde{b}_y plane. In combination with the continuous nature of δ_n , an implementation of the shift as indicated above together with the abelian $U(1)$ symmetry is not possible. Therefore the results of this chapter are obtained with two different versions of the VMPS code:

- Version 1 (V1) works with the standard one-site optimization scheme described in Sec. 3.3 and employs the displacement of the local bosonic basis sets. On the other hand this version does not guarantee the conservation of the $U(1)$ symmetry. It is employed for $0 < s < 1/2$, where the correct description of the critical phenomena requires a displaced oscillator basis, and in all calculations that include a symmetry breaking magnetic field $h_{x,y}$ in one of the directions of the bath couplings.
- Version 2 (V2) explicitly incorporates the $U(1)$ symmetry therefore requiring a two-site VMPS optimization scheme as described in App. A.1. Due to symmetry conservation, the bosonic displacement is not included. This limits the application of V2 to the regime $1/2 < s < 1$, where results do not depend on the shifted basis. The symmetry-improved VMPS version is used for all calculations of the critical phenomena for $1/2 < s < 1$ which do not involve symmetry breaking magnetic field. Moreover, all VMPS energy-flow diagrams are generated with V2.

5.2 Ground state phases

We begin by briefly reviewing the main findings of Guo et al. [21]. The physical properties of ground-state in the XY -symmetric two-bath spin-boson model at zero temperature and zero bias fields $h_x = h_y = 0$ are determined by the competition of the two baths in the xy -plane and a perpendicular external field in z -direction, all trying to align the impurity spin in their respective direction. The symmetric bath coupling constants $\alpha_x = \alpha_y = \alpha$, the strength of the external field h_z and the value of the bath exponent s are the determining parameters of the ground state phase diagram, which is schematically illustrated in Fig. 5.2. In contrast to

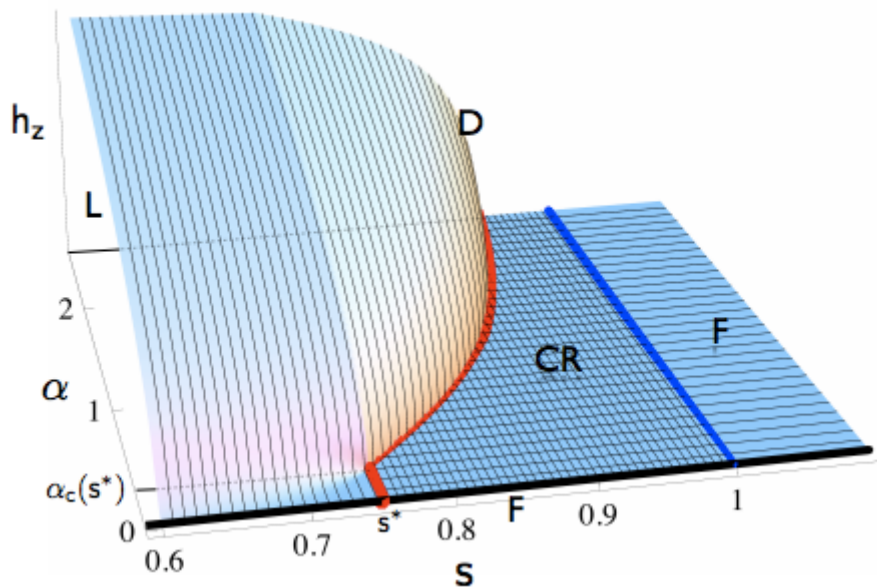


Figure 5.2: Schematic phase diagram (adapted from [21]) of the two-bath spin-boson model as function of the bath exponent s , the coupling α and the transverse field h_z . The localized (L) and delocalized (D) phase are separated by the colored plane representing the critical field h_{zc} . In the $h_z = 0$ plane, the critical phase (CR) exists for $s > s^*$ and small coupling α . At a critical coupling α_c , illustrated by the red line, a phase transition occurs from the critical to the localized phase. The critical phase is unstable with respect to a finite transverse field and is separated from the free phase (F) by the line $s = 1$ (blue line).

the standard one-bath spin-boson model, the sub-ohmic SBM2 includes three distinct types of ground states phases:

- At strong couplings exists a localized phase, where the strength of the dissipation suffices to align the impurity spin in direction of the bath couplings in the xy -plane resulting in a finite magnetization, $\langle \sigma_{x,y} \rangle \neq 0$. A ground state in the localized regime exhibits a two-fold degeneracy.
- In the delocalized phase at weak couplings (or for strong values of h_z) the baths do not succeed in localizing the spin in the xy -plane, therefore any state in this regime has zero magnetization in the directions of the bath couplings, $\langle \sigma_{x,y} \rangle = 0$, but aligns parallel to h_z , $\langle \sigma_z \neq 0 \rangle$. In contrast to the localized and the critical phase, a delocalized ground state is always non-degenerate.
- The so-called critical phase at intermediate couplings is a special feature of the XY -symmetric SBM2; it is characterized by $\langle \vec{\sigma} \rangle = 0$, a non-linear response of $\langle \vec{\sigma} \rangle$ to an

applied magnetic field \vec{h} and a two-fold ground state degeneracy. This behavior corresponds to a fluctuating fractional spin [95, 106] generated by the competing bath couplings partially neutralizing each other. This phase explicitly requires a XY -symmetric setup; already small asymmetries in the coupling constants, $\alpha_x \neq \alpha_y$, destabilize it (see Sec. 5.4).

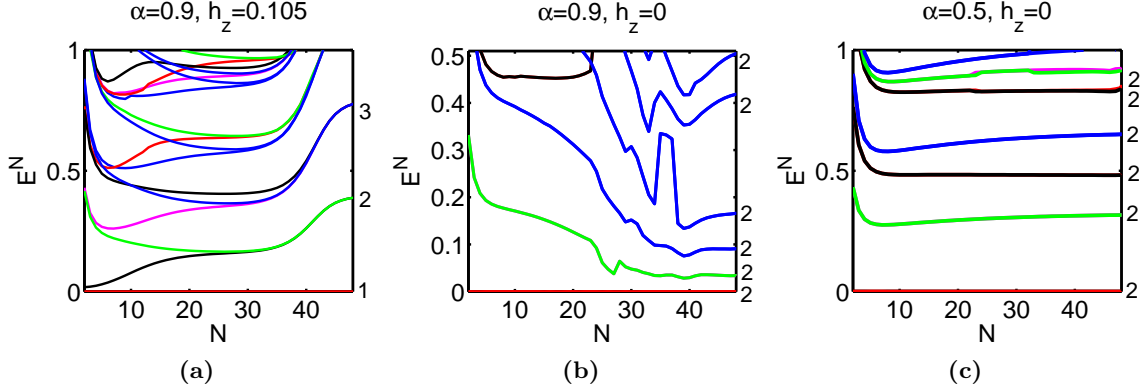


Figure 5.3: Characteristic VMPS energy-flow diagrams for the sub-ohmic SBM2 with $s = 0.8$, in the three ground state phases for different values of α and h_z . The energy-levels flow to a delocalized (a), localized and critical (c) fixed point, where the degree of degeneracy of each state is indicated by the numbers on the right side of each panel. While the localized and critical fixed point show a two-fold degeneracy, the delocalized fixed point is non-degenerate [V2: $N = 50$, $D = 60$, $d_{opt} = 40$, $\Lambda = 2$].

The phases correspond to three stable RG fixed points with distinct flow characteristics illustrated in the VMPS flow diagrams in Fig. 5.3. Which of the fixed points is reached strongly depends on the interplay of three model parameters, namely the bath exponent s , the coupling strength α and the perpendicular external field h_z , as schematically illustrated in Fig. 5.4. It follows from the RG equations that the critical fixed point is located at intermediate couplings $\alpha^* = 1 - s + O[(1 - s)^2]$ and $h_z = 0$. While originally assumed to be present for all $0 < s < 1$ [106], the critical fixed point exists only for $h_z = 0$ and $s > s^*$ with $s^* = 0.75 \pm 0.01$ being a universal lower bond s indicated in Fig. 5.2 [21]. In this regime of s , a strong coupling $\alpha > \alpha_c$ drives the system from a critical to a localized fixed point separated by a continuous quantum phase transition at $\alpha = \alpha_c$ corresponding to an additional unstable fixed point (dubbed QC1 in the following). In contrast to the critical phase, the system can stay in the localized phase for all s down to $s = 0$, although a strong enough transverse field h_z may destabilize it. For $h_z > h_{zc}$ the flow reaches a delocalized fixed point, with the transition between localized and delocalized phase being characterized by another continuous quantum phase transition located at $h_z = h_{zc}$, that corresponds to a second unstable fixed point (labeled QC2). Both phase transitions are topic of extensive studies in the remainder of this chapter, where the first numerical results examining the critical phenomena of the SBM2 are presented.

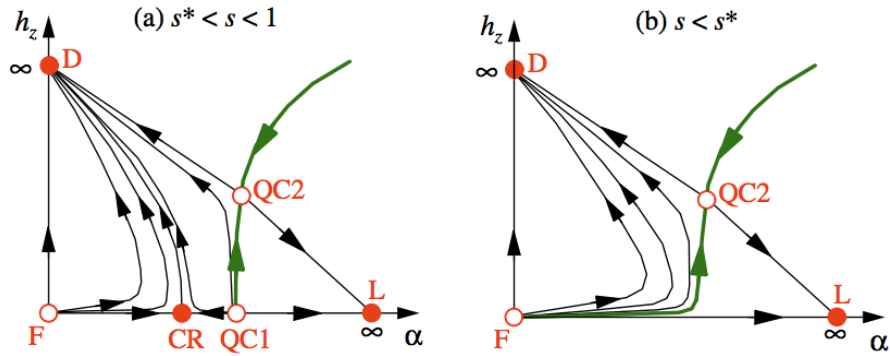


Figure 5.4: Schematic RG flow (adapted from [21]) of the two-bath spin-boson model as function of the coupling α and the transverse field h_z , where the thick lines correspond to a continuous QPT and the full (open) circles indicate stable (unstable) fixed points. Only in (a) with $s^* < s < 1$ the flow reaches the critical fixed point (CR) for small α and $h_z = 0$, which is separated from the localized fixed point (L) by the critical QC1 fixed point. As indicated in (b), CR and QC1 disappear for $s < s^*$.

5.2.1 Properties of critical coupling phase

As already discussed, the critical phase corresponds to a partially-screened impurity spin with zero magnetization in the ground state, $\langle \vec{\sigma} \rangle = 0$. However, the VMPS calculations find a small but still finite magnetization, as indicated in Fig. 5.5(a), where the behavior of $\sigma_{x,y}$ is displayed in the transition from the localized to the critical phase. We clearly observe a decay towards the critical phase, nevertheless the magnetization remains at a finite value $10^{-2} \neq 0$. This effect was previously interpreted as a result of $U(1)$ symmetry breaking in the numerical optimization procedure [109]. However, the data shown in Fig. 5.5(a) was obtained using the symmetry improved VMPS code (V2), thus demonstrating the non-vanishing magnetization is *not* caused by $U(1)$ symmetry breaking. Instead, we find that finite-size effects within the critical regime are the actual reason for the numerical discrepancy, as illustrated in Fig. 5.5(b). While $m = \sqrt{\langle \sigma_x^2 \rangle + \langle \sigma_y^2 \rangle}$ approaches the well-defined physical value $m_0 = 0$ in the limit of an infinitely large system size $L \rightarrow \infty$, we observe corrections for finite systems that decrease exponentially with the effective system size L ,

$$m = a \frac{1}{L^p} = a(\Lambda^{-N})^p = ae^{-\ln(\Lambda)pN}, \quad (5.25)$$

where we used $L = \Lambda^{-N}$ in the second line (analogous to the discussion of the standard SBM in Sec. 4.1.3). Our results in Fig. 5.5(b) clearly show that the finite size correction vanishes with a small exponent p , leading to finite values of m for the chain lengths ($N = 50$) that are typically used in our calculations.

Nevertheless, the finite-size effects do not influence the characteristic non-linear response of the impurity spin in the critical regime, which is of power law type

$$\langle \sigma_{x,y} \rangle \propto h_{x,y}^{1/\delta}, \quad \langle \sigma_z \rangle \propto h_z^{1/\delta'}, \quad (5.26)$$

with $\delta, \delta' > 1$. Perturbative RG calculations around the free-spin fixed point at $\alpha = 0$ predict a scaling of the exponents with s ,

$$1/\delta = \frac{1-s}{2} + O([1-s]^2), \quad (5.27)$$

$$1/\delta' = 1-s + O([1-s]^2). \quad (5.28)$$

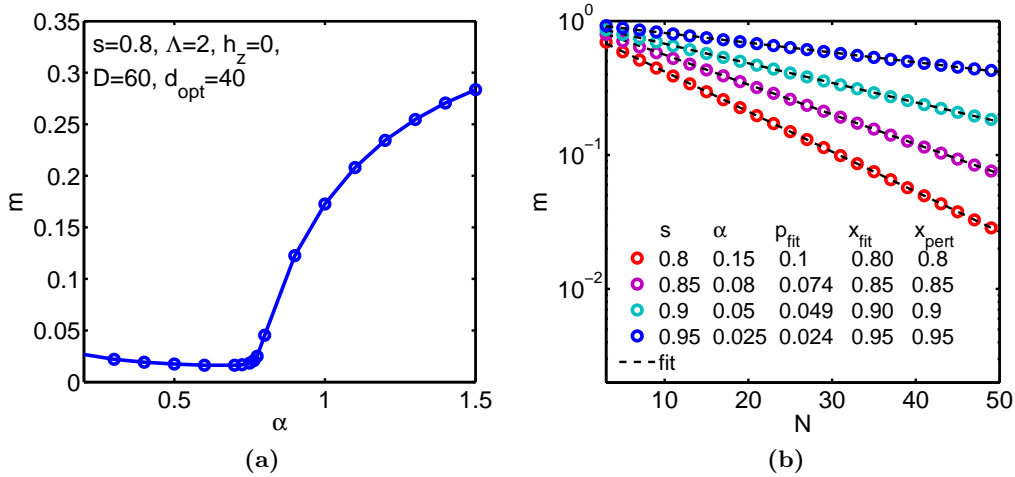


Figure 5.5: Magnetization $m = \sqrt{\langle \sigma_x^2 \rangle + \langle \sigma_y^2 \rangle}$ inside the critical phase. In (a) m is displayed for the transition between localized and critical phase with $\alpha_c \approx 0.7684$. We observe that m remains non-zero in the critical regime due to finite-size effects. The finite-size scaling in (b) illustrates that the magnetization decays only slowly with increasing Wilson chain length N characterized by the exponent p . The temperature exponent x extracted from the finite-size scaling corresponds excellent with perturbative RG predictions of Eq. (5.29) [V2: $N = 50$, $D = 60$, $d_{opt} = 40$, $\Lambda = 2$].

Numerical results of the non-linear response in the critical regime are displayed in Fig. 5.6 for different values of s . As already shown in [21], we can observe a clear power law scaling over several orders of magnitude and find good agreement with the perturbative predictions for both δ and δ' . The small deviations of the numerical data from the RG calculations for larger values of $(1 - s)$ is expected, since the higher order contributions in Eqs. (5.27) and (5.28) become more important.

Furthermore, the exponent p characterizing the finite-size corrections in Eq. (5.25) allows us to calculate the temperature exponent x in the critical phase, if we can neglect the massflow error. As discussed in Sec. 4.1.3 in context of the one-bath SBM, we can determine x by the relation $1 - x = -2p$. The perturbative RG predictions for x are given in first order by

$$1 - x = 1 - s + O([1 - s]^2). \quad (5.29)$$

The VMPS results of p and x for different values of s are displayed in Fig. 5.5(b). Similar to the non-linear response of the impurity spin, x also shows excellent agreement with the perturbative RG calculations. Note that the calculation of x relies on the irrelevance of the massflow error in the critical phase, which is only a hypothesis, so far. Though the excellent agreement with the RG predictions strongly supports this assumption, we should keep it in mind when interpreting VMPS results involving x .

Note that for all calculations carried out in this section, α was chosen so that the system is located near the stable intermediate-coupling fixed point at $\alpha^* = 1 - s + O([1 - s]^2)$ arising from the RG flow equations. Tuning α towards the critical fixed point coupling α^* , the unconventional behavior of the impurity spin within the critical phase becomes most pronounced. At the same time the system is less sensitive to numerical perturbations in comparison to other points in the critical phase. We can determine the value of α^* for different s using the VMPS flow diagrams displayed in Fig. 5.7. Close to α^* , the flow shows a very flat behavior at early iterations with only minor weak bending of the lines towards the

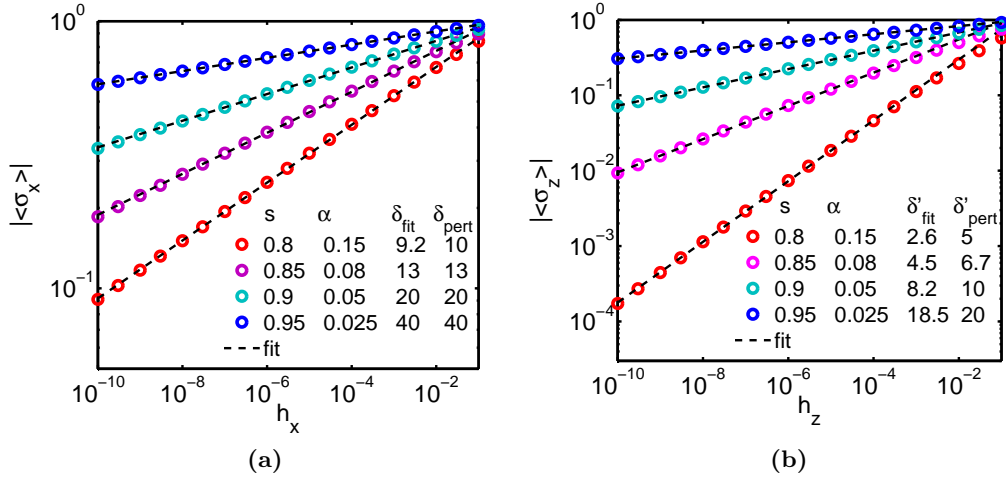


Figure 5.6: Non-linear response of the symmetry spin inside the critical phase to a transverse field h_z (a) and a in-plane bias field h_x (b) for different values of s . We find the expected power law behavior of the non-linear response in agreement with the perturbative RG predictions in Eq. (5.27) and (5.28) [V2: $N = 50$, $D = 60$, $d_{\text{opt}} = 40$, $\Lambda = 2$].

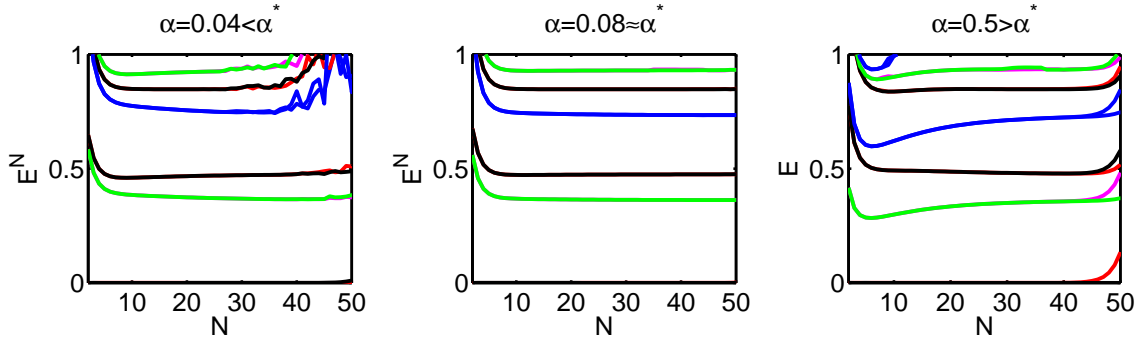


Figure 5.7: Energy-level flow diagrams for fixed $s = 0.85$ and different values of α close to the critical fixed point.

final converged fixed point – a typical characteristic of a system close to a fixed point. For values of α below (beyond) α^* we observe a downwards (upwards) bending of the flow before reaching a plateau. We can use this property to determine α^* qualitatively by examining the flow diagrams.

5.2.2 Determining the phase boundaries

In order to study the critical phenomena of the SBM2, it is necessary to determine the phase boundaries of QC1 and QC2 accurately, i.e. to numerically calculate the critical coupling α_c and the critical transverse field h_{zc} , which define the location of QC1 and QC2, respectively. A strategy involving the VMPS flow diagrams is prone to errors, since the flow of the SBM2 is very sensitive to numerical noise at later iterations – even if the $U(1)$ symmetry is incorporated in the code. At the same time, the use of the order parameter to approximately determine the phase boundary and then employ a ‘best power law’ method as in [21], i.e. to tune α_c and h_{zc} until $\langle \sigma_{x,y} \rangle$ shows the best power law scaling at the phase transition, might work

for QC2. However, since the order parameter is not an accurate indicator for the location of QC1 due to the non-vanishing magnetization in the critical phase caused by finite-size corrections, the application of the method to QC1 is not possible.

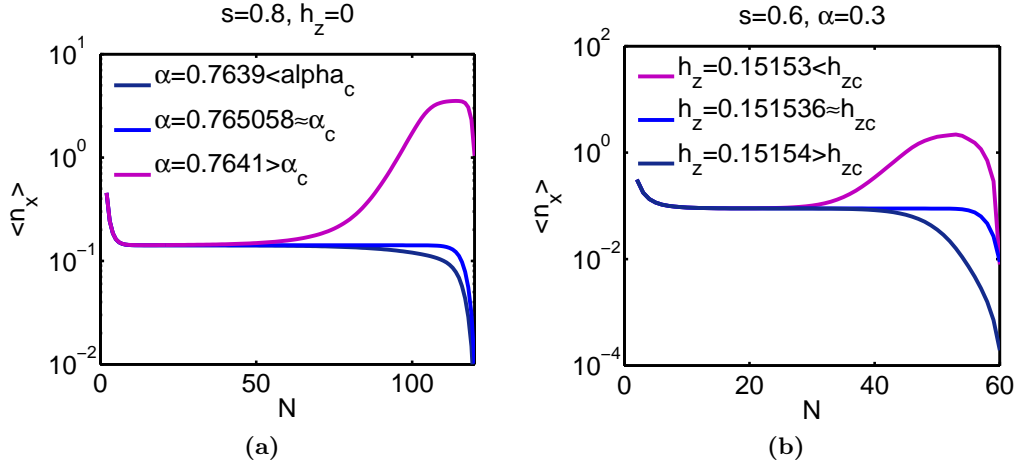


Figure 5.8: Characteristic behavior of the bosonic occupation numbers on the Wilson chain near QC1 (a) and QC2 (b). In both cases, the occupation numbers stay almost constant throughout the chain directly at the phase boundary, while increasing towards the end of the chain in the localized phase. In the delocalized and critical regime, we observe a steady decay.

In our experience, the most accurate and at the same time most efficient way to calculate α_c and h_{zc} is to distinguish the phases by the characteristic behavior of the bosonic occupation numbers $\langle n_{x,y} \rangle$ on the Wilson chain. Similar to the one-bath SBM, the average occupation of boson modes increases towards the end of the Wilson chain in the localized phase, while it decreases in both critical and delocalized phases. Moreover, at the critical points QC1 and QC2 the occupation numbers stay almost constant throughout the chain, except for a sharp decay at the end. This characteristic behavior, illustrated in Fig. 5.8, can be used to determine the phase boundaries with high accuracy. We have thus adopted this approach throughout for determining the α -values involved in the results described below. Note that the accessible accuracy depends again on the chain length N : the calculation of α_c or h_z up to a decimal points requires a minimal chain length

$$N \propto a\nu \frac{\ln(10)}{\ln \Lambda}, \quad (5.30)$$

where ν is the critical exponent of the correlation length. As described in the following section, it often is necessary to use chain lengths $N > 100$, since ν is particularly small for QC1.

5.3 Critical Phenomena

So far, the critical properties of the SBM2 have not been studied in the literature. The emergence of the critical phase without classical counterpart leads to highly non-trivial critical properties. While quantum-to-classical correspondence suggests that the QPT between localized and delocalized phase corresponds to the thermal transition in a classical XY -symmetric spin-chain with long-range interactions, the transition between critical and localized phase has no classical counterpart. In this section, we extensively examine the critical properties of the SBM2 using VMPS with the aim to characterize the two phase transitions by calculating the corresponding critical exponents, summarized in Table 5.1.

physical Quantity	Definition	Exponent	Condition
Local magnetization	$\langle \sigma_{x,y} \rangle \propto g ^{-\beta}$	β	$ g \rightarrow 0, h_{x,y} = 0, T = 0$
Local magnetization	$\langle \sigma_{x,y} \rangle \propto h_{x,y} ^{-1/\delta}$	δ	$g = 0, h_{x,y} \rightarrow 0, T = 0$
Correlation length	$\xi \propto g ^{-\nu}$	ν	$ g \rightarrow 0, h_{x,y} = 0, T = 0$
Local susceptibility	$\chi \propto T^{-x}$	x	$g = 0, h_{x,y} = 0, T \rightarrow 0$

Table 5.1: Critical exponents of the two-bath spin-boson model where $\langle \sigma_{x,y} \rangle$ is the magnetization of the impurity, $h_{x,y}$ a bias of the impurity spin in the respective coupling direction, T the temperature, ξ the correlation length and χ the susceptibility of the impurity. The coefficient g denotes the distance to the critical point, where $g = \alpha - \alpha_c$ at QC1 and $g = h_{z_c} - h_z$ at QC2.

5.3.1 Quantum critical point 1 (QC1)

We begin the analysis of the critical behavior of the symmetric SBM2 with the quantum phase transition between the localized and the critical phase, dubbed quantum critical point 1 (QC1). Only present at zero transverse field ($h_z = 0$), the dependence of the critical coupling α_c on the bath exponent s is illustrated in Fig. 5.9(a). The VMPS calculations

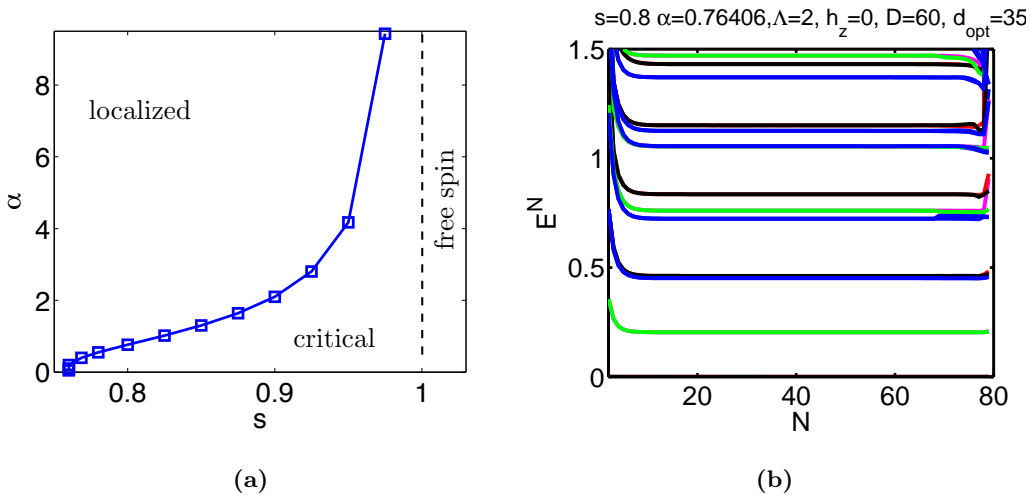


Figure 5.9: (a) Phase diagram in the $h_z = 0$ plane and (b) energy flow for a typical point at QC1. Employing the above described procedure to determine the critical coupling $\alpha_c(s)$, in (a) the location of the phase boundary between localized and critical phase is shown for various values of s . The VMPS flow diagram in (b) displays a completely smooth behavior, which is a signature of the fixed point at QC1.

indicate that QC1 moves towards $\alpha \rightarrow \infty$ for $s \rightarrow 1^-$, while lowering s decreases the critical coupling. In the limit of $s \rightarrow s^{*+}$, QC1 merges with the critical fixed point and disappears for $s < s^*$, which also implies that phase boundary between the critical and localized phases is vertical at s^* and small α .

The critical behavior of the SBM2 at QC1 is particularly interesting, because there is no classical counterpart to this phase transition. In contrast to QC2, quantum-to-classical correspondence breaks down for QC1, since a path integral representation of SBM2 leads to negative Boltzmann weights in the absence of a finite h_z [21]. This introduces an additional difficulty, since no predictions from classical models can be consulted in order to check the validity of the VMPS results presented below. Nevertheless, we may consider the hyperscaling relations,

$$\delta = \frac{1+x}{1-x}, \quad (5.31)$$

$$2\beta = \nu(1-x), \quad (5.32)$$

which should be valid as long as the system's dimension is below its upper critical dimension d_{uc} .

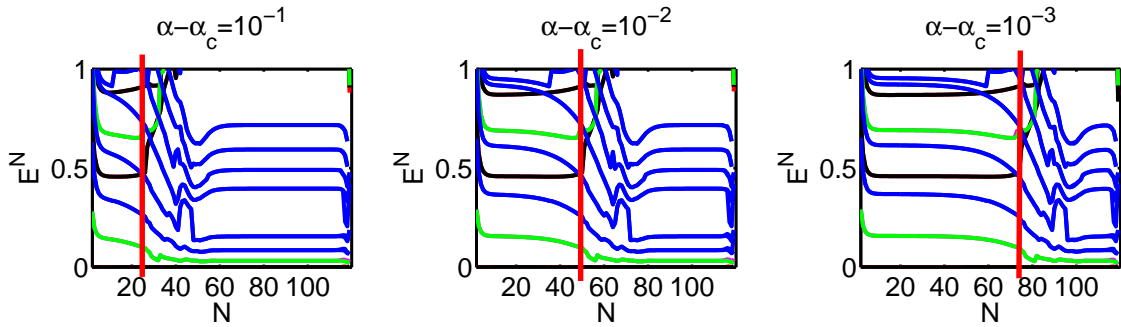


Figure 5.10: Energy-level flow diagrams for $s = 0.85$ in the localized phase close to QC1. The smooth behavior in the first iterations reflects the criticality while the bending and jumps in the lines indicate that the system flows to a localized fixed point. The red bar illustrates the iteration characteristic iteration N^* of the transition used to calculate the low-energy scale T^* .

The correlation length exponent ν characterizes how the low-energy scale T^* vanishes close to QPT, $T^* \propto |\alpha - \alpha_c|^\nu$. By analyzing the behavior of the energy flow close to the critical point we are able to calculate ν . To this end, we determine the iteration N^* where the flow starts to deviate significantly from the characteristic flow at QC1, illustrated in Figs. 5.9(b) and 5.10. The latter displays typical flow diagrams close to QC1, where the transition is indicated with a red bar corresponding to the iteration N^* , where the first excited energy level drops below $E < 0.05$ (in rescaled energy units). For practical purposes, ν was calculated by moving from the localized phase to the critical point. The energy scales T^* determined from such an analysis, finally, are collected and analyzed in Fig. 5.11(a). The VMPS calculations for ν strongly suggest that ν diverges both in the limit $s \rightarrow s^{*+}$ and $s \rightarrow 1^-$, a typical result for a system below its upper critical dimension. For s close to 1, the leading term characterizing the exponent seems to be $1/\nu = 1 - s + O[(1 - s)^2]$.

Panel (b) of Fig. 5.11 displays the results for the critical exponent β describing the scaling of the magnetization $\langle \sigma_{x,y} \rangle$ close to QC1. While the upper panel displays a typical loglog plot used for the extraction of β , the lower panel shows the dependence of β on different values of s . We find increasing values of $\beta > 1$ for $s \rightarrow s^*$, while in the limit of $s \rightarrow 1^-$ the VMPS calculations suggest that β approaches $1/2$. The latter is consistent with the hyperscaling

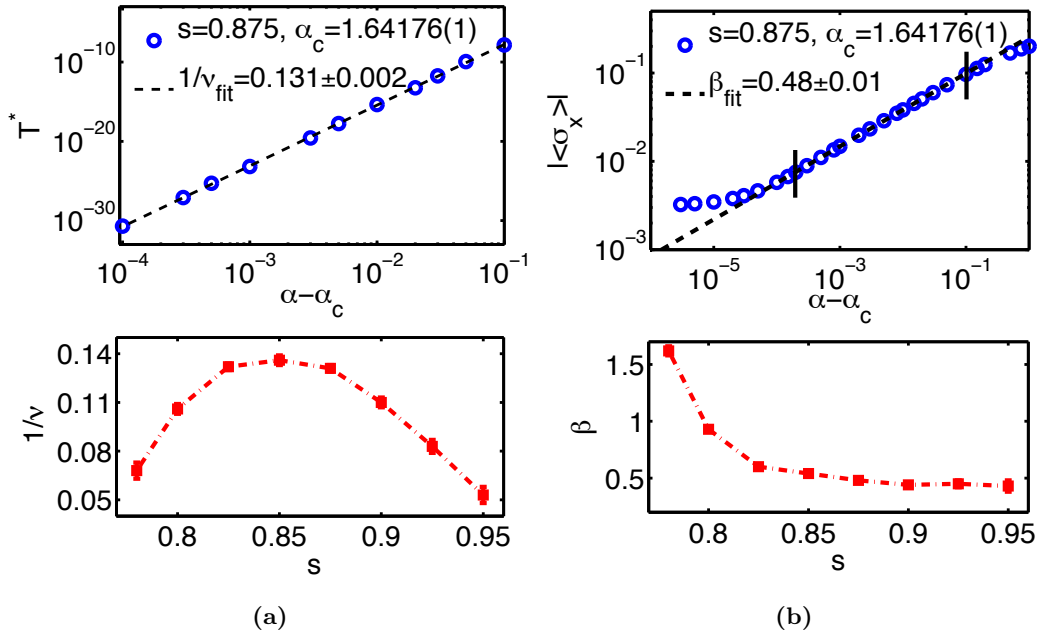


Figure 5.11: VMPS results for the critical exponents ν and β for various values of s at QC1. The upper panel in (a) displays a typical plot of the low-energy scale T^* vanishing as $|\alpha - \alpha_c|^\nu$ for $s = 0.875$, while the dependency of ν on s is illustrated in the lower panel. Similarly, (b) shows both the scaling of the magnetization $\sigma_x \propto (\alpha - \alpha_c)^\beta$ for $s = 0.875$ (upper panel) and the resulting values of β for various s at QC1 (lower panel). All VMPS data corresponding to the lower panels in (a) and (b) can be found in Figs. C.4 and C.5, respectively.

relation in Eq. (5.32), assuming that the temperature exponent follows the relation $x = s$ (see below). Note that determining β is particularly complicated for QC1, since the large values of ν require very long Wilson chains in order to resolve the critical properties. At the same time, calculations become sensitive to numerical noise due to the vicinity to the critical phase. Therefore the usage of the symmetry code V2 is essential in order to generate a clean power law scaling of the magnetization over several orders of magnitude, as illustrated in Fig. 5.11(b). One could worry whether V2 leads to inconsistent results for β , since it does not include a displaced local bosonic basis. But as discussed in Sec. C.2, the treatment of QC1 does not require a shifted basis. The results presented here thus should be correct within the fitting error.

Considering the temperature exponent x at QC1, we used a finite-size scaling of the magnetization $m = \sqrt{\langle \sigma_x^2 \rangle + \langle \sigma_y^2 \rangle}$ to extract the exponent p , which characterizes the decay of finite-size corrections to m , as discussed in previous sections. Assuming that hyperscaling is valid and the mass-flow error can be neglected (see below), the relation $-2p = 1 - x$ is employed to determine the critical exponent x . The VMPS results for x at QC1 are shown in Fig. 5.12(a), where the blue squares denote the values of x extracted from the finite-size scaling displayed in Fig. 5.13, while the red crosses are calculated via the hyperscaling relation in Eq. (5.32) using the numerical values of β and ν presented in Fig. 5.11. Both methods show excellent agreement with $x = s$ for the complete range of s at QC1. This result already supports the validity of hyperscaling at QC1.

Following this hypothesis and assuming that $x = s$ is a valid results, the hyperscaling

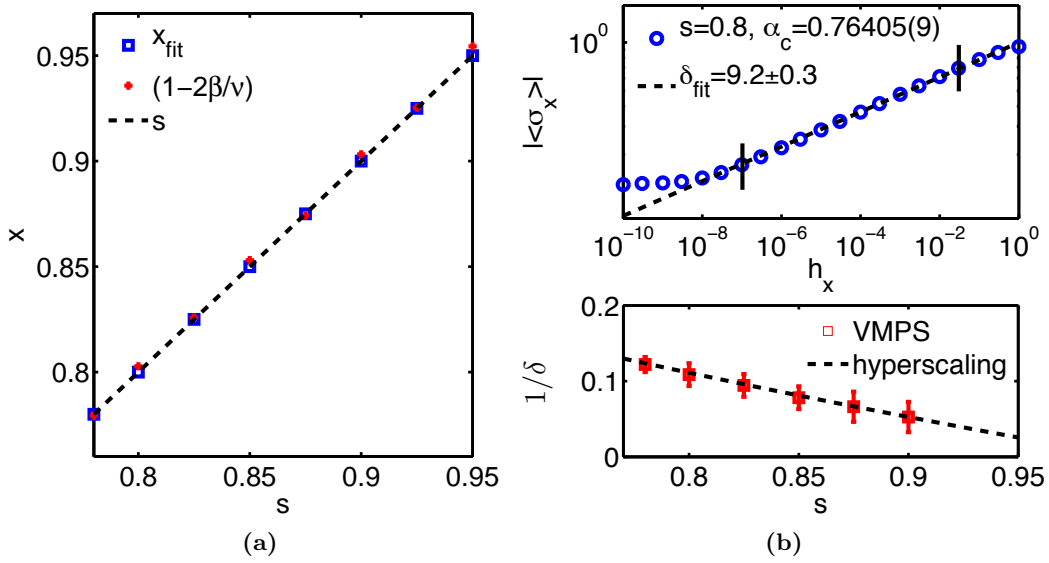


Figure 5.12: VMPS results for the critical exponents x and δ at QC1. In (a) x is displayed for different values of s calculated via finite-size scaling (blue squares) and with the hyperscaling relation in Eq. (5.32) using VMPS results of β and ν . The results of both methods show excellent agreement with $x = s$ (note that $|x_{\text{fit}} - s| < 10^{-5}$ [!]). The upper panel of (b) illustrates the scaling of $\sigma_x \propto h_x$ at the phase boundary for an typical value of $s = 0.8$ used to determine δ . The lower panel shows that the dependence of δ on s follows the hyperscaling relation in Eq. (5.33). All VMPS data corresponding to the lower panels in (b) can be found in Fig. C.6.

relation for the critical exponent δ in Eq. (5.31) is given by

$$\delta = \frac{1 + s}{1 - s}. \quad (5.33)$$

VMPS calculations of δ confirm hyperscaling as shown in Fig. 5.12(b). While the upper panel shows the scaling of $\langle \sigma_x \rangle$ for a typical value of $s = 0.8$ at QC1, the data shown in the lower panel strongly indicates that δ follows Eq. (5.33) for various values of s at the phase boundary. All VMPS calculations thus suggest that the critical exponents at QC1 follow hyperscaling. Nevertheless, we should keep in mind, that this conclusion is only correct if the VMPS results of x are not corrupted by the massflow error. So far, this is only a hypothesis, although our additional findings for β , δ and ν strongly support its validity.

Similar to β , the determination of δ in the asymptotic limit $s \rightarrow 1^-$ becomes increasingly difficult, since very long Wilson chains are required due to the divergence of the exponent ν . In addition, the finite external magnetic field h_x breaks the $U(1)$ symmetry implying that in all calculations of δ , we had to use the slower and less accurate version V1 instead of the symmetry improved V2.

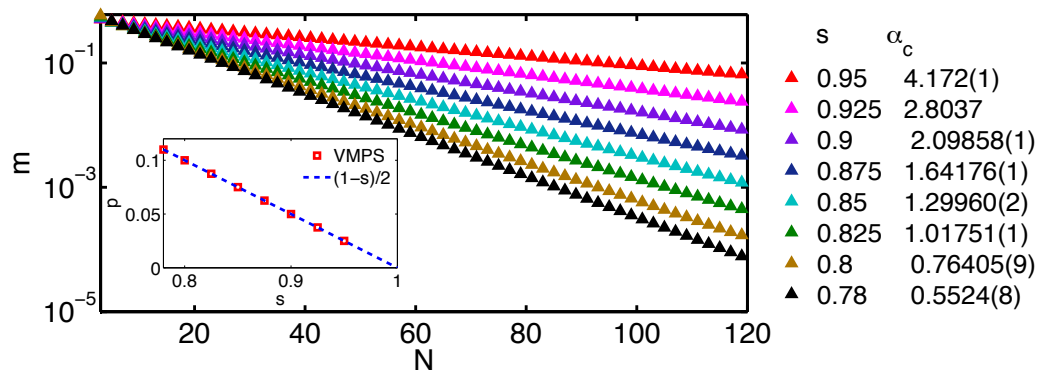


Figure 5.13: Finite-size scaling of the magnetization for various values of s at QC1. The inset shows the s -dependence of the exponent p which characterizes the vanishing magnetization at QC1. For all considered values of s the exponent follows $p = (1 - s)/2$ with high accuracy, indicating that $x = s$ at QC1.

5.3.2 Quantum critical point 2 (QC2)

In case of a finite transverse field h_z , the critical phase becomes unstable and disappears together with QC1. For any $0 < s < 1$, the ground state of the system may then either be localized or delocalized, depending on the interplay of the coupling strength α and the magnetic field h_z . The quantum phase transition separating the two regimes is reached at the critical field $h_z = h_{zc}$ and is governed by the quantum critical point 2 (QC2).

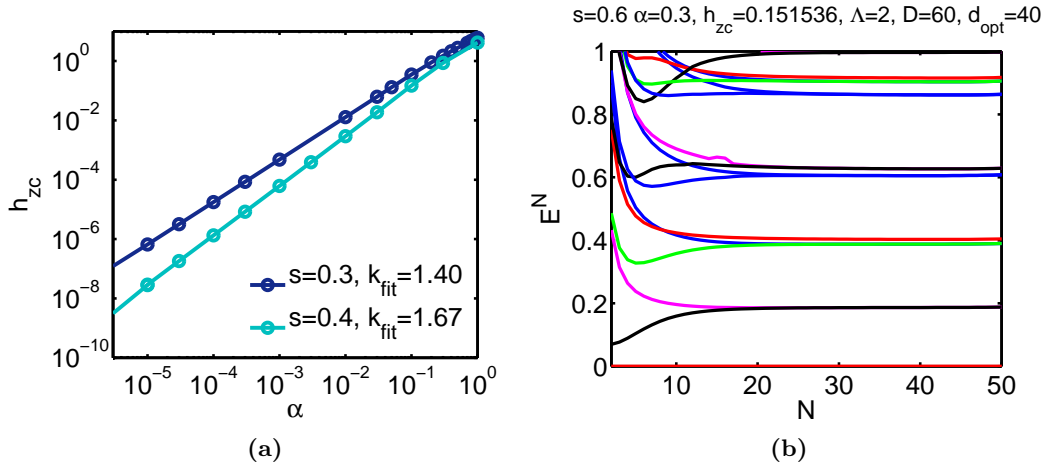


Figure 5.14: (a) The dependence of the critical field h_{zc} on the coupling constant α for different values of s , which follows a power law relation in the asymptotic limit $h_{zc} = \alpha^k$, with $k = 1/(1-s)$. The VMPS flow diagram in (b) displays a completely smooth behavior, which is a signature of the fixed point at QC2.

The phase boundary strongly depends on the bath exponent s and the coupling constant α . For small α , the values of h_{zc} follow a power law relation, $h_{zc} \propto \alpha^k$. As indicated in Fig. 5.14(a), the VMPS data agree well with the result of weak coupling RG, which states that $k = 1/(1-s)$.

In contrast to QC1, this phase transition has a classical counterpart. Employing quantum-to-classical correspondence, it is possible to map QC2 onto the thermal phase transition of a classical XY -symmetric spin chain with long-range interactions. The resulting predictions for the critical exponents resemble those of the standard spin-boson model with mean-field behavior for $0 < s < 1/2$ and hyperscaling for $1/2 < s < 1$.

We studied QC2 extensively using VMPS and are able to confirm the predictions of quantum-to-classical correspondence for a wide range of the bath exponent s . For the critical exponents β and δ , which characterize the scaling behavior of the magnetization $\langle \sigma_{x,y} \rangle$ near the phase boundary, quantum-to-classical correspondence makes the following predictions:

$$\beta = \frac{1}{2} \quad \text{for } s < 1/2, \quad (5.34)$$

$$\beta = 1/[2 + (12/5)\epsilon] \quad \text{for } s = 1/2 + \epsilon, \quad \epsilon \ll 1, \quad (5.35)$$

$$\beta = 1/[2 + O(\epsilon'^2)] \quad \text{for } s = 1 - \epsilon', \quad \epsilon' \ll 1, \quad (5.36)$$

$$\delta = 3 \quad \text{for } s < 1/2, \quad (5.37)$$

$$\delta = (1+s)/(1-s) \quad \text{for } s > 1/2. \quad (5.38)$$

The corresponding VMPS results are displayed in Fig. 5.15. While the upper panels in (a) and (b) show typical power law fits of β and δ for $s = 0.4$, the lower panels illustrate the dependence of both exponents on s . The mean-field results $\beta = 1/2$ and $\delta = 3$ are clearly

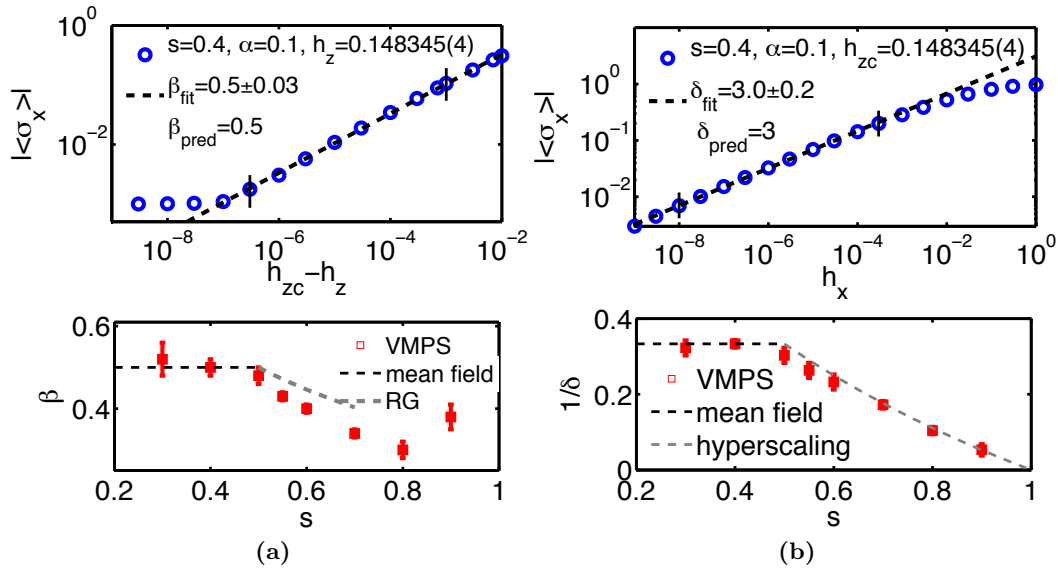


Figure 5.15: VMPS results for the critical exponents β and δ at QC1. The upper panels in (a) and (b) display the power law scaling of the magnetization at the phase boundary for fixed $s = 0.4$, from which the exponents β and δ are extracted. The lower panels show the dependence of β (a) and δ (b) for various values of s , both following mean-field behavior for $0 < s < 1/2$. All VMPS data corresponding to the lower panels in (a) and (b) can be found in Figs. C.7 and C.8, respectively.

reached for $0 < s < 1/2$ within the error-bars, while we observe deviations from the RG predictions for β in the regime $s = 1/2 + \epsilon$ with $\epsilon \ll 1$. This discrepancy might be caused by logarithmic corrections to the leading power laws which are expected near $s = 1/2$, since the transition is at its upper critical dimension for this particular value of the bath exponent. In the limit of $s \rightarrow 1^-$, β shows the tendency to approach the value $1/2$ as suggested in Eq. (5.36). The critical exponent δ follows the hyperscaling relation in Eq. (5.38) for all $1/2 < s < 1$ with small deviations only around $s = 1/2$.

Moreover, our analysis includes the correlation length exponent ν , which according to quantum-to-classical correspondence is given by

$$1/\nu = s \quad \text{for } s < 1/2, \quad (5.39)$$

$$1/\nu = 1/2 - (3/5)\epsilon \quad \text{for } s = 1/2 + \epsilon, \quad \epsilon \ll 1, \quad (5.40)$$

$$1/\nu = 1/\epsilon' \quad \text{for } s = 1 - \epsilon', \quad \epsilon' \ll 1. \quad (5.41)$$

Analogous to QC1, we calculated ν by determining the cross-over scale $T^* \propto |h_{zc} - h_z|^\nu$ using the VMPS energy-flow diagrams. For both practical purposes and consistency with our treatment of QC1, we approached QC2 from the localized phase and identify the deviation from the critical flow at the iteration N^* , where the first excited energy level drops below $E < 0.05$. In such an analysis, we determine a vanishing low-energy scale T^* that allows the extraction of ν as illustrated in Fig. 5.16. The upper panel of Fig. 5.16(a) displays the vanishing energy scale T^* for a fixed $s = 0.5$ at QC2, while the lower panel shows $\nu(s)$ for various values of s . The predicted mean-field behavior of Eq. (5.39) is clearly visible for $0 < s < 1/2$, while ν shows deviations from the RG results near $s = 1/2$. Similar to the previous discussion on δ and β , this might be caused by logarithmic corrections arising from the transition of system below its upper critical dimension.

In order to test the validity of the VMPS results for ν and β near $s = 1/2 + \epsilon$, we consider

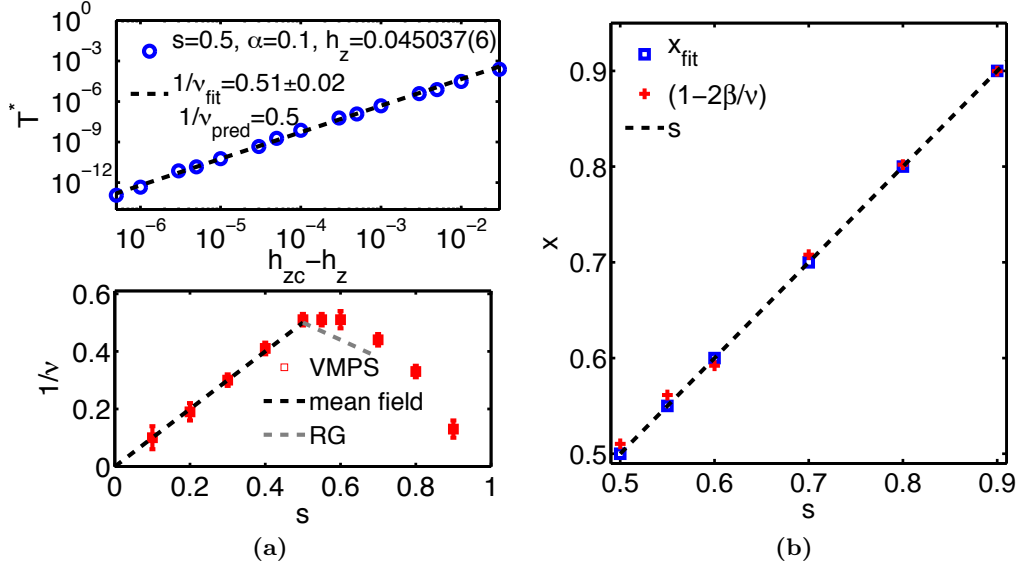


Figure 5.16: VMPS results for the critical exponents ν and x at QC2. The upper panel in (a) shows that the low-energy scale T^* vanishes close to the critical point as $|\alpha - \alpha_c|^\nu$ for a typical value of $s = 0.5$, while the dependency of ν on s is illustrated in the lower panel. Panel (b) displays x for different values of s , calculated via finite-size scaling (blue squares) and with the hyperscaling relation in Eq. (5.42) using VMPS results of β and ν (red crosses). All VMPS data corresponding to the lower panels in (a) can be found in Fig. C.9.

the previously encountered hyperscaling relation

$$x = (1 - 2\beta/\nu), \quad (5.42)$$

which should be valid in the regime $1/2 < s < 1$. Despite the logarithmic corrections around $s = 1/2$, the VMPS results shown in Fig. 5.16(b) indicate the validity of this hyperscaling relation, as they agree with the expected result for the temperature exponent given by $x = s$. For better comparison, we also determined x by analyzing the finite-size scaling of the magnetization at QC2 shown in Fig. 5.17, and find excellent agreement in the regime $1/2 < s < 1$. However, above the upper critical dimension of the SBM2, i.e. for $0 < s < 1/2$, the critical exponent x does not agree with its mean-field prediction $x = 1/2$ and follows $x = s$ instead. Analogous to the standard one-bath spin-boson model, this is caused by the massflow error (see discussion in Sec. 4.1.3).

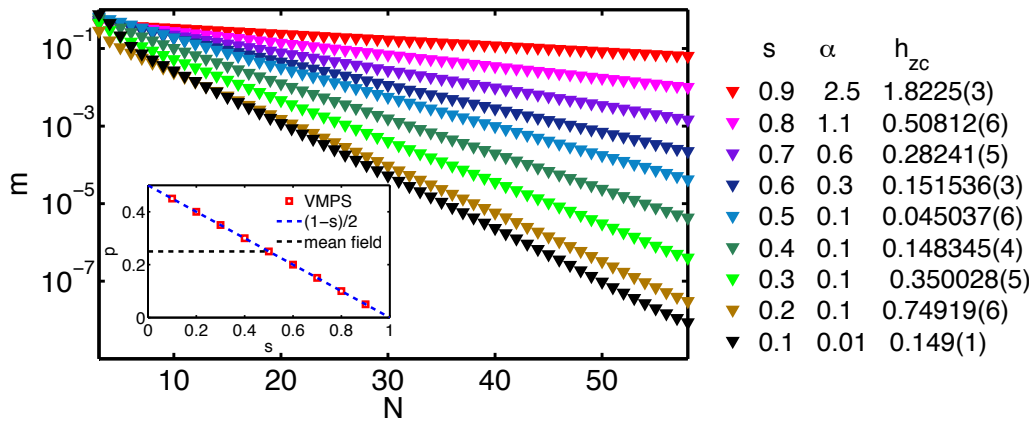


Figure 5.17: Finite-size scaling of the magnetization for various values of s at QC2. The inset shows the s -dependence of the exponent p which characterizes the vanishing magnetization at QC2. For all considered values of s we find that the exponent follows $p = (1 - s)/2$ with high accuracy. This is only in agreement with the RG predictions for $1/2 < s < 1$; for $0 < s < 1/2$ our results disagree with the expected mean-field result $p = 1/4$. Analogous to the standard spin-boson model this is caused by the massflow error, which inevitably plagues finite-size NRG calculations.

5.4 Asymmetric coupling

So far, we only considered an XY-symmetric SBM2 with both baths coupled symmetrically to the impurity, i.e. $\alpha_x = \alpha_y = \alpha$. As stated in the previous sections, the competition of the two baths gives rise to the critical phase at intermediate coupling only in such a situation. In other words, the underlying symmetry is essential for the stability of the critical phase according to RG arguments [21]. Introducing a small asymmetry in the bath couplings, $\Delta\alpha = |\alpha_x - \alpha_y|$, we can study the stability of the critical phase and examine whether the breaking of the XY-symmetry leads to a breakdown of the critical phase.

A first analysis of the magnetization $\langle\sigma_{x,y}\rangle$ in direction of the baths couplings for the localized and critical phase is shown in Fig. (5.18), where the coupling asymmetry $\Delta\alpha$ is tuned over a large interval. We observe a symmetric behavior of the magnetization, $\langle\sigma_x\rangle = \langle\sigma_y\rangle$, for very small $\Delta\alpha < 10^{-4}$. For this parameter spectrum, the stronger coupled bath is not yet able to dominantly influence the impurity spin. For larger coupling asymmetries the impurity spin delocalizes in direction of the weaker coupled bath (in x -direction) and strongly localizes in the direction of strong coupling. While the transition behaves smoother in the critical regime (Fig. 5.18(b)), it occurs rather abruptly in the localized phase (Fig. 5.18(a)). Note that the finite magnetization in the critical phase is due to finite-size effects discussed in Sec. 5.2.1.

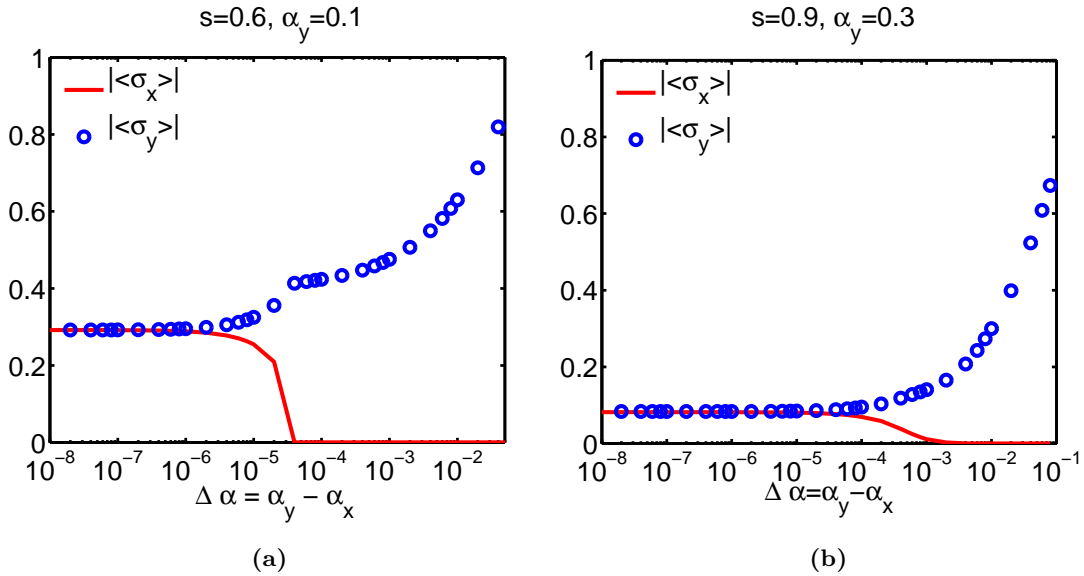


Figure 5.18: Magnetization $\langle\sigma_{x,y}\rangle$ for increasing coupling asymmetries $\Delta\alpha = \alpha_y - \alpha_x$ in both (a) localized and (b) critical phase [V1: $N = 50$, $D = 60$, $d_{opt} = 24$, $\Lambda = 2$].

In order to analyze the stability of the critical phase in more detail, it is useful to study the special properties of the critical phase with respect to an increasing coupling asymmetry $\Delta\alpha$. As discussed previously, the impurity spin shows a non-linear response to an external field in the critical phase, which is of power law character, such as

$$\langle\sigma_{x,y}\rangle \propto h_{x,y}^{1/\delta}, \quad \langle\sigma_z\rangle \propto h_z^{1/\delta'} \quad (5.43)$$

with $\delta, \delta' > 1$ characterized by the perturbative RG predictions in Eqs. (5.27) and (5.28). In the cross-over to the localized regime, we expect that the field response of the impurity spin becomes linear, i.e. $1/\delta' = 1$. Thus monitoring δ and δ' for increasing coupling asymmetries sheds light on the stability of the critical phase.

Figs. 5.19(a) and (b) show the response of the impurity spin to an external field inside the critical phase for different values of the coupling asymmetry $\Delta\alpha$ on a loglog scale. The results confirm our previous observations: for small asymmetry, we find δ and δ' in excellent agreement with the perturbative predictions indicating that the critical phase still exists. Towards larger coupling asymmetries, $\Delta\alpha > 10^{-3}$, the critical phase breaks down and crosses over into a y -localized regime. Hence, the response of the impurity spin in x - and z -direction becomes linear for small fields (e.g. $\delta' = \delta = 1$), while the magnetization localizes in y -direction thus showing no longer a power law response.

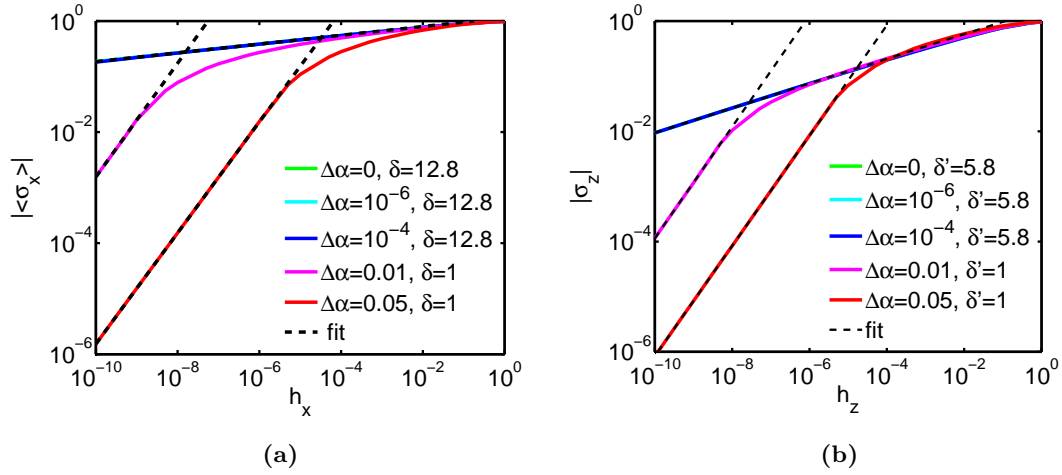


Figure 5.19: Non-linear response of the impurity spin to a magnetic field in (a) x - and (b) z -direction for different coupling asymmetries $\Delta\alpha$ and fixed s in the critical phase [V1: $N = 50$, $D = 60$, $d_{opt} = 24$, $\Lambda = 2$].

5.5 Comparison of methods: symmetry improved VMPS

We conclude this chapter by giving a short comparison of the numerical results obtained by the two different implementations of the VMPS procedure. As introduced above, we refer to the VMPS program without explicitly incorporated $U(1)$ symmetry as V1, while V2 denotes the symmetry conserving VMPS version.

In our experience both versions work equally well in the delocalized phase of the SBM2, where the non-degenerated ground state is very stable against numerical noise and thus hardly affected by artificial symmetry breaking in the numerics. On the other hand, the localized and particularly the critical phase suffer from $U(1)$ symmetry breaking in V1, which can be associated with the lifting of the ground state degeneracy.

Critical phase

Starting with the critical phase, this can be illustrated best by considering the energy-level flow diagrams obtained by the VMPS procedure. In Fig. 5.20 the rescaled energy flow of the SBM2 is displayed for a fixed value of s and α inside the critical phase calculated with V1 (a) and V2 (b) using the same choice of VMPS parameters (e.g bond dimension D , OBB dimension d_{opt} , chain length N). Although we observe that the two-fold ground state

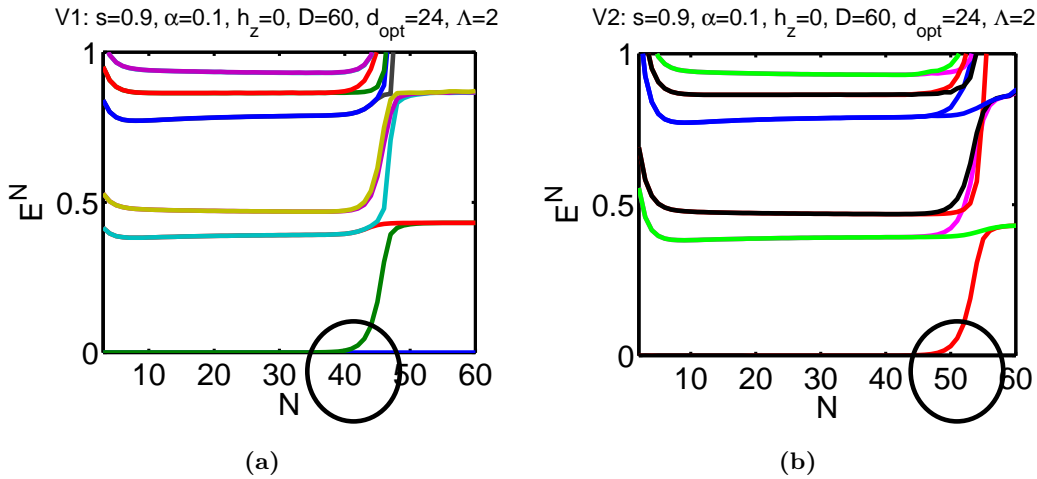


Figure 5.20: VMPS energy-level flow diagrams in the critical regime calculated with (a) V1 and (b) V2. The black circle highlights the lifting of the two-fold ground state degeneracy.

degeneracy is lifted when using both V1 and V2, the symmetry improved version V2 clearly conserves the degeneracy up to higher iterations $N_{split} \approx 50$ compared to $N_{split} \approx 40$ in V1. This indicates symmetry breaking is the reason for the lifting of the ground state degeneracy in V1. In the symmetry improved version, we are able to conserve it approximately up to the iteration that is associated with an energy scale slightly below numerical double precision, $T^* \sim \Lambda^{-N_{split}} < 10^{-16}$. For systems with longer chains, numerical noise at early iterations can influence results at late iterations strongly, which leads to a lifting of the ground state degeneracy despite exactly conserving the $U(1)$. These perturbations seem to play a crucial role within the critical regime while the other phases of the SBM2 are more stable against these numerical effects.

Employing the symmetry improved V2, we generally succeed in conserving the ground state degeneracy within the critical phase for all iterations N corresponding to a low-energy

scale $T \sim \Lambda^{-N}$ above machine precision. Choosing the discretization parameter $\Lambda = 2$, this indicates that we obtain numerically stable results for VMPS calculations with chain length $N < 50$. What's more, it seems the numerical perturbations play a less important role near the critical fixed point at α^* and close to QC1, the phase boundary between critical and localized regime. As Fig. 5.21 indicates, in those cases the degeneracy can be preserved for iterations beyond $N = 50$. To assess the implications of the lifted degeneracy on physical

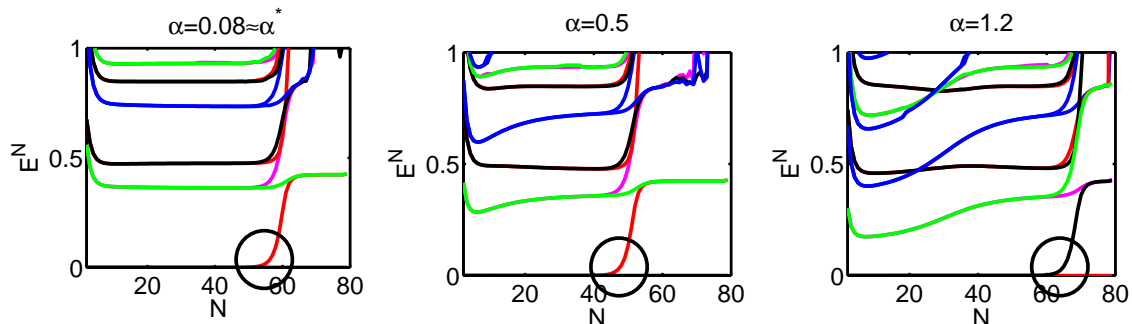


Figure 5.21: VMPS flow diagrams for fixed model parameter $s = 0.85$ and different values of α inside the critical phase. The ground state degeneracy is conserved for higher iterations $N_{split} > 50$ when α is close to the critical fixed point coupling $\alpha^* \approx 0.08$ and near the phase boundary at $\alpha_c \approx 1.29960$.

properties of the critical ground state, it is useful to study the finite-size scaling of the magnetization, which is expected to vanish in the limit of $N \rightarrow \infty$. Fig. 5.22 shows the finite-size behavior of the magnetization of the impurity spin for a fixed value of s and α inside the critical phase calculated with both V1 and V2. While both VMPS versions display the expected decay of m during the first $N \approx 40$ iterations, the magnetization saturates at a constant value of m for later sites when employing V1. In contrast, V2 is able to preserve the exponential decay for approximately 10 more iterations. This strongly resembles the behavior of the corresponding energy flow discussed above, implying that the lifting of the ground state degeneracy leads to artificial effects in physical observables such as the magnetization.

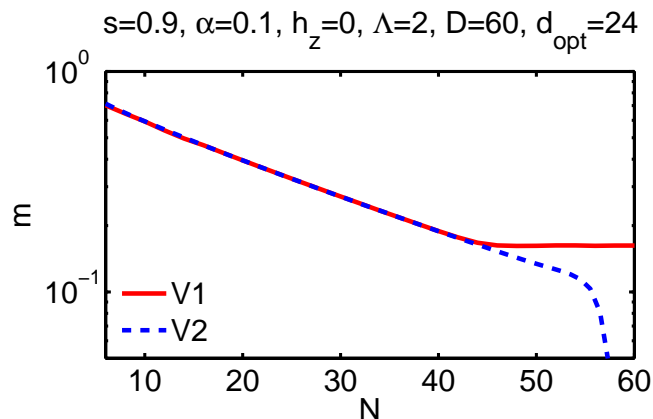


Figure 5.22: Finite size scaling of the magnetization in the critical phase calculated with V1 (red solid line) and V2 (blue dashed line).

Localized phase

Numerical effects associated with $U(1)$ symmetry breaking are also found in the localized phase of the SBM2, where the ground state is two-fold degenerate as well. As discussed

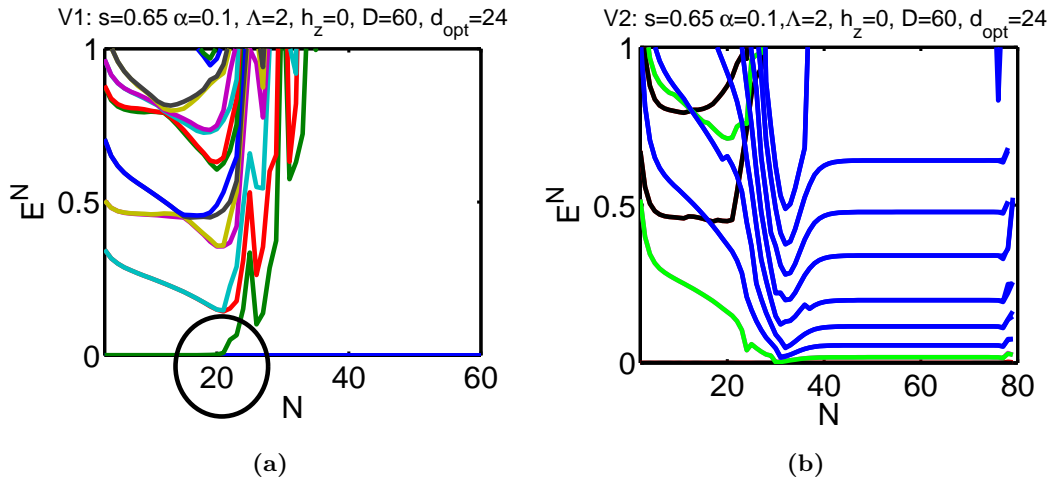


Figure 5.23: VMPS energy-level flow diagrams for fixed $s = 0.65$ and $\alpha = 0.1$ in the localized regime calculated with (a) V1 and (b) V2. Using the latter, we succeed in conserving the ground state degeneracy for all iterations.

above, we can connect the $U(1)$ symmetry breaking with the lifting of the ground state degeneracy. The flow diagrams in Fig. 5.23 display this effect very clearly: employing V1 the degeneracy is only conserved for few iterations with $N_{split} \approx 20$. On the other hand when using V2, the ground state degeneracy is conserved for all iterations, and even for sites ≥ 50 where the corresponding energy scale reaches values below the order of numerical double precision. Thus the symmetry improved VMPS procedure V2 drastically improves the stability of the numerical results in localized phase. In contrast to the critical regime, where numerical perturbations affect the calculations with long chains despite the exactly incorporated $U(1)$ symmetry, numerical noise at early iterations does not influence the results at late iterations in the localized phase.

These observations are also reflected in the finite-size scaling of the magnetization inside the localized regime as displayed in Fig. 5.24(a). Using V1, the magnetization m decays exponentially for very small systems m , and then after reaching a constant value shows a jump around iteration $N = 25$. That this effect occurs in correspondence with the lifting of the ground state degeneracy in Fig. 5.23 can be understood as signature of the breaking of $U(1)$ symmetry in the SBM2. When employing the symmetry improved version V2, the jump vanishes completely and m remains almost constant for larger systems. The slight decay of m for iterations $N > 30$ can be explained by the diverging bosonic numbers on the chain in the localized regime, that reach the cap around site 30 as indicated in Fig. 5.24(b). Nevertheless, it is possible to extract the physically correct value of m in the SBM2 for $1/2 < s < 1$ (for detail see App. C.2).

Thus the symmetry implementation V2 is not only relevant to obtain qualitatively clean energy-flow diagrams, which allow a fixed point analysis and the determination of the correlation length exponent ν . Moreover, the correct description of the phase transition QC1 and QC2 for $1/2 < s < 1$ requires the symmetry improved VMPS procedure. Particularly for large values of $s \leq 1$, the critical behavior of the SBM2 at both QC1 and QC2 is governed by a diverging exponent ν , requiring exponentially growing chain lengths (see Sec. 5.2.2).

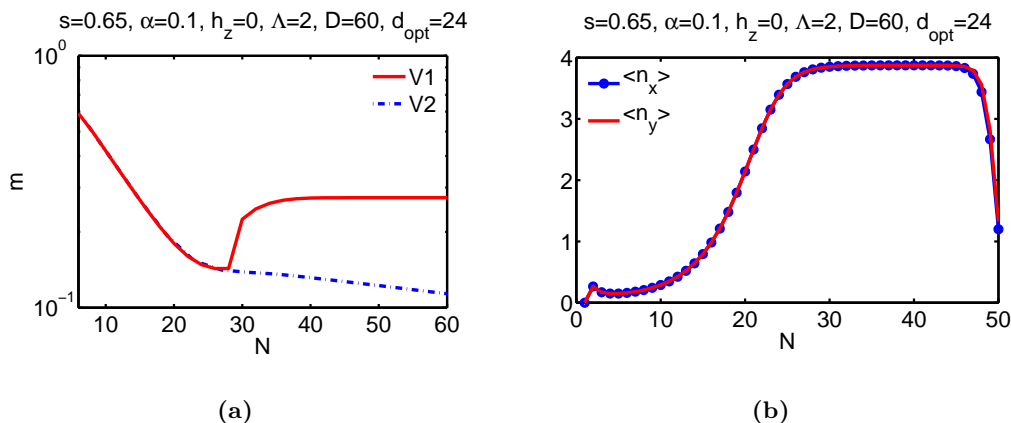


Figure 5.24: (a) Finite size scaling of the magnetization in the critical phase calculated with V1 (red solid line) and V2 (blue dashed line) and the corresponding bosonic occupation numbers on the Wilson chain.

Only V2 is able to systematically access the critical phenomena of the SBM2 in this regime due to shorter calculation times and drastically improved numerical accuracy. Using V1 not only limits the chain length to $N \leq 80$ (already requiring a run time of 2 days or more for each data point), it also suffers from systematic convergence problems near the phase boundaries, as displayed in Fig. 5.25. Here, the magnetization of the system is plotted at the transition from the localized to the delocalized phase for $s = 0.9$. The VMPS results of V1 in Fig. 5.25(a) are clearly distorted while V2 in (b) resolves the physical properties of the system for the same set of VMPS parameters correctly.

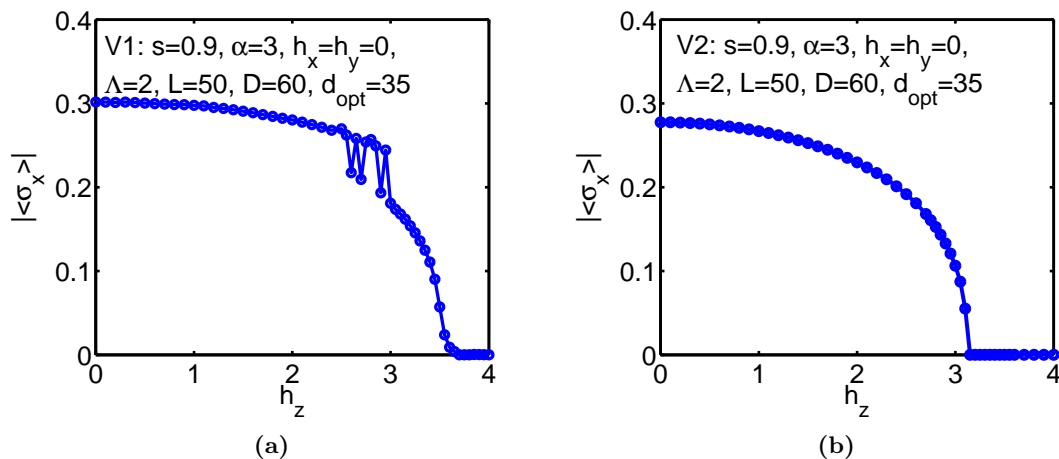


Figure 5.25: Vanishing magnetization at the transition between localized and delocalized phase calculated with (a) V1 and (b) V2 for fixed $s = 0.9$, $\alpha = 3$ and identical VMPS parameters. We observe drastic numerical problems in (a) not allowing a correct description of the physical properties near the phase transition. On the other hand, the symmetry improved VMPS procedure in (b) leads to well-converged results.

6. Conclusion

Since the introduction of the spin-boson model in the 1980s [6, 4], bosonic quantum impurity models have been successfully applied in various contexts from quantum information to biological systems and helped gaining profound insights in the physical properties of open quantum systems [4, 5]. Due to the presence of interaction, however, the full quantum-many-body state space must be explored. As a consequence, these models involve a high degree of complexity so that only few analytic approaches are able to assess and describe the underlying physics. Particularly the study of critical phenomena requires powerful numerical first-principle methods, that are able to deal with the specific difficulties arising from the bosonic nature of the model.

This thesis is motivated by the recent work of Guo et al. [21], who presented a variational matrix product state approach based on a hybrid of NRG and DMRG, which is capable to study bosonic quantum impurity models with high accuracy across the entire phase diagram. By employing an extended version of their VMPS method, the thesis pursued two objectives: (i) to revise the critical and dynamical properties of the standard spin-boson model, and (ii) to fully characterize the critical phenomena of a generalized two-bath spin-boson model.

After introductory remarks on the physics of critical phenomena and quantum criticality (Chap. 2), the relevant numerical methods – MPS, NRG and VMPS – were presented, including a discussion on the implementation of symmetries and time-dependence, the latter based on adaptive time-dependent DMRG (Chap. 3).

Starting with the one-bath version of the spin-boson model (Chap. 4), the numerical results for the critical properties of the system were found to be in agreement with the predictions of quantum-to-classical correspondence. Moreover, it was demonstrated how to access additional critical exponents within the VMPS formalism. Employing time-dependent VMPS, the simulation of the non-equilibrium dynamics successfully reproduced NIBA results in the weak-coupling regime of the ohmic SBM, as well as the characteristic transition from damped oscillations to incoherent decay observed for sub-ohmic dissipation.

The application of VMPS to the XY -symmetric two-bath spin-boson model revealed details of the rich ground state phase diagram, that consists of three distinct phases – a delocalized, localized and critical regime – and exhibits two independent quantum phase transitions at zero temperature (Chap. 5). The extensive numerical study of critical points allowed a detailed characterization of the critical properties of the SBM2. We confirmed that the transition between localized and delocalized regime is equivalent to the thermal transition in a classical XY -symmetric spin chain with long-range interactions, following mean-field predictions for $0 < s < 1/2$ and hyperscaling for $1/2 < s < 1$. In addition, our calculations indicate that the exponents describing the quantum critical point between localized and critical phase obey hyperscaling as well. By successful application of VMPS to the two-bath spin-boson model, we were thus able to determine the critical phenomena of this model for a wide range of parameters, which so far had been an open problem.

Possible topics for future research include the application of VMPS to other quantum

impurity models such as the Bose-Fermi Kondo model, where bosonic NRG results suggested the breakdown of quantum-to-classical correspondence [18]. Analogous to the spin-boson model, the validity of these results is may be compromised, since the bosonic NRG procedure did not properly account for the truncated local bosonic basis sets. The VMPS procedure should be able to reveal the correct critical properties of this model. Furthermore, it would be interesting to study models with two or more interacting spins located at the impurity, relevant in various applications in the context of noisy qubits [110]. While we have already carried out preliminary studies on a two-spin version of the one-bath SBM [111], a generalized two-baths version might contain exciting new critical phenomena.

Appendices

Appendix A

A.1 Two-site VMPS with optimal bosonic basis

It is often more effective to employ one-site VMPS optimization for bosonic models, since the large local basis sets make a two-site update numerically expensive. Nevertheless, the presence of symmetries or the need for a dynamic Hilbert space truncation may require the implementation of a two-site update. There exists no literature on this topic for an MPS with optimal bosonic basis, nevertheless the details of the procedure are very similar.

Consider an MPS with OBB structure of general form,

$$|\psi\rangle = \sum_{\sigma=\uparrow\downarrow} \sum_{n_1 \dots n_N} A^{[\sigma]} A^{[n_1]} A^{[n_2]} \dots A^{[n_N]} |\sigma\rangle |n_1\rangle |n_2\rangle \dots |n_N\rangle \quad (\text{A.1})$$

where the form of $A^{[n_k]}$ is given by

$$A_{l_k, m}^{[n_k]} = \sum_{\tilde{n}_k=0}^{d_{opt}^k-1} \tilde{A}_{l_k, r_k}^{[\tilde{n}_k]} V_{\tilde{n}_k, n_k}, \quad (\text{A.2})$$

We again emphasize that here the sum over \tilde{n}_k is not carried out explicitly, i.e. the tensors \tilde{A} and V are kept separate. Nevertheless, the two-site update can be adapted to the two blocks \tilde{A} and V to dynamically adjust not only the bond dimensions D^k but also the OBB dimensions d_{opt}^k . This requires an additional optimization step compared to the standard two-site update without OBB.

1. We start in the local picture with current site k for given state $|\psi\rangle$,

$$|\psi\rangle = \sum_{l_k r_k n_k} \sum_{\tilde{n}_k}^{d_{opt}^k-1} \tilde{A}_{l_k, r_k}^{[\tilde{n}_k]} V_{\tilde{n}_k, n_k} |l_k\rangle |n_k\rangle |r_k\rangle, \quad (\text{A.3})$$

where $|l_k\rangle |n_k\rangle |r_k\rangle$ are the effective orthonormal basis sets of the left, local and right state space, respectively. We set $\tilde{A}_{l_k, r_k, \tilde{n}_k} \equiv \tilde{A}_{l_k, r_k}^{[\tilde{n}_k]}$ and now carry out the sum over \tilde{n}_k explicitly

$$B_{l_k, r_k, n_k} = \sum_{\tilde{n}_k}^{d_{opt}^k} \tilde{A}_{l_k, r_k, \tilde{n}_k} V_{\tilde{n}_k, n_k}. \quad (\text{A.4})$$

After transforming the Hamiltonian and operators into the effective $|l_k\rangle |n_k\rangle |r_k\rangle$ basis, we optimize the B -matrix using standard VMPS procedure of Sec. 3.3.1.

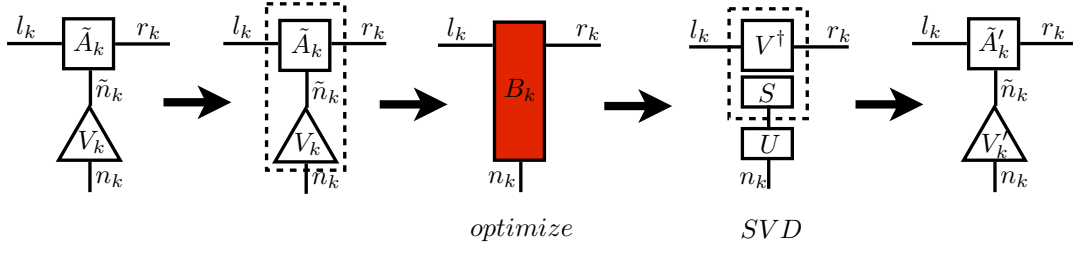


Figure A.1: Steps 1 and 2 of the two-site update procedure when sweeping from left to right. The indices connecting the matrices surrounded by the dashed lines are contracted. The red filled square is the subject of the VMPS optimization.

2. To restore the original OBB structure, we perform a SVD on the updated B'

$$\begin{aligned}
 B'_{l_k, r_k, n_k} &= B'_{(l_k r_k), n_k} \stackrel{SVD}{=} \sum_{m, n=0}^{d_{k-1}^k} U_{(l_k r_k), m} S_m V_{m, n_k}^\dagger \\
 &\stackrel{truncate}{\approx} \sum_{m, n=0}^{d_{opt}^k - 1} U_{(l_k r_k), m} S_m V_{m, n_k}^\dagger \\
 &= \sum_{m=0}^{d_{opt}^k - 1} U_{l_k, r_k, m} (S V^\dagger)_{m, n_k} \\
 &= \sum_{m=0}^{d_{opt}^k - 1} \tilde{A}'_{l_k, r_k, m} V'_{m, n_k}. \tag{A.5}
 \end{aligned}$$

The SVD is carried out exactly with respect to the local index n_k . In the following truncation step, we only keep the d_{opt}^k largest instead of all singular values in S . In contrast to the one-site update this allows to adapt d_{opt}^k easily.

3. Now we are ready to perform the two-site optimization by shifting to a local setting of sites k and $k+1$,

$$|\psi\rangle = \sum_{l_k, r_{k+1}, \tilde{n}_k, \tilde{n}_{k+1}} \sum_m^{D^k} \tilde{A}_{l_k, m, \tilde{n}_k}^k \tilde{A}_{m, r_{k+1}, \tilde{n}_{k+1}}^{k+1} |l_k\rangle |\tilde{n}_k\rangle |\tilde{n}_{k+1}\rangle |r_{k+1}\rangle, \tag{A.6}$$

where we assume site k to have an orthonormal left basis and site $k+1$ to have an orthonormal right basis. To calculate the update it is most convenient and also most efficient in practice to change to an expanded left and right basis [112, 113, 54],

$$|l_c\rangle = \mathbb{I}_{l_k, l_c}^{[\tilde{n}_k]} |l_k\rangle |\tilde{n}_k\rangle = \delta_{(l_k n_k), l_c} |l_k\rangle |\tilde{n}_k\rangle \tag{A.7}$$

$$|r_c\rangle = \mathbb{I}_{r_c, r_{k+1}}^{[\tilde{n}_{k+1}]} |\tilde{n}_{k+1}\rangle |r_{k+1}\rangle = \delta_{r_c, (n_{k+1} r_{k+1})} |\tilde{n}_{k+1}\rangle |r_{k+1}\rangle, \tag{A.8}$$

where the two A -matrices are merged into the center matrix

$$C_{l_c, r_c} = \sum_m \tilde{A}_{l_c = (l_k \tilde{n}_k), m}^k \tilde{A}_{m, r_c = (\tilde{n}_{k+1} r_{k+1})}^{k+1}. \tag{A.9}$$

Transforming the Hamiltonian into the effective basis $|l_c\rangle |r_c\rangle$, the optimization of the matrix C is carried out.

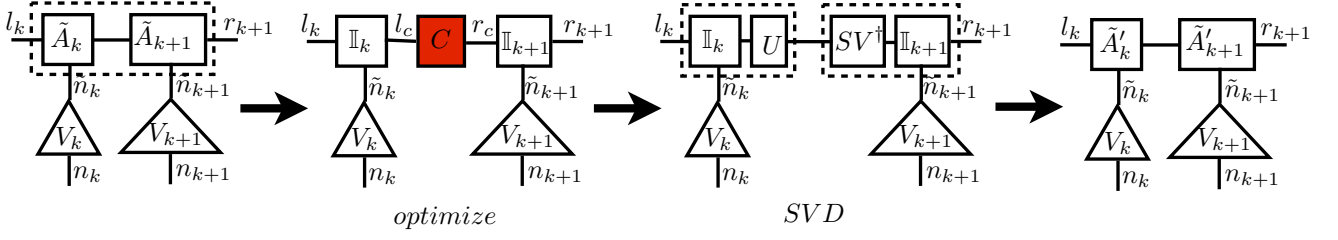


Figure A.2: Steps 3 and 4 of the two-site update procedure when sweeping from left to right. The indices connecting the matrices surrounded by the dashed lines are contracted. The red filled square is the subject of the VMPS optimization.

4. In the final step, we switch into the local picture with current site $k + 1$ to terminate the two-site optimization of sites k and $k + 1$.

$$\begin{aligned}
\mathbb{I}[\tilde{n}_k] C \mathbb{I}[\tilde{n}_{k+1}] &\stackrel{SVD}{=} \sum_{l_c r_c} \sum_{m, n=1}^{D^k d_{opt}^k} \delta_{(l_k \tilde{n}_k), l_c} U_{l_c, m} s_m V_{m, r_c}^\dagger \delta_{r_c, (\tilde{n}_{k+1} r_{k+1})} \\
&\stackrel{truncate}{\approx} \sum_{m, n=1}^{D^k} U_{(l_k \tilde{n}_k), m} s_m V_{m, (\tilde{n}_{k+1} r_{k+1})}^\dagger \\
&= \sum_{m=1}^{D^k} U_{l_k, \tilde{n}_k, m} (S V^\dagger)_{m, \tilde{n}_{k+1}, r_{k+1}} \\
&= \sum_{m=1}^{D^k} \tilde{A}'_{l_k, m, \tilde{n}_k} \tilde{A}'_{m, r_{k+1}}^{k+1} \tag{A.10}
\end{aligned}$$

Again, we calculate the exact SVD of the matrix C , then truncate from $D^k d_{opt}^k$ states back to D^k states by keeping only the largest singular values. D^k can be adapted freely and for example chosen such that we keep all singular values bigger than some threshold.

The state is now described in the local picture of site $k + 1$

$$|\psi\rangle = \sum_{l_{k+1} r_{k+1} n_{k+1}} \sum_{\tilde{n}_{k+1}}^{d_{opt}^{k+1}-1} \tilde{A}'_{l_{k+1}, r_{k+1}}^{[\tilde{n}_{k+1}]} V_{\tilde{n}_{k+1}, n_{k+1}} |l_{k+1}\rangle |n_{k+1}\rangle |r_{k+1}\rangle, \tag{A.11}$$

where we start over the two-site update by repeating steps 1-4 for site $k + 1$ and $k + 2$.

Appendix B

B.1 SBM1: critical exponents

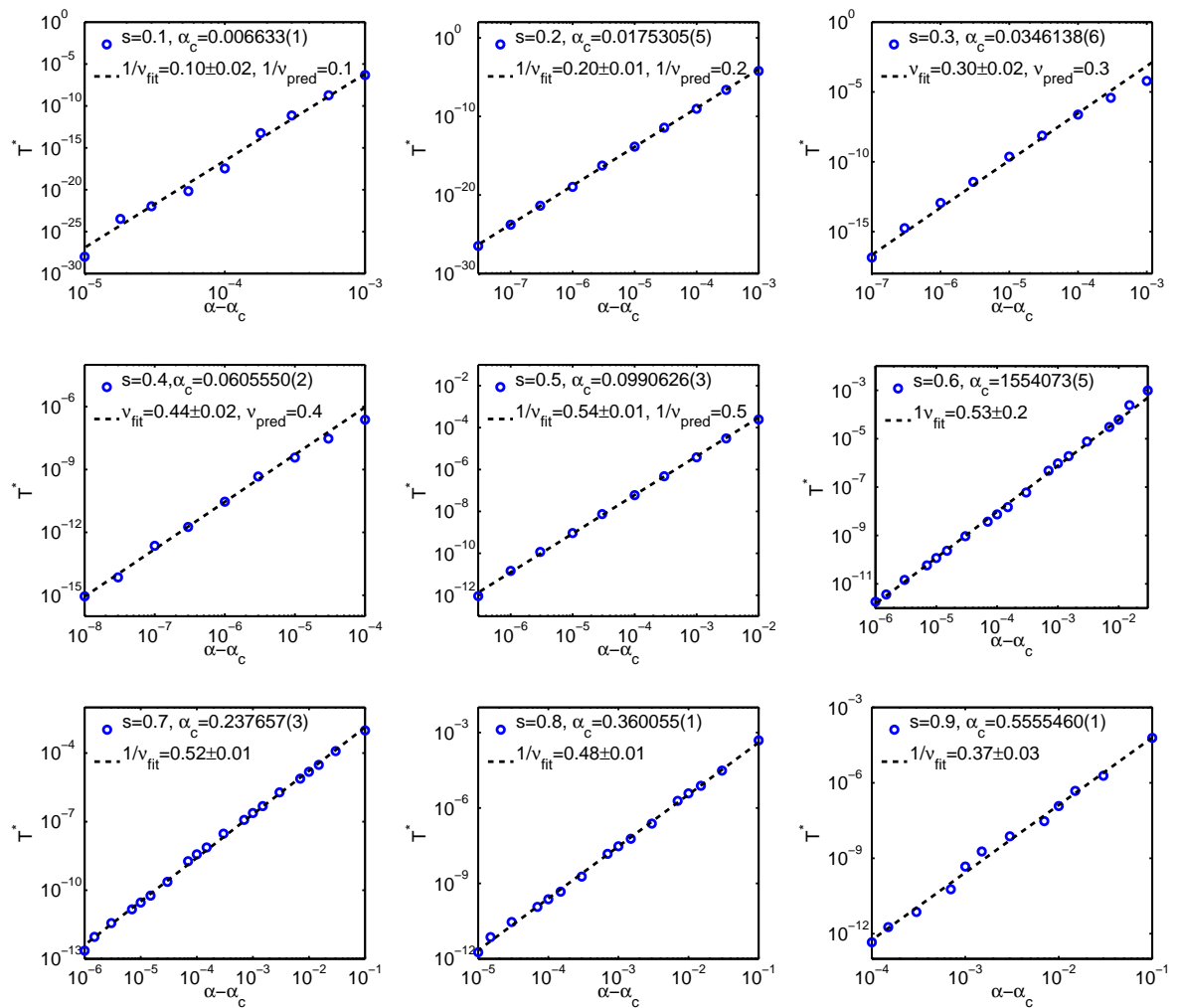


Figure B.1: Critical exponent ν extracted from $T^* \sim (\alpha - \alpha_c)^{1/\nu}$ for different s at the QPC of the SBM. In all calculations we used the parity code $[N = 100, D = 40, d_{\text{opt}} = 16, \Lambda = 2]$.

Appendix C

C.1 SBM2: Calculation of the magnetization in the $U(1)$ symmetry code

The ground state of the SBM2 in the localized and critical phase is twofold degenerate. A VMPS run breaks the degeneracy at the end of the Wilson chain and chooses one of the two physical states as numerical ground state. In case of an exact $U(1)$ symmetry implementation, we can attach a well defined symmetry label to the numerical ground state ($q = 0 \vee q = 1$).

Let us consider the magnetization in x - and y -direction in the ground state. The diagonal matrix elements vanish per definition,

$$m_x = \langle \psi^{q'} | \sigma_x^{imp} | \psi^q \rangle = 0 \quad \text{for } q = q' \quad (\text{C.1})$$

$$m_y = \langle \psi^{q'} | \sigma_y^{imp} | \psi^q \rangle = 0 \quad \text{for } q = q'. \quad (\text{C.2})$$

When not enforcing the $U(1)$ symmetry the final ground state of a VMPS calculation is always the symmetry broken, with maximized $m_{i=x,y}$. To reconstruct the magnetization of this 'original' ground state, we have to calculate the non-diagonal matrix elements of the magnetization. In general there are two ways to do that:

1. We calculate in two separate VMPS runs $|\psi^{q=1}\rangle$ and $|\psi^{q=0}\rangle$. Then we determine the matrix elements $\langle \psi^{q=1} | \sigma_i^{imp} | \psi^{q=0} \rangle$ with an explicit calculation. From a numerical point of view this is expensive - for each data point and each chain length N we have to carry out two VMPS runs.
2. We use only one VMPS run to determine either $|\psi^{q=1}\rangle$ or $|\psi^{q=0}\rangle$ and use the following method to determine the magnetization of a system with arbitrary Wilson chain length $0 < n < N$:

- ground state is brought into left-canonical form:

$$|\psi^q\rangle_N = \sum_{n_1 \dots n_N} A^{[n_1]} A^{[n_2]} \dots A^{[n_N]} |n_1, n_2, \dots, n_N\rangle \quad (\text{C.3})$$

- projection into 2D hilbert space of ground state: we project the state into the effective eigenbasis of the hamiltonian \hat{H}^n ($0 < n < N$) and only keep the two states of lowest energy.¹ Using NRG notation the lowest lying eigenstates of \hat{H}^n can be written as

$$|s\rangle_n = \sum_{n_1 \dots n_n} (A^{[n_1]} A^{[n_2]} \dots A^{[n_n]})_s |n_1, n_2, \dots, n_n\rangle \quad s \in \{0, 1\} \quad (\text{C.4})$$

¹As seen in the flowdiagrams in Figure (2) the two lowest lying energy states stay the same for all systems $n < N$ (e.g. no line crossing)

- next we calculate all matrix elements $(M_i)_{ss'}^{[n]} \equiv {}_n \langle s | \sigma_i^{imp} | s' \rangle_n$ of the magnetization, where one of the matrix elements is given by

$$(M_i)_{ss'}^{[n]} = \left(\sum_{n_n} \tilde{A}'^{[n_n] \dagger} \left(\dots \left(\sum_{n_2} A'^{[n_2] \dagger} \left(\sum_{n_1} A'^{[n_1] \dagger} \sigma_i^{imp} A^{[n_1]} \right) A^{[n_2]} \right) \dots \right) A^{[n_n]} \right)_{ss'} \quad (\text{C.5})$$

- The eigenvalues of the 2×2 matrix $M_i^{[n]}$ give the two possible values of the magnetization of the system with chain length n in the ground state $\langle \sigma_i^{imp} \rangle = \pm m_i$ (therefore the plain thermal average *without spontaneous symmetry breaking* would result in zero magnetization).

A direct comparison of the two different methods to calculate m is shown in Fig. C.1 for the example of a finite size scaling. In general, we observe excellent agreement between both results. Therefore the second (numerically cheaper) method of determining m in the symmetry code of the SBM2 leads to reliable results.

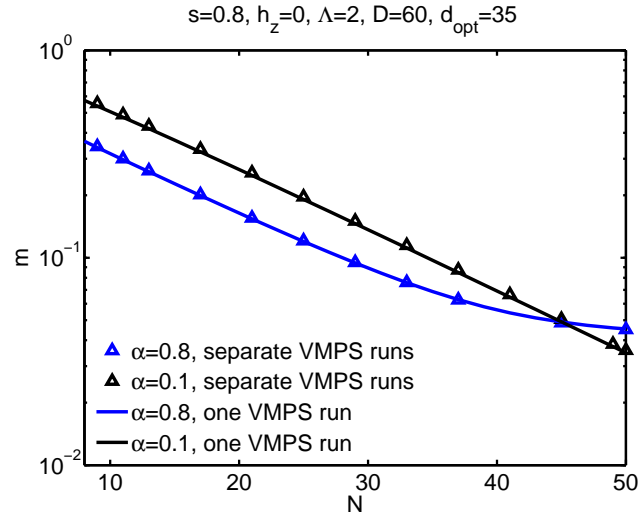


Figure C.1: Finite-size scaling of the magnetization in the localized (blue lines) and in the critical (black lines) regime. For the triangles we carried out different VMPS runs for each data point, while for the solid lines we used an NRG based approximation explained in the main text.

C.2 SBM2: Influence of diverging bosonic basis on QC1 and QC2

Since the incorporation of the bosonic shift into the symmetry improved VMPS version V1 is still an open task, the question arises to what extent the diverging bosonic basis influences the results for critical exponents (especially β) at QC1 and at QC2 for $1/2 < s < 1$.

A similar analysis has already been carried out in [89] for the NRG application to the one-channel spin-boson model. The bosonic truncation error should not spoil $\langle \sigma_x^{imp} \rangle$, if the magnetization saturates at an NRG iteration where the bosonic occupation number $\langle n_x \rangle$ is not yet affected by the Hilbert space truncation, i.e. the occupation number has not reached its maximum value yet. This condition is satisfied for $0.5 < s < 1$ for the SBM1 and explains why critical exponents obtained by NRG agree with VMPS/QMC results in this regime. On the other hand, the magnetization and the bosonic occupation number saturate at the same iterations for $0 < s < 0.5$, indicating that the truncation error affects the value of $\langle \sigma_x^{imp} \rangle$.

We extend this analysis to SBM2 treated by a VMPS procedure with incorporated $U(1)$ symmetry. In Figs. C.2(a) and (b) $\langle \sigma_x^{imp} \rangle$ and $\langle n_x \rangle$ are shown for two values near QC2 in the localized regime for $0.5 < s < 1$. We see clearly that the magnetization saturates before $\langle n_x \rangle$ reaches the plateau. Transferring the argument of [89] from NRG to VMPS, this indicates that the a bosonic shift is not absolutely necessary to obtain correct results. Nevertheless, $\langle \sigma_x^{imp} \rangle$ further decreases after the bosonic occupation number has reached its maximum value, which we identify as an effect of the bosonic state space truncation in the VMPS procedure. To circumvent this systematic error, we extract $\langle \sigma_x^{imp} \rangle$ not at the end of the chain but chose an iteration right before $\langle n_x \rangle$ saturates as indicated by the red lines. For QC1 the situation is similar as shown in Fig. C.2(c).

In Fig. C.3 the influence of the truncation error on the critical exponent β is shown for a typical value of s at QC1. Extracting $\langle \sigma_x^{imp} \rangle$ at the end of the chain reduces β significantly compared to its 'correct' value.

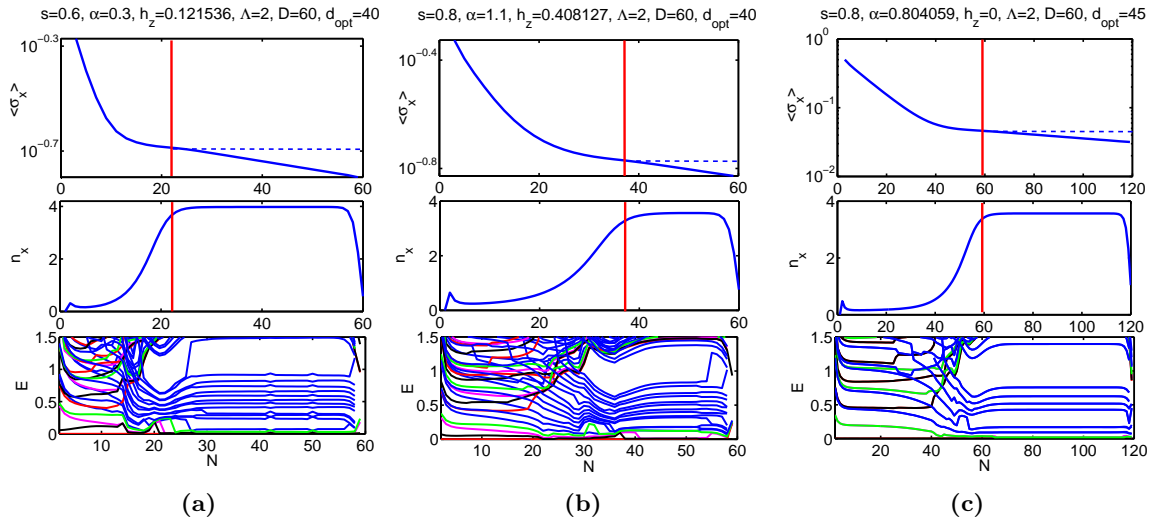


Figure C.2: $\langle \sigma_x^{imp} \rangle$, $\langle n_x \rangle$ and flow diagrams for typical points in the localized regime close to QC2 (a,b) and QC1 (c). The bosonic state space truncation results in an unnatural decrease of the magnetization for iterations where $\langle n_x \rangle$ has already reached its maximum value. The red bar indicates the 'correct' choice of $\langle \sigma_x^{imp} \rangle$.

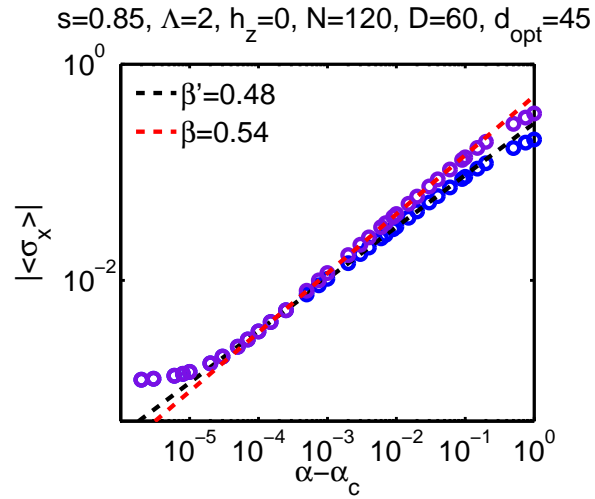


Figure C.3: Calculation of the critical exponent β at QC1. If we extract $\langle \sigma_x^{imp} \rangle$ at the end of the chain (blue dots), we systematically include an error due to bosonic state space truncation leading to a lower value β' . The purple dots display $\langle \sigma_x^{imp} \rangle$ calculated according to the text - extracting $\langle \sigma_x^{imp} \rangle$ at an iteration right before $\langle n_x \rangle$ saturates. This yields to a value of β in accordance with hyperscaling relations.

C.3 SBM2: Critical exponents

C.3.1 ν at QC1

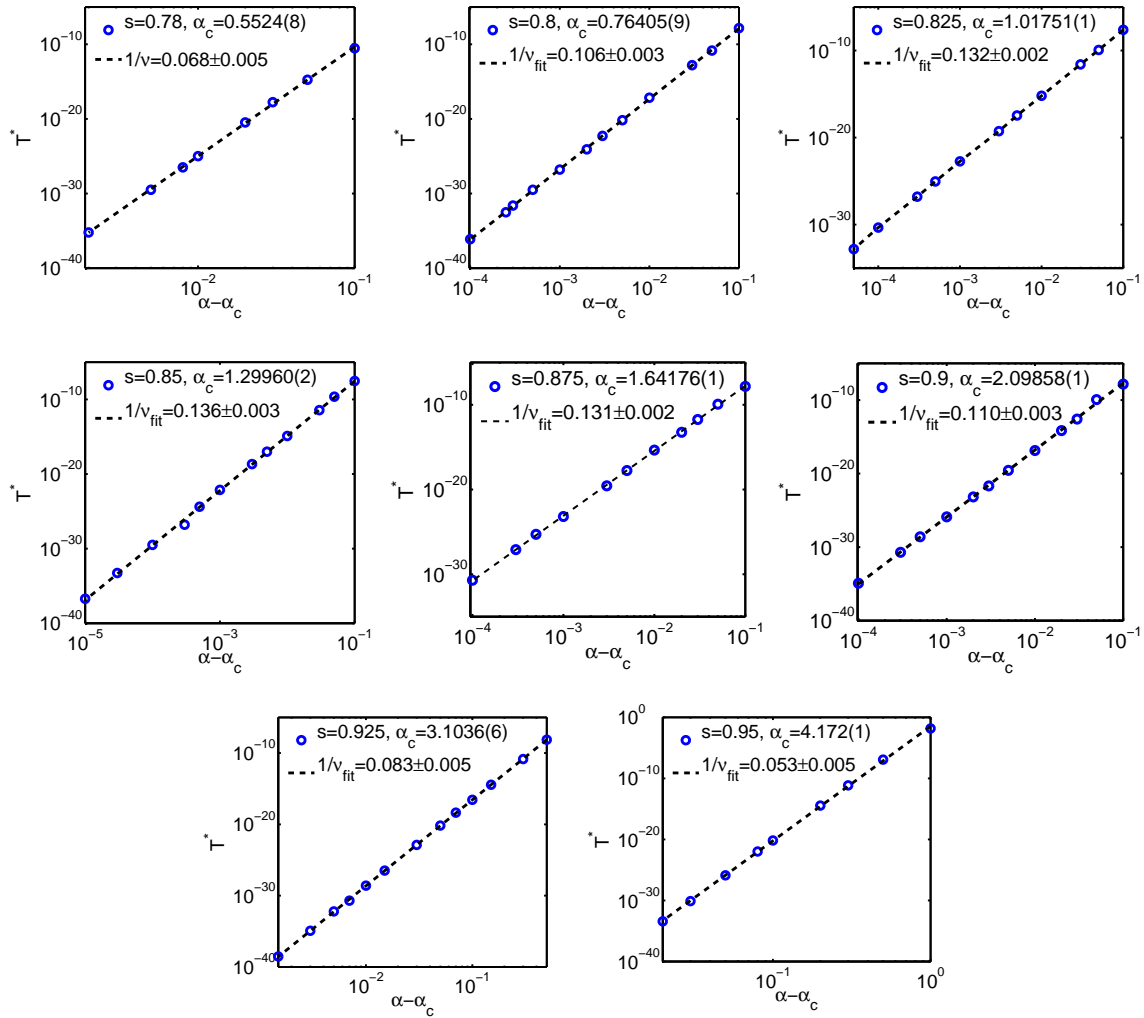


Figure C.4: Critical exponent ν for different values s at QC1 [V2: $N = 120$, $D = 60$, $d_{\text{opt}} = 40$, $\Lambda = 2$].

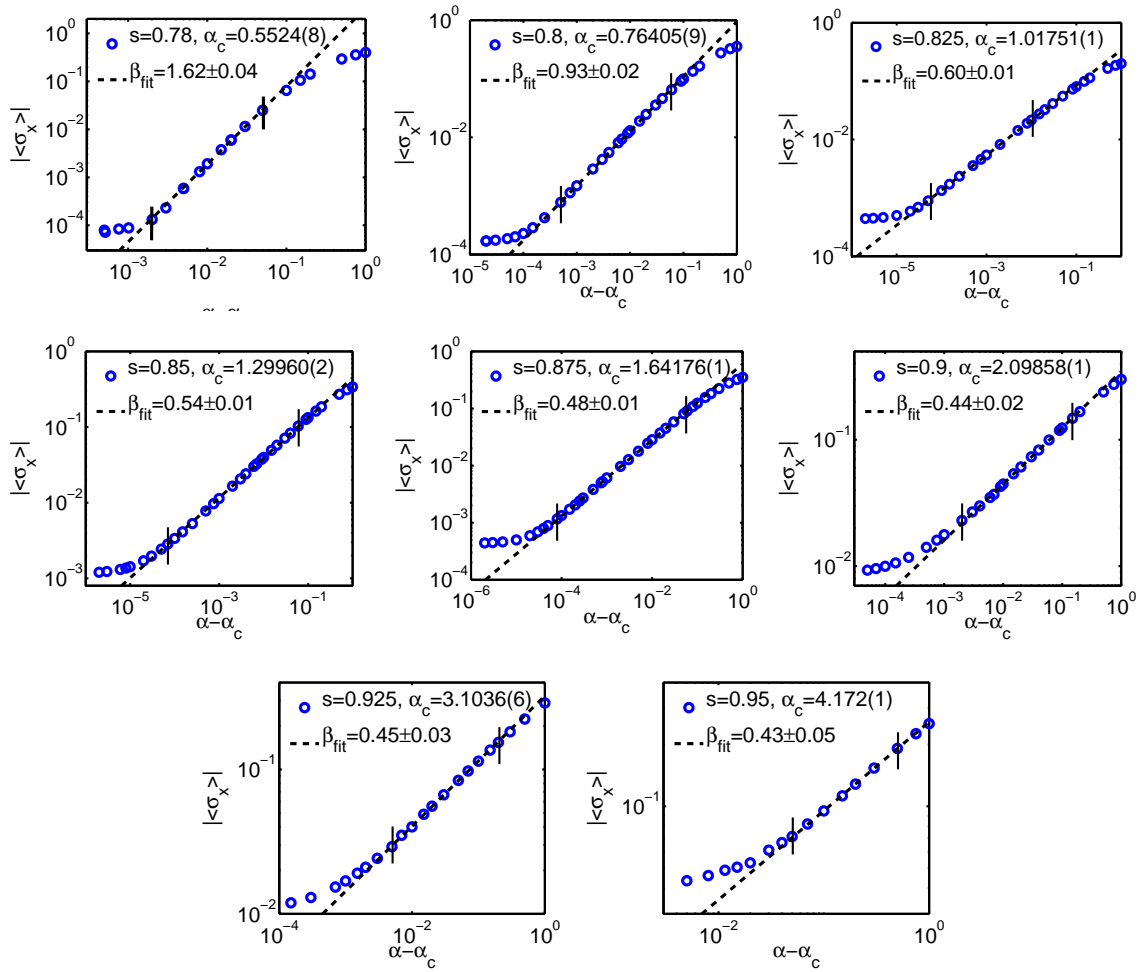
C.3.2 β at QC1

Figure C.5: Critical exponent β for different values s at QC1 [V2: $D = 60$, $d_{opt} = 40$, $\Lambda = 2$, $N = 120$ ($s < 0.9$), $N = 150$ ($s \geq 0.9$)]. The error bars correspond to the two extremal values of the exponent obtained by using only the upper or lower half of the full fitting interval that is indicated by vertical marks.

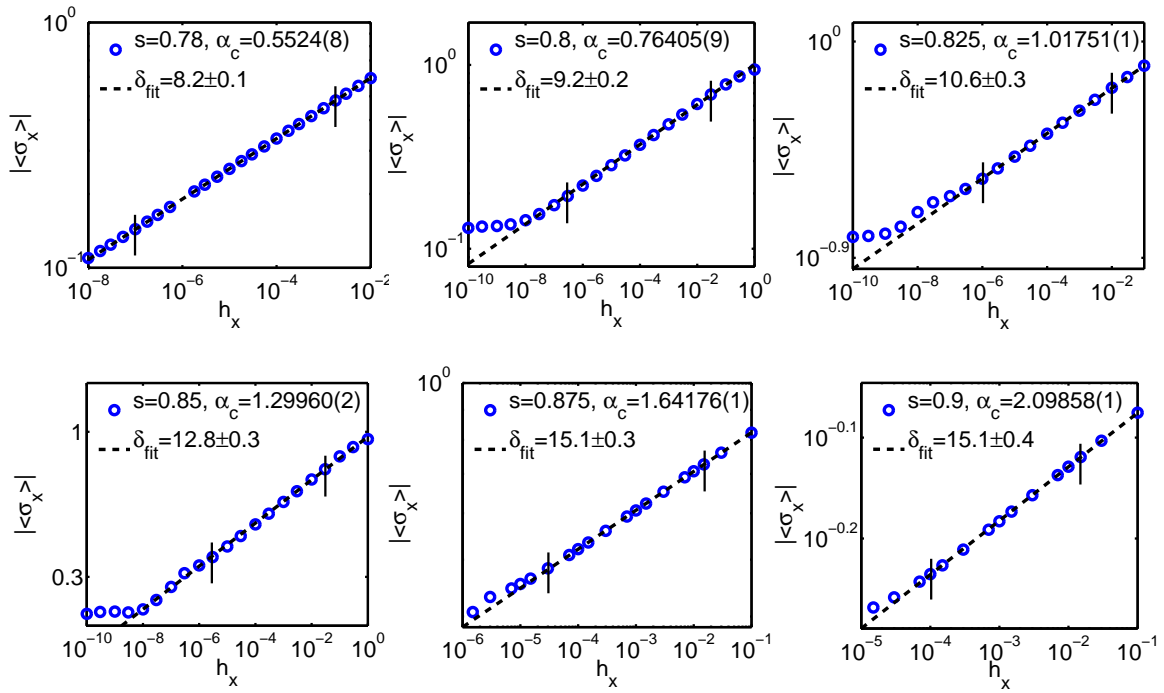
C.3.3 δ at QC1

Figure C.6: Critical exponent δ for different values of s at QC1, where the vertical lines indicate the fitting range [V1: $N = 60$, $D = 60$, $d_{\text{opt}} = 24$, $\Lambda = 2$].

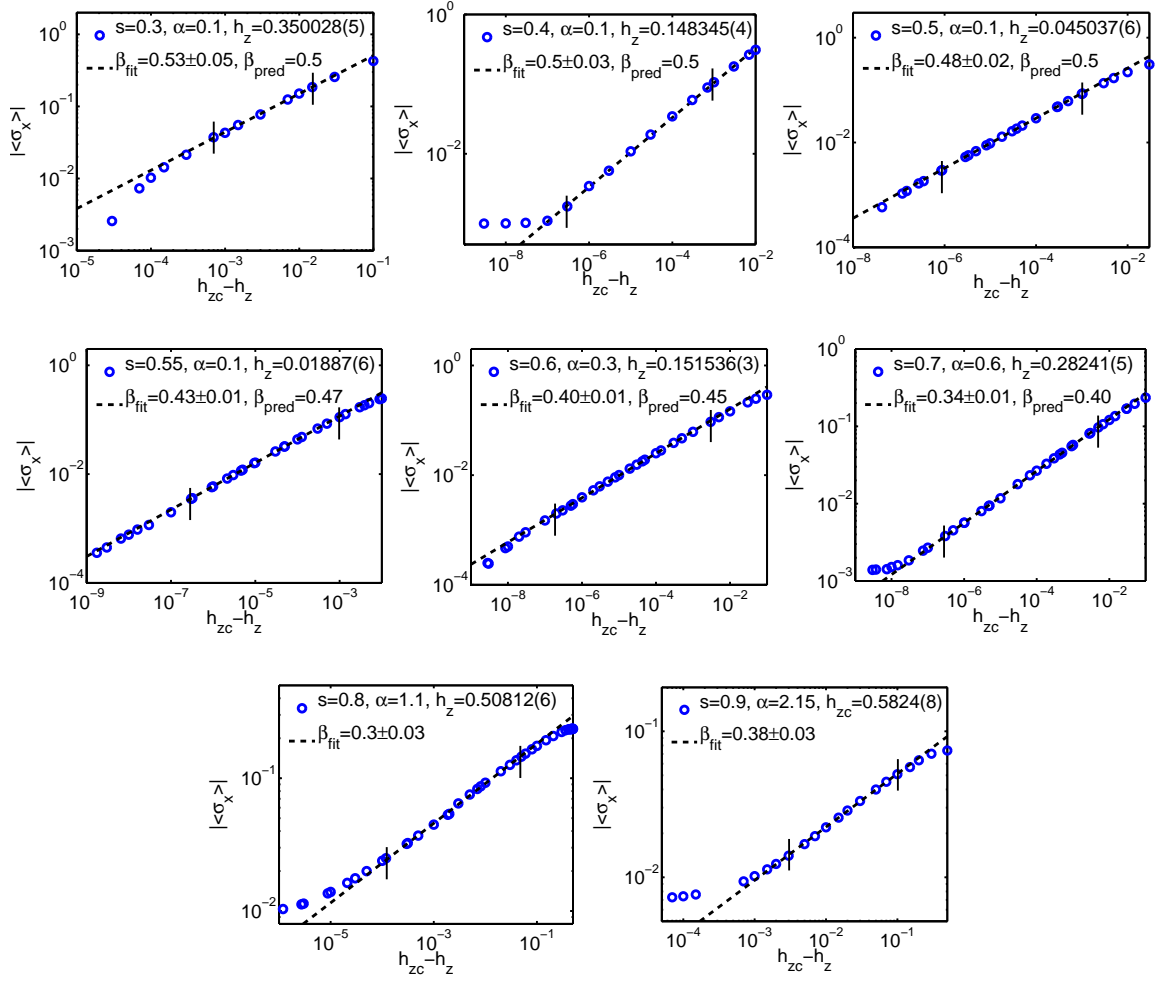
C.3.4 β at QC2

Figure C.7: Critical exponent β for different values of s at QC2, where the vertical black lines indicate the fitting range. In calculations for $s \leq 0.5$ we included the bosonic shift [V1: $N = 60$, $D = 60$, $d_{\text{opt}} = 24$, $\Lambda = 2$]. For $0.5 < s < 1$ we employed the symmetry code [V2: $D = 60$, $d_{\text{opt}} = 40$, $\Lambda = 2$, $N = 60$ ($0.5 < s < 0.8$), $N = 120$ ($s = 0.9$)].

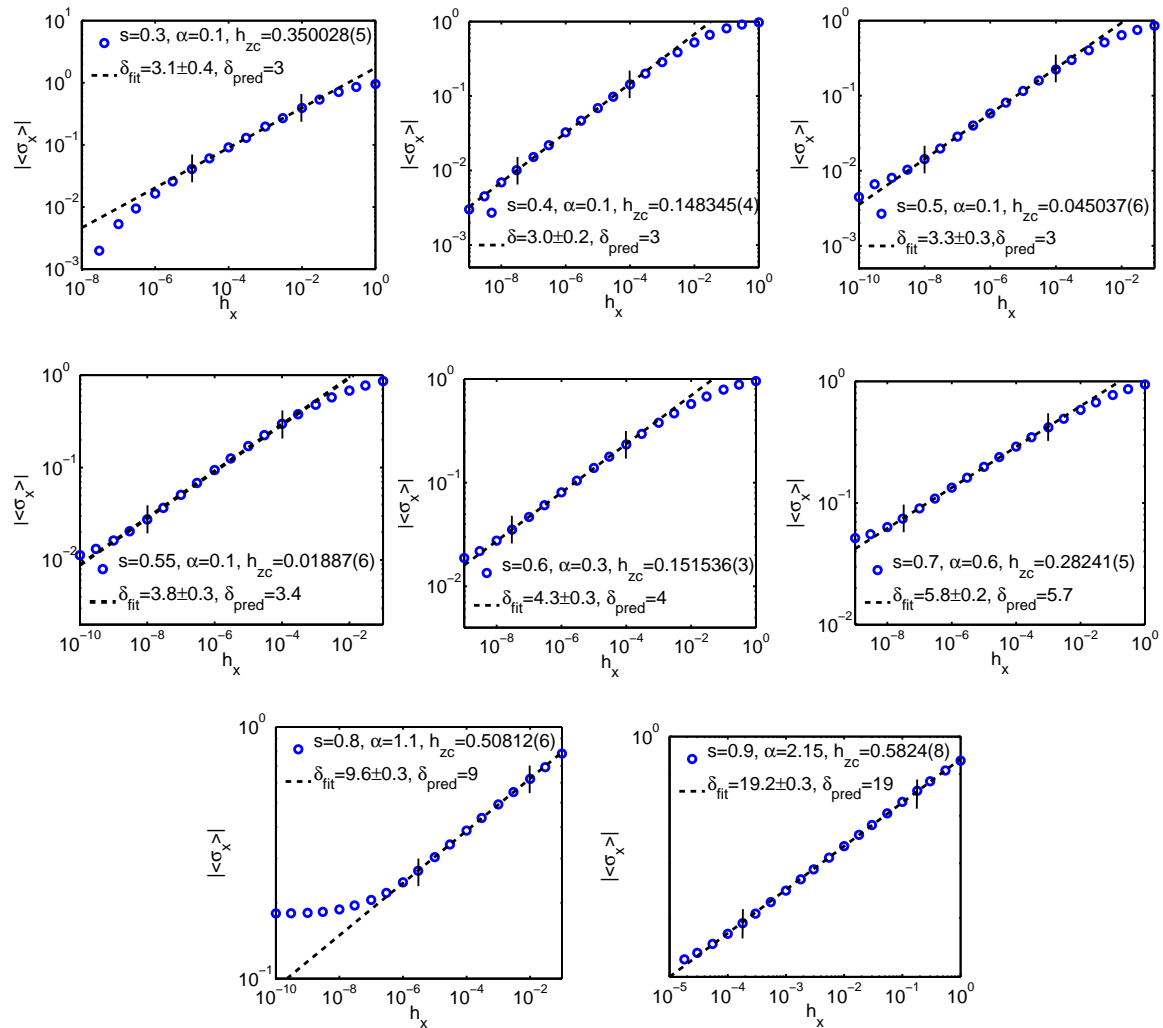
C.3.5 δ at QC2

Figure C.8: Critical exponent δ for different s at QC2, where vertical black lines indicate the fitting range [V1: $N = 60, D = 60, d_{opt} = 24, \Lambda = 2$].

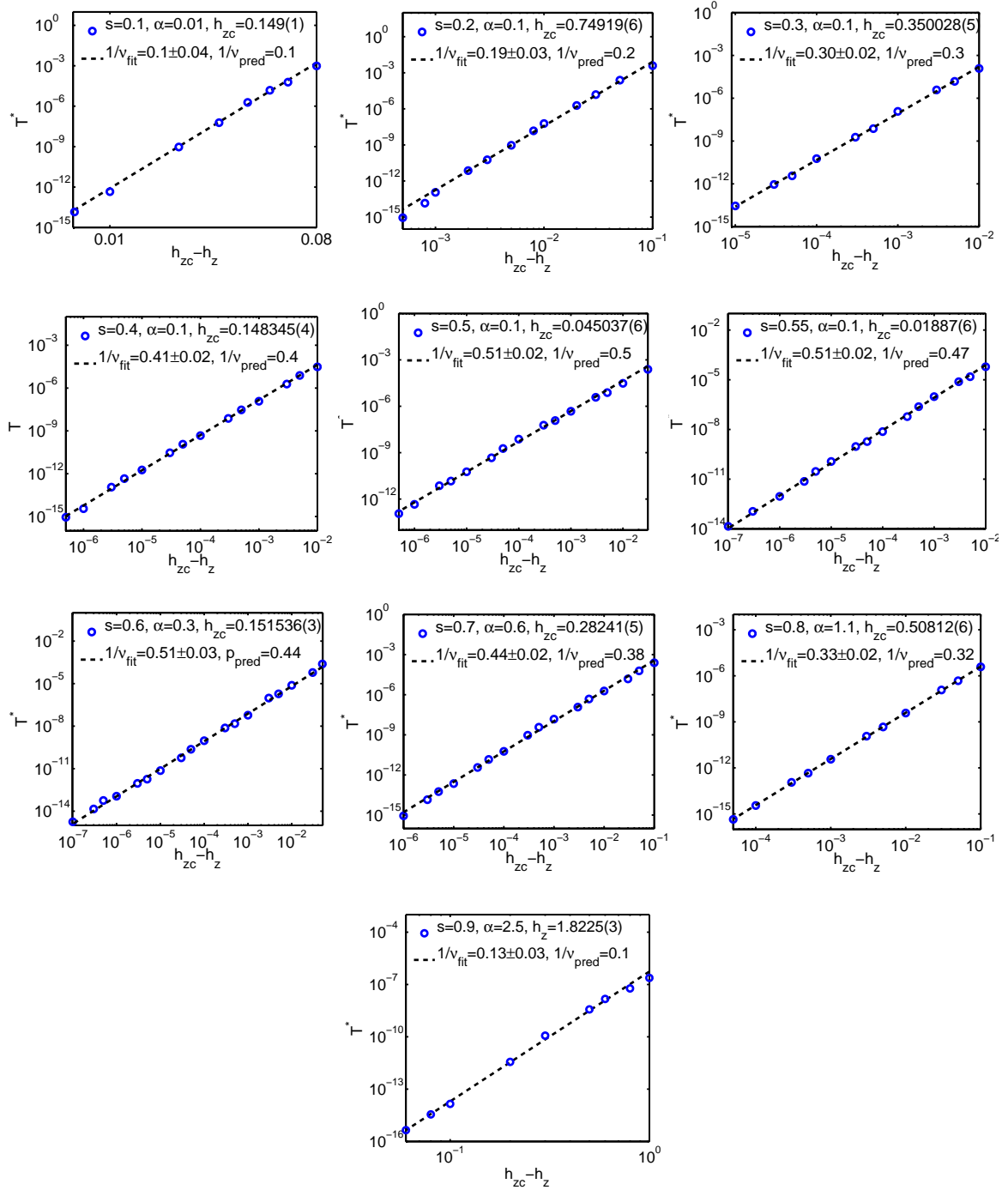
C.3.6 ν at QC2

Figure C.9: Critical exponent ν for different s at QC2 [V2: $N = 60$, $D = 60$, $d_{\text{opt}} = 40$, $\Lambda = 2$].

List of Figures

2.1	Phase transitions in a ferromagnetic material	4
2.2	Free energy of a ferromagnetic material (a) in a disordered, (b) in a critical and (c) in an ordered state.	6
2.3	Schematic phase diagram of system in the vicinity of a quantum phase transition.	10
3.1	(a) Schematic diagram of an MPS wavefunction in the (a) global and (b) local picture.	14
3.2	Graphical representation of MPS orthonormality conditions.	15
3.4	Schematic diagram of the overlap of two $ \psi'\rangle, \psi\rangle$ in MPS notation. The calculation is carried out by contracting the corresponding local indices n_i resulting in overall scalar quantity.	16
3.5	Graphical representation of the calculation of an expectation value in the MPS formalism.	17
3.6	(a) Spectral function $J(\omega)$ of a bosonic bath in the spin-boson model. (b) "star"-Hamiltonian of the discretized spin-boson model. (c) "chain"-Hamiltonian of the spin-boson model.	22
3.7	(a) Sketch of unscaled energy levels at different NRG iterations with ground state energy shifted to zero. (b) Typical energy-level flow diagram of $U(1)$ symmetric two-channel spin-boson model.	24
3.8	Graphical representation of application of the Hamiltonian \hat{H} to $ \psi\rangle$ during VMPS optimization	27
3.10	Typical VMPS energy-level flow diagram of $U(1)$ symmetric two-channel spin-boson model	31
3.11	MPS diagram illustrating the application of $\hat{U}(\tau)$ to $ \psi\rangle$	33
4.1	Schematic display of the spin-boson system with the quantum tunneling coefficient Δ and the bias ϵ	34
4.2	VMPS energy-flow diagrams for the sub-ohmic SBM with $s = 0.6$	36
4.3	The phase diagram of the SBM in (a) shows a transition between a localized ($\alpha > \alpha_c$) and a delocalized ($\alpha < \alpha_c$) regime for various values of the tunneling coefficient Δ . In (b) the Δ dependence of the critical coupling α_c is displayed for different values of s	37
4.4	Bosonic occupation numbers on Wilson chain sites	37
4.5	Critical exponents (a) β and (b) δ of the spin-boson model for different values of s calculated with VMPS (blue squares) and NRG (red dots).	39
4.6	Critical exponent ν of the spin-boson model for different values of s	40
4.7	Finite-size scaling of the magnetization m at the QPT of the spin-boson model for various values of s	41

4.8	Critical exponent x calculated from finite-size scaling (blue squares) and hyperscaling (red crosses) compared with the RG prediction $x = s$.	42
4.9	Time-evolution of the ohmic SBM (a) illustrating the virtue of z-averaging and (b) showing the characteristically different behavior in the weak and strong coupling regime.	44
4.10	Comparison tDMRG data with NIBA results for the non-equilibrium dynamics of the ohmic SBM	45
4.11	Non-equilibrium dynamics of a polarized impurity spin in the ohmic SBM (a) at the Toulouse point $\alpha = 1/2$ and (b) for short time scales in the weak damping regime $0 < \alpha < 1/2$.	46
4.12	Non-equilibrium dynamics of a fully polarized spin in the sub-ohmic SBM with $s = 0.7$ and $\Delta = 0.1$ for various values of α .	48
4.13	Non-equilibrium dynamics of a fully polarized spin for the sub-ohmic SBM with dissipation (a) $s = 0.5$ and (b) $s = 0$ for various values of α ($\Delta = 0.1$).	49
5.1	Schematic picture of the folded VMPS setup of the SBM2.	54
5.2	Schematic phase diagram of the two-bath spin-boson model	55
5.3	VMPS energy-flow diagrams for the sub-ohmic two-bath spin-boson model with $s = 0.8$	56
5.4	Schematic RG flow of the two-bath spin-boson model	57
5.5	Scaling of the magnetization inside the critical phase.	58
5.6	Non-linear response of the symmetry spin inside the critical phase to a transverse field h_z (a) and a in-plane bias field h_x (b).	59
5.7	Energy-level flow diagrams for fixed $s = 0.85$ and different values of α close to the critical fixed point.	59
5.8	Characteristic behavior of the bosonic occupation numbers on the Wilson chain near QC1 (a) and QC2 (b).	60
5.9	Phase boundary between localized and critical phase calculated with VMPS	61
5.10	Energy-level flow diagrams for $s = 0.85$ in the localized phase close to QC1.	62
5.11	VMPS results for critical exponents ν and β for various values of s at QC1	63
5.12	VMPS results for the critical exponents x and δ at QC1	64
5.13	Finite size scaling of the magnetization for various values of s at QC1	65
5.14	Dependence of the critical field h_{zc} on the coupling constant α and energy flow at the QC2.	66
5.15	VMPS results for the critical exponents β and δ at QC2	67
5.16	VMPS results for the critical exponents ν and x at QC2	68
5.17	Finite size scaling of the magnetization for various values of s at QC2	69
5.19	Non-linear response of the impurity spin to a magnetic field in (a) x - and (b) z -direction for different coupling asymmetries $\Delta\alpha$ and fixed s in the critical phase [V1: $N = 50$, $D = 60$, $d_{opt} = 24$, $\Lambda = 2$].	71
5.20	VMPS energy-level flow diagrams in the critical regime calculated with (a) V1 and (b) V2.	72
5.21	VMPS flow diagrams for fixed model parameter $s = 0.85$ and different values of α inside the critical phase.	73
5.22	Finite size scaling of the magnetization in the critical phase calculated with V1 (red solid line) and V2 (blue dashed line).	73
5.23	VMPS energy-level flow diagrams for fixed $s = 0.65$ and $\alpha = 0.1$ in the localized regime calculated with (a) V1 and (b) V2.	74

5.24	(a) Finite size scaling of the magnetization in the critical phase calculated with V1 (red solid line) and V2 (blue dashed line) and the corresponding bosonic occupation numbers on the Wilson chain.	75
5.25	Vanishing magnetization at the transition between localized and delocalized phase calculated with (a) V1 and (b) V2 for fixed $s = 0.9$, $\alpha = 3$ and identical VMPS parameters	75
A.1	Steps 1 and 2 of the two-site update procedure when sweeping from left to right. The indices connecting the matrices surrounded by the dashed lines are contracted. The red filled square is the subject of the VMPS optimization.	80
A.2	Steps 3 and 4 of the two-site update procedure when sweeping from left to right. The indices connecting the matrices surrounded by the dashed lines are contracted. The red filled square is the subject of the VMPS optimization.	81
B.1	Critical exponent ν extracted from $T^* \sim (\alpha - \alpha_c)^{1/\nu}$ for different s at the QPC of the SBM. In all calculations we used the parity code [$N = 100$, $D = 40$, $d_{opt} = 16$, $\Lambda = 2$].	82
C.1	Finite-size scaling of the magnetization in the localized and in the critical regime.	84
C.2	Influence of diverging bosonic basis on the magnetization inside the localized phase	85
C.3	Calculation of the critical exponent β at QC1.	86
C.4	Critical exponent ν for different values s at QC1	87
C.5	Critical exponent β for different values s at QC1	88
C.6	Critical exponent δ for different values of s at QC1.	89
C.7	Critical exponent β for different values of s at QC2.	90
C.8	Critical exponent δ for different s at QC2.	91
C.9	Critical exponent ν for different values of s at QC2.	92

Bibliography

- [1] P. W. Anderson, G. Yuval, and D. R. Hamann, “Exact results in the Kondo problem. II. Scaling theory, qualitatively correct solution, and some new results on one-dimensional classical statistical models,” *Phys. Rev. B* **1**, 4464–4473 (1970).
- [2] A. Hewson, *The Kondo Problem to Heavy Fermions*, *Cambridge Studies in Magnetism* (Cambridge University Press, 1997).
- [3] F. Guinea, V. Hakim, and A. Muramatsu, “Bosonization of a two-level system with dissipation,” *Phys. Rev. B* **32**, 4410–4418 (1985).
- [4] A. J. Leggett, S. Chakravarty, A. T. Dorsey, M. P. A. Fisher, A. Garg, and W. Zwerger, “Dynamics of the dissipative two-state system,” *Rev. Mod. Phys.* **59**, 1–85 (1987).
- [5] U. Weiss, *Quantum Dissipative Systems (Second Edition)*, *Series in modern condensed matter physics* (World Scientific Publishing Company, Incorporated, 1999).
- [6] A. O. Caldeira and A. J. Leggett, “Influence of dissipation on quantum tunneling in macroscopic systems,” *Phys. Rev. Lett.* **46**, 211–214 (1981).
- [7] R. Marcus and N. Sutin, “Electron transfers in chemistry and biology,” *Biochimica et Biophysica Acta (BBA) - Reviews on Bioenergetics* **811**(3), 265 – 322 (1985).
- [8] Y. Makhlin, G. Schön, and A. Shnirman, “Quantum-state engineering with josephson-junction devices,” *Rev. Mod. Phys.* **73**, 357–400 (2001).
- [9] J. E. Mooij, T. P. Orlando, L. Levitov, L. Tian, C. H. van der Wal, and S. Lloyd, “Josephson persistent-current qubit,” *Science* **285**(5430), 1036–1039 (1999).
- [10] A. Recati, P. O. Fedichev, W. Zwerger, J. von Delft, and P. Zoller, “Atomic quantum dots coupled to a reservoir of a superfluid bose-einstein condensate,” *Phys. Rev. Lett.* **94**, 040404 (2005).
- [11] P. P. Orth, I. Stanic, and K. Le Hur, “Dissipative quantum ising model in a cold-atom spin-boson mixture,” *Phys. Rev. A* **77**, 051601 (2008).
- [12] K. G. Wilson, “Renormalization group and critical phenomena. I. Renormalization group and the Kadanoff scaling picture,” *Phys. Rev. B* **4**, 3174–3183 (1971).
- [13] R. Bulla, T. A. Costi, and T. Pruschke, “Numerical renormalization group method for quantum impurity systems,” *Rev. Mod. Phys.* **80**, 395–450 (2008).
- [14] S. R. White, “Density matrix formulation for quantum renormalization groups,” *Phys. Rev. Lett.* **69**, 2863–2866 (1992).

- [15] U. Schollwöck, “The density-matrix renormalization group,” *Rev. Mod. Phys.* **77**, 259–315 (2005).
- [16] R. Bulla, N.-H. Tong, and M. Vojta, “Numerical renormalization group for bosonic systems and application to the sub-ohmic spin-boson model,” *Phys. Rev. Lett.* **91**, 170601 (2003).
- [17] M. Vojta, N.-H. Tong, and R. Bulla, “Quantum phase transitions in the sub-ohmic spin-boson model: Failure of the quantum-classical mapping,” *Phys. Rev. Lett.* **94**, 070604 (2005).
- [18] M. T. Glossop and K. Ingersent, “Numerical renormalization-group study of the Bose-Fermi Kondo model,” *Phys. Rev. Lett.* **95**, 067202 (2005).
- [19] A. Winter, H. Rieger, M. Vojta, and R. Bulla, “Quantum phase transition in the sub-ohmic spin-boson model: Quantum monte-carlo study with a continuous imaginary time cluster algorithm,” *Phys. Rev. Lett.* **102**, 030601 (2009).
- [20] A. Alvermann and H. Fehske, “Sparse polynomial space approach to dissipative quantum systems: Application to the sub-ohmic spin-boson model,” *Phys. Rev. Lett.* **102**, 150601 (2009).
- [21] C. Guo, A. Weichselbaum, J. von Delft, and M. Vojta, “Critical and strong-coupling phases in one- and two-bath spin-boson models,” *Phys. Rev. Lett.* **108**, 160401 (2012).
- [22] U. Schollwöck, “The density-matrix renormalization group in the age of matrix product states,” *Annals of Physics* **326**(1), 96 – 192 (2011).
- [23] H. Nishimori and G. Ortiz, *Elements of Phase Transitions and Critical Phenomena*, *Oxford Graduate Texts* (OUP Oxford, 2011).
- [24] D. Uzunov, *Introduction to the Theory of Critical Phenomena: Mean Field, Fluctuations and Renormalization* (World Scientific, 2010).
- [25] M. Vojta, “Quantum phase transitions,” *Reports on Progress in Physics* **66**(12), 2069 (2003).
- [26] T. Vojta, “Computing quantum phase transitions,” in *Reviews in Computational Chemistry* (John Wiley and Sons, Inc., 2009), pp. 167–221.
- [27] S. Sachdev, *Quantum Phase Transitions* (University Press, 2001).
- [28] P. Ehrenfest, “Continuous quantum phase transitions,” *Proc. Kon. Akad. Akad. Wetenschap, Amsterdam* **36**, 153 (1933).
- [29] P. Weiss, “L’hypothse du champ molculaire et la proprit ferromagntiqu,” *J. Phys. (Paris)* **6**(1), 661–690 (1907).
- [30] J. D. van der Waals, “On the continuity of the gas and liquid state,” PhD thesis, University of Leiden (1873).
- [31] L. Landau, *Collected papers of L. D. Landau* (Gordon and Breach, 1965).
- [32] K. G. Wilson and J. Kogut, “The renormalization group and the epsilon expansion,” *Physics Reports* **12**(2), 75 – 199 (1974).

- [33] N. Goldenfeld, *Lectures on Phase Transitions and the Renormalization Group*, *Frontiers in Physics*, 85 (Perseus Books, 1992).
- [34] J. Orenstein and A. J. Millis, “Advances in the physics of high-temperature superconductivity,” *Science* **288**(5465), 468–474 (2000).
- [35] S. Sachdev, “Quantum criticality: Competing ground states in low dimensions,” *Science* **288**(5465), 475–480 (2000).
- [36] H. von Loehneysen, “Non-fermi-liquid behaviour in the heavy-fermion system,” *Journal of Physics: Condensed Matter* **8**(48), 9689 (1996).
- [37] P. Coleman, “Theories of non-fermi liquid behavior in heavy fermions,” *Physica B: Condensed Matter* **259261**(0), 353 – 358 (1999).
- [38] S. V. Kravchenko, W. E. Mason, G. E. Bowker, J. E. Furneaux, V. M. Pudalov, and M. D’orio, “Scaling of an anomalous metal-insulator transition in a two-dimensional system in silicon at $b=0$,” *Phys. Rev. B* **51**, 7038–7045 (1995).
- [39] S. L. Sondhi, S. M. Girvin, J. P. Carini, and D. Shahar, “Continuous quantum phase transitions,” *Rev. Mod. Phys.* **69**, 315–333 (1997).
- [40] V. J. Emery and A. Luther, “Low-temperature properties of the Kondo Hamiltonian,” *Phys. Rev. B* **9**, 215–226 (1974).
- [41] M. Vojta, “Impurity quantum phase transitions,” *Philosophical Magazine* **86**(13-14), 1807–1846 (2006).
- [42] J. M. Kosterlitz and D. J. Thouless, “Ordering, metastability and phase transitions in two-dimensional systems,” *Journal of Physics C: Solid State Physics* **6**(7), 1181 (1973).
- [43] A. Weichselbaum, F. Verstraete, U. Schollwöck, J. I. Cirac, and J. von Delft, “Variational matrix-product-state approach to quantum impurity models,” *Phys. Rev. B* **80**, 165117 (2009).
- [44] S. Rommer and S. Östlund, “Class of ansatz wave functions for one-dimensional spin systems and their relation to the density matrix renormalization group,” *Phys. Rev. B* **55**, 2164–2181 (1997).
- [45] J. Dukelsky, M. A. Martin-Delgado, T. Nishino, and G. Sierra, “Equivalence of the variational matrix product method and the density matrix renormalization group applied to spin chains,” *Europhysics Letters* **43**(4), 457 (1998).
- [46] A. Weichselbaum, “Tensor networks and the numerical renormalization group,” *Phys. Rev. B* **86**, 245124 (2012).
- [47] H. Saberi, A. Weichselbaum, and J. von Delft, “Matrix-product-state comparison of the numerical renormalization group and the variational formulation of the density-matrix renormalization group,” *Phys. Rev. B* **78**, 035124 (2008).
- [48] W. Muender, A. Weichselbaum, A. Holzner, J. von Delft, and C. L. Henley, “Correlation density matrices for one-dimensional quantum chains based on the density matrix renormalization group,” *New Journal of Physics* **12**(7), 075027 (2010).
- [49] R. Bulla, H.-J. Lee, N.-H. Tong, and M. Vojta, “Numerical renormalization group for quantum impurities in a bosonic bath,” *Phys. Rev. B* **71**(4), 045122 (2005).

- [50] M. B. Plenio, J. Eisert, J. Dreißig, and M. Cramer, “Entropy, entanglement, and area: Analytical results for harmonic lattice systems,” *Phys. Rev. Lett.* **94**, 060503 (2005).
- [51] T. Barthel, M.-C. Chung, and U. Schollwöck, “Entanglement scaling in critical two-dimensional fermionic and bosonic systems,” *Phys. Rev. A* **74**, 022329 (2006).
- [52] N. Schuch, M. M. Wolf, F. Verstraete, and J. I. Cirac, “Entropy scaling and simulability by matrix product states,” *Phys. Rev. Lett.* **100**, 030504 (2008).
- [53] A. Weichselbaum, “Tensor networks and the numerical renormalization group,” Habilitation thesis, LMU Munich, (2012).
- [54] A. Weichselbaum, “Non-abelian symmetries in tensor networks: A quantum symmetry space approach,” *Annals of Physics* **327**(12), 2972 – 3047 (2012).
- [55] B. A. Jones and C. M. Varma, “Study of two magnetic impurities in a Fermi gas,” *Phys. Rev. Lett.* **58**, 843–846 (1987).
- [56] H. R. Krishna-murthy, J. W. Wilkins, and K. G. Wilson, “Renormalization-group approach to the Anderson model of dilute magnetic alloys. I. Static properties for the symmetric case,” *Phys. Rev. B* **21**, 1003–1043 (1980).
- [57] L. N. Oliveira and J. W. Wilkins, “New approach to the x-ray-absorption problem,” *Phys. Rev. B* **24**, 4863–4866 (1981).
- [58] F. B. Anders and A. Schiller, “Real-time dynamics in quantum-impurity systems: A time-dependent numerical renormalization-group approach,” *Phys. Rev. Lett.* **95**, 196801 (2005).
- [59] F. B. Anders and A. Schiller, “Spin precession and real-time dynamics in the Kondo model: Time-dependent numerical renormalization-group study,” *Phys. Rev. B* **74**, 245113 (2006).
- [60] A. Weichselbaum and J. von Delft, “Sum-rule conserving spectral functions from the numerical renormalization group,” *Phys. Rev. Lett.* **99**, 076402 (2007).
- [61] C. Latta, F. Haupt, M. Hanl, A. Weichselbaum, M. Claassen, W. Wuester, P. Fallahi, S. Faelt, L. Glazman, J. von Delft, H. Türeci, and A. Imamoglu, “Quantum quench of Kondo correlations in optical absorption,” *Nature* **474**(7353), 627–630 (2011).
- [62] M. Vojta, N.-H. Tong, and R. Bulla, “Erratum: Quantum phase transitions in the sub-ohmic spin-boson model: Failure of the quantum-classical mapping [*phys. rev. lett.* 94, 070604 (2005)],” *Phys. Rev. Lett.* **102**, 249904 (2009).
- [63] A. Weichselbaum, F. Verstraete, U. Schollwöck, J. Cirac, and J. von Delft, “Variational matrix product state approach to quantum impurity models,” arXiv preprint cond-mat/0504305, (2005).
- [64] A. Weichselbaum, “Discarded weight and entanglement spectra in the numerical renormalization group,” *Phys. Rev. B* **84**, 125130 (2011).
- [65] S. Kirchner, K. Ingersent, and Q. Si, “Quantum criticality of the sub-ohmic spin-boson model,” *Phys. Rev. B* **85**, 075113 (2012).
- [66] S. R. White, “Density-matrix algorithms for quantum renormalization groups,” *Phys. Rev. B* **48**, 10345–10356 (1993).

- [67] K. A. Hallberg, “Density-matrix algorithm for the calculation of dynamical properties of low-dimensional systems,” *Phys. Rev. B* **52**, R9827–R9830 (1995).
- [68] T. D. Kuehner and S. R. White, “Dynamical correlation functions using the density matrix renormalization group,” *Phys. Rev. B* **60**, 335–343 (1999).
- [69] R. J. Bursill, T. Xiang, and G. A. Gehring, “The density matrix renormalization group for a quantum spin chain at non-zero temperature,” *Journal of Physics: Condensed Matter* **8**(40), L583 (1996).
- [70] X. Wang and T. Xiang, “Transfer-matrix density-matrix renormalization-group theory for thermodynamics of one-dimensional quantum systems,” *Phys. Rev. B* **56**, 5061–5064 (1997).
- [71] S. R. White, “Spin gaps in a frustrated Heisenberg model for CaV_4O_9 ,” *Phys. Rev. Lett.* **77**, 3633–3636 (1996).
- [72] S. R. White and D. J. Scalapino, “Energetics of domain walls in the 2d $t - J$ model,” *Phys. Rev. Lett.* **81**, 3227–3230 (1998).
- [73] F. Verstraete and J. I. Cirac, “Renormalization algorithms for quantum-many body systems in two and higher dimensions,” eprint arXiv:cond-mat/0407066, (2004).
- [74] V. Murg, F. Verstraete, O. Legeza, and R. M. Noack, “Simulating strongly correlated quantum systems with tree tensor networks,” *Phys. Rev. B* **82**, 205105 (2010).
- [75] S. Depenbrock, I. P. McCulloch, and U. Schollwöck, “Nature of the spin-liquid ground state of the $s = 1/2$ Heisenberg model on the Kagome lattice,” *Phys. Rev. Lett.* **109**, 067201 (2012).
- [76] H. Takasaki, T. Hikihara, and T. Nishino, “Fixed point of the finite system DMRG,” *Journal of the Physical Society of Japan* **68**(5), 1537–1540 (1999).
- [77] G. Vidal, “Efficient simulation of one-dimensional quantum many-body systems,” *Phys. Rev. Lett.* **93**, 040502 (2004).
- [78] C. Lanczos, “An iteration method for the solution of the eigenvalue problem of linear differential and integral operators,” *Journal of research of the National Bureau of Standards* **45**, 255–282 (1950).
- [79] E. R. Davidson, “The iterative calculation of a few of the lowest eigenvalues and corresponding eigenvectors of large real-symmetric matrices,” *Journal of Computational Physics* **17**(1), 87 – 94 (1975).
- [80] C. Guo, A. Weichselbaum, J. von Delft, and M. Vojta, “Critical and strong-coupling phases in one- and two-bath spin-boson models, supplementary,” *Phys. Rev. Lett.* **108**, 160401 (2012).
- [81] C. Zhang, E. Jeckelmann, and S. R. White, “Density matrix approach to local hilbert space reduction,” *Phys. Rev. Lett.* **80**, 2661–2664 (1998).
- [82] A. J. Daley, C. Kollath, U. Schollwöck, and G. Vidal, “Time-dependent density-matrix renormalization-group using adaptive effective hilbert spaces,” *Journal of Statistical Mechanics: Theory and Experiment* **2004**(04), P04005 (2004).

- [83] F. Verstraete, J. J. Garcia-Ripoll, and J. I. Cirac, “Matrix product density operators: Simulation of finite-temperature and dissipative systems,” *Phys. Rev. Lett.* **93**, 207204 (2004).
- [84] S. R. White and A. E. Feiguin, “Real-time evolution using the density matrix renormalization group,” *Phys. Rev. Lett.* **93**, 076401 (2004).
- [85] T. Prosen and M. Znidaric, “Matrix product simulations of non-equilibrium steady states of quantum spin chains,” *Journal of Statistical Mechanics: Theory and Experiment* **2009**(02), P02035 (2009).
- [86] D. Porras, F. Marquardt, J. von Delft, and J. I. Cirac, “Mesoscopic spin-boson models of trapped ions,” *Phys. Rev. A* **78**, 010101 (2008).
- [87] M. Vojta, N.-H. Tong, and R. Bulla, “Erratum: Quantum phase transitions in the sub-ohmic spin-boson model: Failure of the quantum-classical mapping [*Phys. Rev. Lett.* 94, 070604 (2005)],” *Phys. Rev. Lett.* **102**, 249904 (2009).
- [88] M. Vojta, R. Bulla, F. Güttge, and F. Anders, “Mass-flow error in the numerical renormalization-group method and the critical behavior of the sub-ohmic spin-boson model,” *Phys. Rev. B* **81**, 075122 (2010).
- [89] M. Vojta, “Numerical renormalization group for the sub-ohmic spin-boson model: A conspiracy of errors,” *Phys. Rev. B* **85**, 115113 (2012).
- [90] M. E. Fisher, S.-k. Ma, and B. G. Nickel, “Critical exponents for long-range interactions,” *Phys. Rev. Lett.* **29**, 917–920 (1972).
- [91] E. Luijten and H. W. J. Blöte, “Classical critical behavior of spin models with long-range interactions,” *Phys. Rev. B* **56**, 8945–8958 (1997).
- [92] Q. Si, S. Rabello, K. Ingersent, and J. L. Smith, “Locally critical quantum phase transitions in strongly correlated metals,” *Nature* **413**(6858), 804–808 (2001).
- [93] Q. Si, S. Rabello, K. Ingersent, and J. L. Smith, “Local fluctuations in quantum critical metals,” *Phys. Rev. B* **68**, 115103 (2003).
- [94] S. Kirchner, K. Ingersent, and Q. Si, “Quantum criticality of the sub-ohmic spin-boson model,” *Phys. Rev. B* **85**, 075113 (2012).
- [95] M. Vojta, C. Buragohain, and S. Sachdev, “Quantum impurity dynamics in two-dimensional antiferromagnets and superconductors,” *Phys. Rev. B* **61**, 15152–15184 (2000).
- [96] M. Vojta, Private communication, (2013).
- [97] H. Dekker, “Noninteracting-blip approximation for a two-level system coupled to a heat bath,” *Phys. Rev. A* **35**, 1436–1437 (1987).
- [98] F. B. Anders, R. Bulla, and M. Vojta, “Equilibrium and nonequilibrium dynamics of the sub-ohmic spin-boson model,” *Phys. Rev. Lett.* **98**, 210402 (2007).
- [99] M. Yoshida, M. A. Whitaker, and L. N. Oliveira, “Renormalization-group calculation of excitation properties for impurity models,” *Phys. Rev. B* **41**, 9403–9414 (1990).

-
- [100] Q. Wang, A.-Y. Hu, and H. Zheng, “Analytical approach to dynamical behavior and phase diagrams in dissipative two-state systems,” *Phys. Rev. B* **80**, 214301 (2009).
- [101] D. Kast and J. Ankerhold, “Persistence of coherent quantum dynamics at strong dissipation,” *Phys. Rev. Lett.* **110**, 010402 (2013).
- [102] D. Kast and J. Ankerhold, “Dynamics of quantum coherences at strong coupling to a heat bath,” *Phys. Rev. B* **87**, 134301 (2013).
- [103] A. H. Castro Neto, E. Novais, L. Borda, G. Zaránd, and I. Affleck, “Quantum magnetic impurities in magnetically ordered systems,” *Phys. Rev. Lett.* **91**, 096401 (2003).
- [104] E. Novais, A. H. Castro Neto, L. Borda, I. Affleck, and G. Zarand, “Frustration of decoherence in open quantum systems,” *Phys. Rev. B* **72**, 014417 (2005).
- [105] G. Zaránd and E. Demler, “Quantum phase transitions in the Bose-Fermi Kondo model,” *Phys. Rev. B* **66**, 024427 (2002).
- [106] L. Zhu and Q. Si, “Critical local-moment fluctuations in the Bose-Fermi Kondo model,” *Phys. Rev. B* **66**, 024426 (2002).
- [107] D. V. Khveshchenko, “Quantum impurity models of noisy qubits,” *Phys. Rev. B* **69**, 153311 (2004).
- [108] A. Weichselbaum, Private communication, (2013).
- [109] C. Guo, “Using density matrix renormalization group to study open quantum systems,” PhD thesis, LMU Munich (2012).
- [110] P. P. Orth, D. Roosen, W. Hofstetter, and K. Le Hur, “Dynamics, synchronization, and quantum phase transitions of two dissipative spins,” *Phys. Rev. B* **82**, 144423 (2010).
- [111] T. Werner, “Phasenübergang des Zwei-Spin Boson Modells,” Bachelor thesis, LMU Munich, (2013).
- [112] S. Holzner, “DMRG studies of Chebychev-expanded spectral functions and quantum impurity models,” PhD thesis, LMU Munich (2011).
- [113] I. P. McCulloch, “From density-matrix renormalization group to matrix product states,” *Journal of Statistical Mechanics: Theory and Experiment* **2007**(10), P10014 (2007).

Danksagung

Zuallererst möchte ich mich sehr herzlich bei Prof. Jan von Delft bedanken – nicht nur für die Möglichkeit meine Masterarbeit in seiner Gruppe schreiben zu dürfen sowie seine Ideen und sein Fachwissen, die in diese Arbeit eingeflossen sind, sondern auch für seine hervorragenden Vorlesungen, die früh mein Interesse für theoretische Festkörperphysik geweckt haben.

Darüber hinaus möchte ich mich ganz herzlich bei PD Dr. Andreas Weichselbaum bedanken, der sich viel Zeit für meine Fragen nahm und von dem ich in zahlreichen Diskussionen viel über NRG und DMRG lernen konnte. Zudem waren mir seine numerische Expertise und nicht zuletzt sein hocheffizienter MPS Code eine große Hilfe bei der Durchführung meiner Arbeit.

Vielen Dank an Prof. Matthias Vojta, der sein großes Fachwissen im Rahmen unserer Kollaboration einbrachte und mit vielen spannenden Ideen und Vorschlägen das Projekt weiter vorantrieb.

Ein großes Dankeschön geht an Dr. Cheng Guo, der mich zu Beginn meiner Arbeit in die VMPS Thematik einführte und mir seinen VMPS Code überlassen hat. Außerdem vielen Dank an Markus Hanl für die zahlreichen Diskussionen über NRG und den vielen Kaffee. Gleiches gilt natürlich auch für all die anderen netten Menschen am Lehrstuhl.

Selbstständigkeitserklärung

Hiermit erkläre ich, die vorliegende Arbeit selbständig verfasst zu haben und keine anderen als die in der Arbeit angegebenen Quellen und Hilfsmittel benutzt zu haben.

München, den 5. Juni 2013